GEOLOGICAL SURVEY OF CANADA
OPEN FILE 7451

Feasibility study of Using Muon Observations for Extreme Space Weather Early Warning (final report)

L. Trichtchenko, G. Kalugin, J. Armitage, K. Boudjemline and D. Waller

2013

Natural Resources Canada | Ressources naturelles Canada

Canada

GEOLOGICAL SURVEY OF CANADA
OPEN FILE 7451

Feasibility study of Using Muon Observations for Extreme Space Weather Early Warning (final report)

L. Trichtchenko[1], G. Kalugin[1], J. Armitage[2], K. Boudjemline[2] and D. Waller[3]

[1]- Geological Survey of Canada, 2617 Anderson Rd., Ottawa, ON, K1A 0E7
[2]- Carleton University, 1125 Colonel By Drive, Ottawa, ON, K1S 5B6
[3]- Defence R&D Canada-Ottawa, 3701 Carling Avenue, Ottawa, ON, K1A 0Z4

2013

doi:10.4095/292841

This publication is available for free download through GEOSCAN (http://geoscan.ess.nrcan.gc.ca/).

Recommended citation
Trichtchenko, L., Kalugin,G., Armitage, J., Boudjemline, K., and Waller, D., 2013. Feasibility study of Using Muon Observations for Extreme Space Weather Early Warning (final report); Geological Survey of Canada, Open File 7451, 109 p. doi:10.4095/292841

Publications in this series have not been edited; they are released as submitted by the author.

Abstract

This project is motivated by the need for improved protection of Canadian critical infrastructure from solar disturbances. The feasibility study examines the possibility of using measurements of muons produced by cosmic rays (CR) to provide advanced warning of approaching solar disturbances. A literature review and workshops with invited specialists were the important part of work. These identified the need for a Canadian muon detector to fill the coverage gap existing in global network.

Two types of tasks were undertaken: theoretical investigations of the interaction of cosmic rays with solar disturbances performed by the Lead Department, NRCan; and review of the existing technology and development of a test detector, done by a Contractor, Physics Department at Carleton University.

The study identified two types of precursors associated with interaction of the CR with solar disturbance. The physics-based transport equation for CR has been analysed and diffusion model was validated. Two types of technology for building detectors were assessed, a test muon detector has been built and prototype data were analysed.

The detailed design specifications and recommendations (roadmap) for proto-operational developments are provided.

Résumé

Ce projet a été lancé pour aider les spécialistes à mieux protéger l'infrastructure canadienne essentielle des perturbations solaires. L'étude de faisabilité examine la possibilité de se baser sur la mesure des muons produits par le rayonnement cosmique pour donner aux personnes intéressées un préavis de l'approche de perturbations solaires. Les travaux ont consisté principalement en une analyse documentaire et en la tenue d'ateliers auxquels des spécialistes ont été invités. Ces travaux ont permis de relever la nécessité de doter le Canada d'un détecteur de muons afin de combler la lacune relevée dans la couverture du réseau international.

Deux types de tâches ont été entreprises : des recherches théoriques sur l'interaction entre le rayonnement cosmique et les perturbations solaires, effectuées par Ressources naturelles Canada à titre de ministère responsable, et une étude de la technologie existante ainsi que la conception d'un détecteur d'essai, tâches confiées à au département de physique de l'Université Carleton à titre d'entrepreneur.

Les recherches ont permis d'identifier deux types de précurseurs associés aux interactions entre le rayonnement cosmique et les perturbations solaires. L'équation du transport fondée sur la physique pour le rayonnement cosmique a été analysée, et le modèle de diffusion a été validé. Deux types de technologies ont été évaluées en vue de la construction de détecteurs. Un détecteur de muons d'essai a été conçu et les données produites par le prototype ont été analysées.

Les spécifications de conception et des recommandations détaillées (feuille de route) ont été fournies en vue de la conception proto-opérationnelle.

Executive summary

Modern society is becoming more and more dependent on technological systems, such as power grids, which could be harmfully impacted by extreme space weather events resulting from solar disturbances. Sufficient early warning of an approaching disturbance would allow power grid operators to take protective measures. Unfortunately, the existing observations of the Sun can provide up to three days warning but with extremely poor reliability; errors can be as large as 12 hours and the rate of false alarms is high.

The primary objective of this study is to determine the feasibility of obtaining timely warning of extreme space weather conditions by using ground-based measurements of cosmic-ray-induced muons. It is based on the recent scientific evidence that precursors could be seen in changes of the flux of muons produced in Earth's atmosphere by galactic cosmic rays (CRs)

A literature review and workshops with invited specialists helped in identification of two types of tasks. One is to increase knowledge by theoretical investigations of the interaction of cosmic rays with solar disturbances. It has been performed by the Lead Department, i.e. visiting fellow and the staff of the Space Weather Forecast Centre, Natural Resources Canada. Another is the experimental part, i.e. to assess the need for Canadian muon detector, review the existing technology and develop the test detector. It has been done by a Contractor, i.e. the group of students, postdoctoral fellow and professors at Physics Department, Carleton University.

It has been found, that two types of precursors are described in the literature, both associated with variations of the flux of cosmic rays due to interactions with propagating solar disturbance. The physics-based transport equation was analysed based on data from existing muon telescope in Nagoya and solar disturbance measurements. The validity of the diffusion model for CR interaction with solar disturbance has been verified.

It has been identified that today the existing global muon detector network has a coverage gap over the North America region. Thus, it is important to have a muon detector in Canada. The existing technology has been assessed and a test muon detector has been built. The data from this detector have been analysed. This confirmed that technology readiness level is high and the detailed design specifications and recommendations for future work were provided.

Future plans: Analysis of the state-of-the-art of using muon detectors for extreme space weather forecasting and progress made in this research area showed that both knowledge level and technology readiness levels are high enough that it is feasible to use full-sky muon detector network for development of the prototype space weather forecasting.

Significance: Development of proto-operational muon detector in Canada will fill the gap in global coverage and therefore make an important contribution towards proto-operational use of the muon measurements. This would improve the advanced forecast of extreme space weather.

Sommaire

La société moderne dépend de plus en plus d'une infrastructure technique susceptible de subir les effets néfastes de conditions spatiométéorologiques extrêmes causées par des perturbations solaires. S'ils étaient avertis suffisamment tôt d'une perturbation à venir, les exploitants de réseaux électriques pourraient prendre des mesures de protection. Malheureusement, les méthodes actuelles d'observation du soleil ne donnent que trois jours de préavis et leur fiabilité est extrêmement faible : un décalage de 12 heures peut se produire entre la prévision et la réalité, et le taux de fausses alertes est élevé.

L'objectif principal de cette étude est d'établir s'il est possible d'obtenir des alertes rapides des conditions spatiométéorologiques extrêmes en se basant sur la mesure au sol des muons produits par le rayonnement cosmique. En effet, on a récemment obtenu la preuve scientifique qu'un changement du flux des muons produits dans l'atmosphère terrestre par le rayonnement cosmique galactique peut indiquer une perturbation à venir.

Les travaux ont consisté principalement en une analyse documentaire et en la tenue d'ateliers auxquels des spécialistes ont été invités, ce qui a permis de relever deux types de tâches à faire. Le premier type consistait à approfondir les connaissances en procédant à des recherches théoriques sur l'interaction entre le rayonnement cosmique et les perturbations solaires. Cette tâche a été prise en charge par le ministère responsable (boursier postdoctoral et personnel du Centre canadien de météo spatiale de Ressources naturelles Canada). L'autre partie du projet était expérimentale et consistait à évaluer la nécessité de doter le Canada d'un détecteur de muons, à étudier la technologie existante et à concevoir un détecteur d'essai. Cette tâche a été confiée à un entrepreneur, c.-à-d. le groupe d'étudiants, de boursiers postdoctoraux et de professeurs du département de physique de l'Université Carleton.

Les recherches ont permis de décrire deux types de précurseurs, tous deux associés à une variation du flux du rayonnement cosmique due aux interactions avec les perturbations solaires en propagation. L'équation du transport fondée sur la physique a été analysée en se basant sur des données obtenues au moyen du télescope à muons de Nagoya et sur les mesures de la perturbation solaire. La validité du modèle de diffusion pour l'interaction entre le rayonnement cosmique et les perturbations solaires a été vérifiée.

Il a été établi que le réseau international de détecteurs de muons en place comporte une lacune dans sa couverture de la région nord-américaine. Il est donc important de doter le Canada d'un détecteur de muons. La technologie existante a été évaluée et un détecteur de muons a été construit à l'essai. Les données fournies par ce détecteur ont été analysées. Cela a permis de confirmer le stade avancé de préparation de cette technologie ainsi que de fournir des spécifications de conception et des recommandations détaillées pour de futurs travaux.

Recherches futures : L'analyse faite des techniques de pointe d'utilisation des détecteurs de muons pour la prévision des conditions spatiométéorologiques extrêmes ainsi que les progrès réalisés dans ce domaine de recherche montrent que notre niveau de connaissances de même que la préparation technologique sont suffisamment élevés pour qu'il soit possible d'élaborer un prototype de système de prévision des conditions spatiométéorologiques au moyen d'un réseau de détecteurs de muons couvrant tout le ciel.

Importance : La conception d'un détecteur de muons proto-opérationnel au Canada permettra de combler la lacune dans la couverture internationale et donc d'apporter une contribution de premier plan à l'utilisation proto-opérationnelle de la mesure des muons. Cela améliorera les prévisions éloignées des conditions spatiométéorologiques extrêmes.

Table of contents

List of figures

List of tables

Acknowledgments

We are thankful to all the participants of the Canadian Muon Workshop including Prof. Kazuoki Munakata, Dr. Victor Yanke, Dr. Eugenia Eroshenko, Prof. John Bieber, Dr. Frank Jansen, Prof. Lev Dorman, Prof. David Thompson, and Dr. Ken Tapping.

We also thank Dr. David Boteler, Dr. Takao Kuwabara, Dr. Anatoly Belov, Prof. Karel Kudela and Dr. Zenjiro Fujii for useful discussions.

We express gratitude to Principal Investigators for possibility to use data from Nagoya muon telescope, McMurdo neutron station and ACE Satellite Mission.

1 Introduction

1.1 Space weather hazards to technological infrastructure

The sequence of physical processes, beginning at the Sun and ultimately affecting human activities on Earth and in space is called *space weather*. Solar eruptions, accompanied by solar flares, create disturbances propagating toward the Earth and ultimately affecting the near-Earth environment and space-borne and ground infrastructure.

Energetic particles from the solar eruptions affect satellites causing anomalies or equipment damage that can put the satellite out of operation. These particles also increase ionization in the ionosphere, which affects satellite communication and navigation (GPS) signals and can block HF radio communication in high Arctic for several days. The geomagnetic storms that follow the solar eruptions directly affect operations that use the magnetic field, such as magnetic surveys, directional drilling, or compass use. These disturbances also produce currents in ground conducting networks (power grids, pipelines, submarine cables, etc) interfering with normal operations of these infrastructure (see Fig. 1).

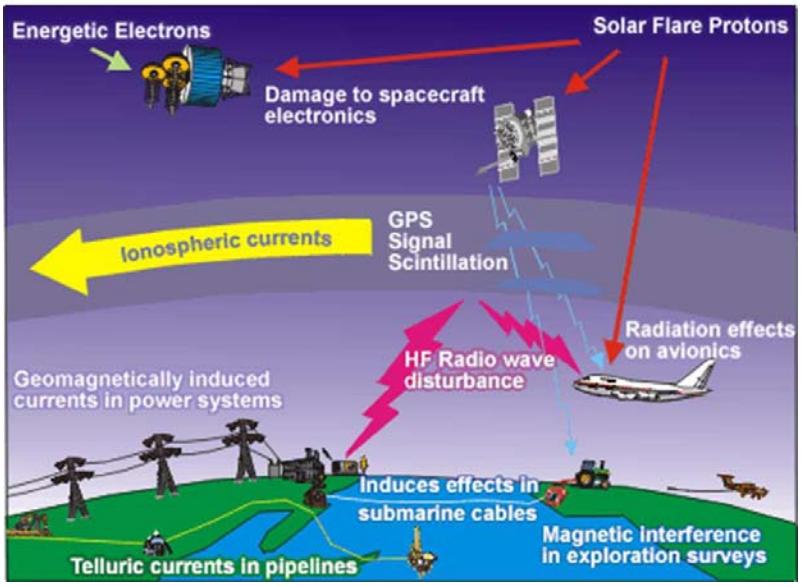

Figure 1: Impacts of extreme space weather on engineered systems and infrastructure (courtesy of Canadian Space Weather Forecast Centre [1: CSWFC]).

One of the most important for modern society and the most severely affected critical infrastructure is the electric power distribution system. Currents produced by geomagnetic storms can cause severe damage to critical components of the electrical power grid (e.g. during the Hydro Quebec blackout of March 1989). Many of these critical components do not have spares and it might require up to one year to manufacture and significant expertise to install these parts. A 2008 US National Academic of Sciences study concluded that up to one third of the US could lose electricity for 4 to 10 years due to extreme space weather events.

Modern society is becoming more and more dependent on technological systems which could be harmfully affected by extreme space weather events [2: Trichtchenko et al., 2012]. Sufficient early warning of an approaching disturbance would allow critical infrastructure (CI) operators (e.g. power grid operators, Hydro One, Hydro Quebec, etc) take protective measures (e.g. put spare generating capacity online). Unfortunately, reliable warnings are not currently available. Observations of the Sun's surface (images in different wavelengths) can provide up to three days warning, but with extremely poor reliability; errors can be as large as 12 hours and the rate of false alarms is high. The NASA ACE satellite can provide more detailed data on the approaching solar disturbance and up to 30 minutes warning due to its location close to the Earth, but this time is generally insufficient for CI operators.

The primary objective of the study is to improve the protection of Canadian CI from solar disturbances. It determines the feasibility of obtaining timely warning of extreme space weather conditions by using ground-based measurements of cosmic-ray-induced muons.

The feasibility study is based on the recent scientific evidence that the signatures of the approaching solar disturbance could be seen in the characteristics of the flux of muons produced in Earth's atmosphere by Galactic Cosmic Rays (GCRs). It is currently accepted that GCRs are deflected away from the Earth by the magnetic field of a solar disturbance, so a sudden decrease in the normal flux of neutrons and muons on the ground can indicate that a solar disturbance is approaching Earth. A ground-based Muon Telescope (MT) precisely measures trajectories of muons that are produced from GCR interactions in the Earth's upper atmosphere; thus, could possibly provide data for development of the early warning of an approaching solar disturbance.

1.2 Scope

The purpose of this study is to determine the efficacy of using ground-based measurements of cosmic-ray-produced muons to provide reliable, timely warning of extreme space weather conditions that can have severe impacts on Canada's critical infrastructure (CI).

The early warning requirements were determined as a result of discussion with CI operators and users to define the type of information they need (and when) in order to protect their CI assets. This information will help in the development of early warning systems that CI operators can use to maintain safe operation during extreme space weather events.

The efficacy study presented includes a literature review, workshop with leading experts, analysis of the available muon data, modelling and simulation of behaviour of the primary cosmic rays during their interaction with the solar disturbances and guidelines for future work. This study provides recommendations for developing ground-based muon telescopes and their supporting systems.

A capability roadmap describes the steps needed to develop the muon detector technology to produce reliable muon data and recommendations on the steps needed to develop the numerical model for the forecasting. In addition, the benefits of incorporating data from Canadian sites into the nascent Global Muon Detector Network (GMDN) are discussed.

For this project the specifications for muon telescopes (MT) were determined through a combination of modeling, simulation, test and evaluation by a contractor (researchers at Carleton

University), while theoretical part including analysis of the data available from currently operating muon telescopes has been done by the researchers from the Lead Department (NRCan).

1.3 Included work and deliverables

The project was divided into six work packages (WPs).

WP 1 is related to a survey of critical infrastructure representatives to assess the understanding of the impacts and readiness for extreme space weather, and to quantify their needs and requirements for early warning. The result on this package is summarized in Section 2.

WP 2 was aimed at reviewing the current situation with the use of muon detections for space weather applications [3: Kalugin et al., 2013]. This was achieved through a discussion with experts during Canadian Muon workshop and a literature review. The results are described in Sections 3 and 5.

Two work packages were associated with theoretical work, WP 3 and WP6. The first has been focused on investigations towards possibility to use muon data for early warning of extreme space weather. After reviewing the most up-to-date models in Section 3 (WP3), the possible mechanism to evaluate the interaction of the primary galactic cosmic rays with solar disturbance has been chosen.
The Work Package 6 provides results of applicability of obtained theoretical model. This includes obtaining the muon and solar disturbance (solar wind) parameters during extreme events for the last solar cycle. These parameters were used to test the chosen model of interaction of different parts of solar disturbances (CMEs) with galactic cosmic rays in order to evaluate the applicability and expected results of the models. The output of this work is described in Section 4.

Experimental part of the work (WP 4) was performed by a contractor (Professors, a postdoctoral fellow and a group of students of Physics Department, Carleton University). Here we made an assessment of different muon detector systems and their performance requirements for possible use in an Extreme Space Weather Events (ESW) early warning system. The small scale test telescope has been designed based on computer simulations. The system has been constructed, tested and the short experiments were performed. The experience obtained by operating a small muon telescope is an important input into the technology assessment. The output from this work is described in Section 6.

WP 5 developed a roadmap (steps) for the development of Canadian muon detectors for operational use as a component of an early warning system for space weather disturbances. The Roadmap includes recommendations for the algorithms that analyze the muon telescope data and the communications systems that support the telescopes so that the muon data can be sent to space weather forecasters who will fuse the muon data with other data streams to provide the best possible space weather forecasts to CI operators. This Roadmap also recommends how to achieve integration of Canadian muon detectors into the GMDN. There are currently no North American sites in the GMDN and it is expected that the addition of one or more Canadian sites would significantly improve the reliability and timeliness of the early warning from the GMDN. The output is described in Section 7.

2 Impacts on power grids and CI requirements

Of the four consequences of space weather, such as changes to the space environment, atmospheric expansion, ionospheric disturbance and geomagnetic disturbance (GMD), 90 percent of the immediate impacts are related to the energy sector, which then cascades to all other sectors [4: Trichtchenko et al., 2011].

This chapter first reviews the effects of geomagnetic disturbance or geomagnetic storms on power system components and the operation of the whole system. Then the strategies used to minimize these effects by power industry representatives will be listed and discussed.

2.1 Response of power grid components to extreme space weather

During geomagnetic disturbances caused by the interaction of the solar eruption with the Earth's magnetic field, strong variations of the ground electric fields drive Geomagnetically Induced Currents (GIC) along power lines and through power transformers to ground. Compared to normal ac frequencies the GIC appear to the power system as quasi-dc currents and can saturate transformers and create high levels of harmonics which, in some instances, can trigger the operation of protective relays and overheat large transformers.

High voltage power distribution is provided by a network of 3-phase transmission lines connected between Y-configuration transformers as shown in Fig. 2. During normal operation the different phase currents in each winding of the transformer add to zero at the centre (neutral) point of the Y and there is no AC current flow along the connection to ground. However, when the AC supply is unbalanced or there are fault conditions, such as a broken conductor or a lightning strike on the line, the currents do not cancel at the neutral point and the connection to ground is needed to provide a safe discharge path. The presence of this neutral-ground connection allows geomagnetically induced currents to flow to ground through the transformer windings which causes a variety of problems.

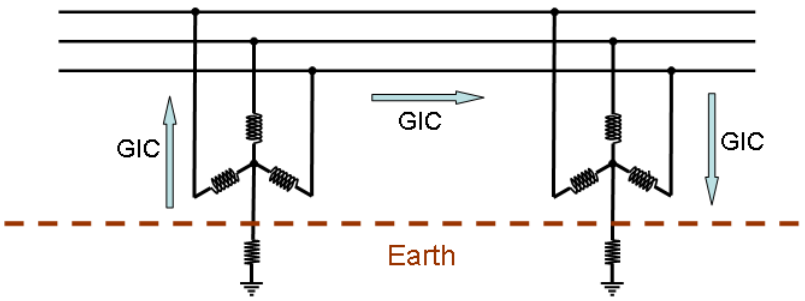

Figure 2: Geo- electric fields drive geomagnetically induced currents (GIC) along the lines and to/from ground through transformer windings and neutral-ground connections.

The GIC flowing through the transformer winding produces extra magnetisation which, during the half-cycles when the AC magnetisation is in the same direction, can saturate the core of the transformer. The key factor in determining the level of impact of geomagnetic storm on a power system is the degree to which the GIC cause saturation of the transformer core. The hysteresis curve of the transformer is shown by three straight lines in Figure 3. Normal regime is located within the central region where the transformer is unsaturated. If the magnetic flux increases past the "knee" in the curve the transformer core is saturated and the slope of the hysteresis curve changes dramatically. The "knee" in the curve is typically at 1.1 times the normal operating peak flux value.

When a transformer experiences a DC current such as GIC during the geomagnetic storm, the operating point of the transformer is shifted. If this takes the AC flux past the knee in the hysteresis curve the transformer will be in saturation for part of each AC cycle, resulting in a spiky current waveform as shown in Fig. 3. Spiky AC waveform with increased harmonic levels can cause misoperation of relays and other equipment on the system and lead to problems ranging from trip-outs of individual lines to collapse of the whole system.

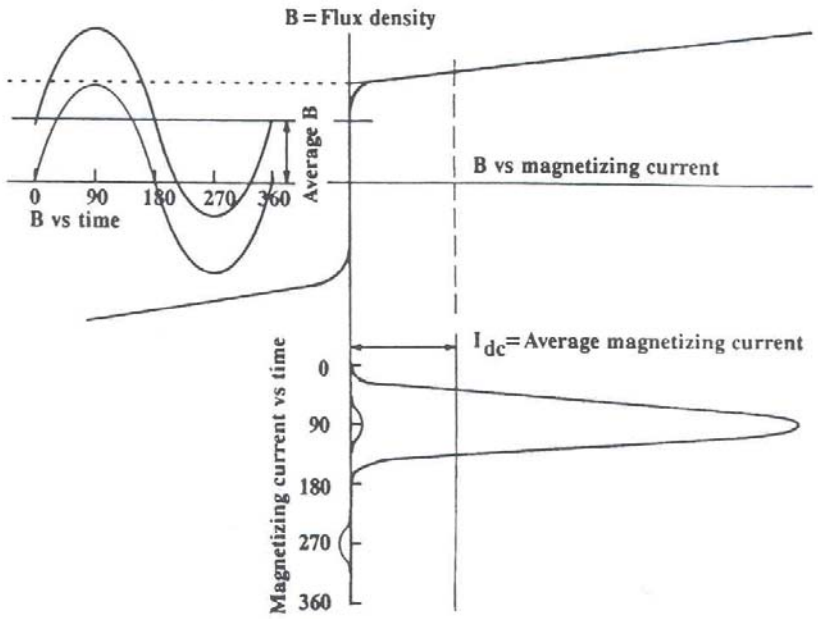

Figure 3: Hysteresis curve for a single phase power transformer showing the spiky current waveform produced when the flux offset takes the transformer into saturation [5: Boldu & Aubin, 1978].

Saturation of the transformer core causes increased transformer heating because of the extra electrical eddy currents produced in the transformer core and structural supports. The large thermal mass of a high voltage power transformer means that this heating produces a negligible change in the overall transformer temperature. However, localised hot spots can occur and cause damage to the transformer windings.

The harmonics produced by GIC can interfere with operation of transformer differential relays. Differential relays are designed to detect a departure from the normal ratio of input and output

currents, which is usually indicative of a fault in the transformer. The additional harmonics resulting from transformer saturation due to GIC can cause misoperation of relays.

The power delivered to customers usually has the AC current in phase with the AC voltage and is termed “real” power. In contrast the AC magnetising current drawn by the transformers is out of phase with the AC voltage and this combination is termed “reactive power” (also referred to as VAR standing for volts multiplied by amps reactive). Reactive power has to be supplied to the system in order for the transformers to operate correctly. This can be done either by dedicated generators or by Static VAR Compensators (SVC) that convert real power to reactive power. When there is insufficient reactive power to maintain voltage stability, voltage collapse may occur causing system outages and interruption of service to customers.

Saturation of transformer during space weather event increases their magnetising current and, by association, increases the reactive power demand. Because of the widespread nature of GIC many transformers on a power system can be going into saturation simultaneously, creating a significant increase in the total reactive power demand on the system. During the March 1989 magnetic storm GIC in the Hydro-Quebec system caused transformer saturation and increased reactive power demand. At the same time harmonics caused SVCs relays to trip removing a source of reactive power, leading to voltage collapse and the system-wide blackout.

2.2 User requirements

The impact of space weather on apower grid can be reduced by several engineering approaches, such as DC blocking capacitors, special transformer design. These are not only very costly, but also cannot completely eliminate the unwanted impacts.

In addition to the engineering approaches, special operating procedures can be used to maintain system operation during geomagnetic disturbances. The Northeast Power Coordinating Council procedures [6: NPCC, 2000] list a range of actions that may be taken by system operators including: discontinuing maintenance work and restoring out of service lines, reducing the load on critical transmission links to 90% of their normal safe limit, reduce loading on generators to provide reserve power capacity, and increase the reserve capacity for reactive power.

These operating procedures involve a penalty, either in terms of compromised safety margins, or because of lost revenue because of power transfer limits. Thus, their implementation requires **timely and accurate notification of space weather conditions** likely to cause large impacts.

In the aftermath of the March 1989 Hydro Quebec blackout studies have been done and alerting requirements were defined by IEEE Working Group on Geomagnetic Disturbance in 1993 [7: Molinsky, 2002]. The fact that reliable data on the solar disturbance can only be acquired from ACE satellite which is only 1 hour prior the geomagnetic disturbance on Earth has limited the requirements to accurate advanced warnings of 1 hour (or more). This warning should include the following parameters of the disturbance: start time, maximum severity and regions affected, end time and level of uncertainty.

Recently, in 2012, the North American Electricity Reliability Council (NERC) has developed the more comprehensive and general set of the operating procedures to mitigate GIC. These

requirements are based on analysis of previous cases of recorded effects of space weather events on power grids. In order to enhance the resilience of critical infrastructure, analysis of the estimation of a 100-year hypothetical extreme event has been included as Design Basis Credible Threat (DBCT).

The recommendations were addressed to multiple organisations and are divided into four different classes:

1. Improve tools for industry planners to develop mitigation strategies, such as vulnerability assessment for different components of power grid; produce a set of reference storms; develop tools to model GIC flow; develop transformer specification to be able to withstand the large GIC.

2. Improve tools for system operators to manage GMD impacts, such as guidelines to monitor and mitigate GIC and **get improved warnings and alerts from** NOAA and **NRCan** in order to enhance GMD notification procedures.

3. Education and information exchange between researchers and industry.

4. Review the need to enhance the NERC reliability standards.

With regard to the functional areas of situational awareness and forecasting, the recommendation was "**Forecasting and early warning of GMD are vital components** of system defense against severe GMD. ….Maintaining and **enhancing this capability** is important to system operators…"[8: NERC, 2012].

Although the impacts on the power systems are immediate, in enhancing resilience to an event, warnings are major enablers. Whereas a major earthquake can strike without warning, an extreme space weather event is detectable hours or days before its most widespread effects strike the earth. This raises the possibility of implementing mitigation action.

Although a number of our critical infrastructure sectors—such as transportation, finance, communications and energy—are improving the resiliency of their infrastructure, it is still not assured that such measures will sufficiently offset the effects of a major space weather event. **The ability to be prepared in advance is directly dependent on the ability to provide advanced warnings and reliable forecasts**. To increase the level of preparedness, **reliable forecasts of several days ahead on the start, duration and severity** of the impacts will significantly increase the abilities to cope with these impacts for potentially protracted periods

3 CR and space weather forecasting. Overview

3.1 Introduction

The primary cosmic ray (CR) flux (galactic in origin) is composed mainly of protons (79%), with a further 15% being alpha particles (He nuclei). The remaining 6% is made up of heavier nuclei in decreasingly smaller fractions as their atomic number increases up to iron. The energy (E) spectrum is flat around 1 GeV and drops off above 3 GeV as $E^{-2.7}$. When these primary particles impinge on the outer atmosphere starting around 25km above the surface, they interact with the with the oxygen and nitrogen molecules producing secondary hadronic and electromagnetic showers (Fig. 4). Among these secondary CR particles, are muons (produced by primaries with energies of ~50GeV) and neutrons (primaries ~ 10 GeV). These are two main species observed by muon detectors (often called muon telescopes) and neutron monitors respectively. The neutron monitors are omnidirectional while the muon telescopes are multidirectional particle detectors. Thus, muon and neutron observations are complementary to each other in terms of energies of primary CR and directional resolution.

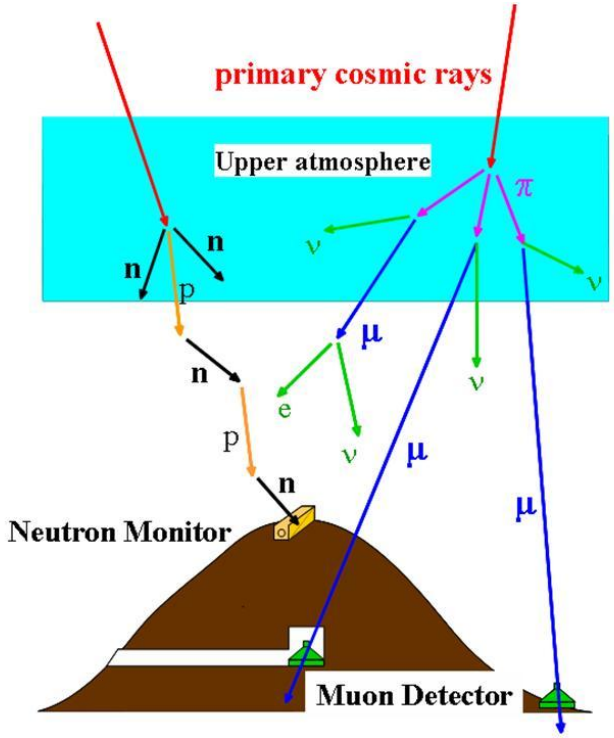

Figure 4: Cosmic ray shower.

It is important to understand that, due to the geometry of the geomagnetic field, not all the CR particles can reach Earth. This effect can be described by *rigidity*. By definition, rigidity is the product of magnetic field intensity and Larmor radius (i.e. it is inversely proportional to the curvature of the path of a charged particle traversing the geomagnetic field) [9: Rossi, 1964, p. 55]. Therefore the rigidities of primary CR particles responsible for the counting rates registered

at ground level should have values larger than the so-called *cut-off rigidity* which describes the magnetic shielding provided by the geomagnetic field against the arrival of charged CR particles [10: Humble et al., 1985]. In addition, owing to the particle motion in the geomagnetic field, each ground level detector is capable of recording particles produced by primaries originating from a limited set of directions in space, which is called the *asymptotic cone of viewing* [11: Plainaki et al., 2009]; the directions themselves are called *asymptotic directions* [12: Duldig, 2001] (for details, see Section 5). One more characteristic of the motion of charged particle in magnetic field is so-called *pitch-angle*, i.e. angle between the vector of particle velocity and the direction of the magnetic field.

3.2 Variations in the cosmic ray flux

Most primary and secondary particles are absorbed in the atmosphere, where the flux builds to a maximum at around 15km, before dropping off until it reaches the surface. Muons, produced in pion decays around 15km, form the bulk of the particle species detected at the surface ~70%, with the rest being mainly electrons. The energy spectrum at the surface is flat up to about 3 GeV, and then drops off at a faster rate than the primary spectrum i.e. at ~ $E^{-3.7}$. The muons then have an average momentum of around 2 – 4 GeV/c and show a $\cos^2 \theta$ variation around the vertical (θ=0).

Their flux is fairly constant at a particular height above sea level and magnetic latitude. Throughout the day it displays a 1% diurnal variation and a variation of similar magnitude with the rotation of the Sun (27 days variations). Larger local effects can be due to variations of local atmospheric pressure and temperature (determining the density of the atmosphere) or cloud cover. Changes on a longer timescale include the 11 year solar cycle, which can change the flux by up to 15%, and the reversal of the sun's magnetic field every 22 years.

In addition to the periodic variations noted above, shorter term non-periodic variations ranging from a few hours to a few days have been observed. One of the most noticeable results of the interaction of CRs with solar disturbances is a *Forbush Decrease* (FD) which is characterized by reductions of their flux up to 25-30% over a few days. These decreases in the cosmic ray flux were first observed by S.E. Forbush in the 1930's [13: Forbush, 1938].

Solar eruption seen in the solar corona, named *Coronal Mass Ejection* (*CME*, see the Glossary, on p.93) propagates and interacts with the interplanetary media (solar wind) forming so-called *Interplanetary Coronal Mass Ejection (ICME)*, which might consist of several distinctive parts that differ in their magnetic and particle composition and parameters. Such parts of ICME are sheath (area of fast magnetic field variations) and magnetic cloud or ejecta (depleted density and increased magnetic field) with preceded *interplanetary (IP)* shocks. There can be many IP shocks during the passage of ICME. Their interaction with the Earth's magnetic field causes shock-type geomagnetic disturbances seen on the ground as well. The one which is most closely preceded geomagnetic storm traditionally called *Storm Sudden Commencement* (*SSC*).

It is now understood that the FDs and strong geomagnetic storms are produced by the interaction of ICME with solar wind and magnetosphere of the Earth.

In three papers in the late '40's and early '50's [14: Forbush, 1946; 15: Forbush, 1950; 16: Forbush, 1959;] Scott Forbush reported on several unusual increases and decreases to the cosmic ray intensity. These occurred simultaneously at several different ground based stations, the changes seemed to be larger where the stations were nearer to the pole, and there was also an

elevation effect. The increases ranged between 20 to 85% at one station (Cheltenham, Maryland) they usually lasted a few hours, and were followed by a period of reduced activity for a day or so.

3.3 Cosmic rays precursors of the geomagnetic activity

It has been recently shown that in addition to the Forbush Decreases coinciding in time with the geomagnetic storm, several types of precursors can be observed by muon detectors which gives significantly longer advanced time than currently existing warning of 0.5-1 hr ahead by detection of ICME at ACE spacecraft (~ 8 hours [17: Leerungnavarat et al., 2003], or even 12 to 25 hours [18: Munakata et al., 2000] before the storm). These precursors are of two types: loss cone anisotropy (i.e. deficit) and enhanced variance of muon flux, which are described below.

Variations of the primary CRs with energies up to ~100 GeV experienced in response to passing solar disturbances are schematically presented in Fig. 5 [19: Asipenka et al., 2009]. The Interplanetary CME propagates toward the Earth generating Interplanetary Shocks. Behind (downstream) of shocks there is a depleted region (FD). The numerical modelling [20: Ruffolo, 1999; 18: Munakata 2000] for the pitch angle distribution of charged particles travelling across the interplanetary shock predicted a depletion of particle intensity in a narrow loss cone upstream of the shock (blue line in Fig.5).

Another type of precursor corresponds to the intensity increase or its large fluctuations and term Enhanced Variability precursor (EV). The possible mechanism for this precursor is reflection of the ambient upstream primary CR particles of larger pitch angles from the IP shocks.

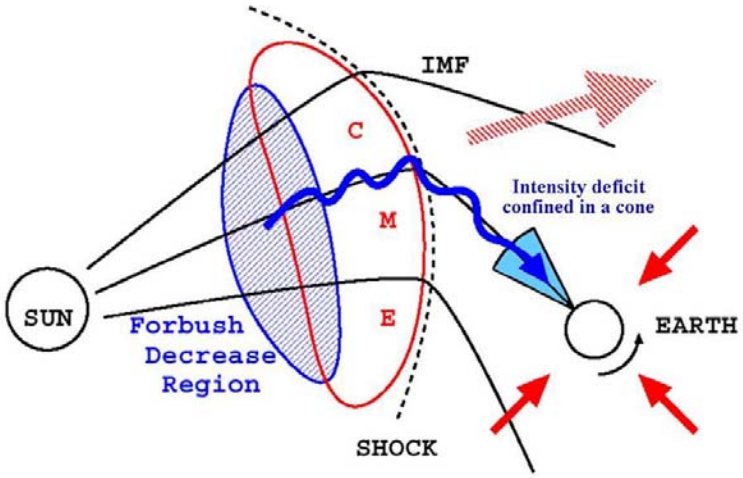

Figure 5: The effects of a shock driven by ICME [19: Asipenka et al., 2009].

Figure 6 (from [17: Leerungnavarat et al., 2003]) displays results from two surveys of CR precursors. In particular, the histogram on the left is given for 22 large storms surveyed with surface muon telescopes in [18: Munakata et al., 2000] and the right histogram is for 14 "major" geomagnetic storms surveyed with a network of neutron monitors [21: Belov et al., 2001]. The histograms display the lead time of the precursor relative to the SSC associated with the shock

driven by ICME. The typical primary CR energy producing the secondary particles modulated by FD is taken as ~ 30 GeV for muon detectors and ~ 10 GeV for neutron monitors.

It follows from Fig. 6 that the muon detectors observed precursors in 15 of 22 large storms and that the lead time of precursors relative to the SSC is typically 8 hours and can be as long as 12 hours. This is more than the lead time of precursors for neutron monitors and is sufficient to be useful for space weather forecasting.

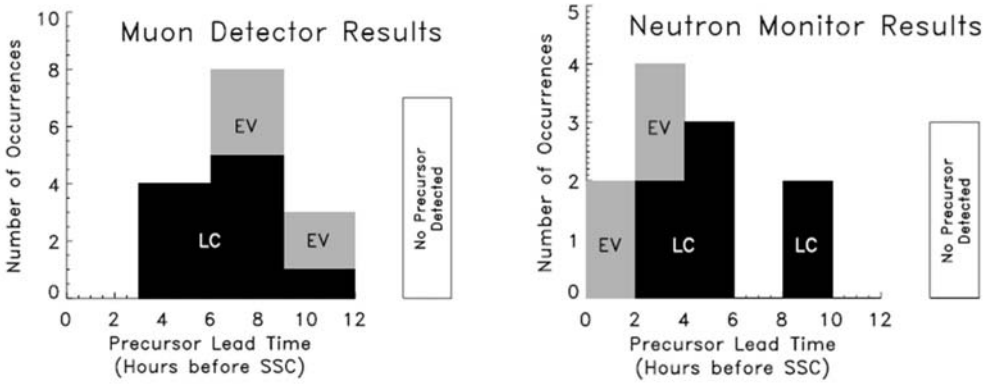

Figure 6: Histograms of the earliest observation of precursors by muon detectors (on the left) and neutron monitors (on the right) before SSC [17: Leerungnavarat et al., 2003].

The difference in the lead time of EV for muon detectors and neutron monitors is offered in [17: Leerungnavarat et al., 2003] in terms of a power-law index q of the reduced power spectrum as a function of wavenumber which affects the transport of CRs [22: Jokipii, 1966]. Specifically, it was found that CRs of ~30GeV, to which a muon detector is sensitive, experience a substantially lower q-value than CRs at ~10 GeV, as measured by neutron monitors (q = 0.5 and q = 1.1 respectively). As a result the parallel mean free path for IP scattering and a decay length for the former are larger than for the latter and as a consequence, the lead time provided by muon detectors is larger than by neutron monitors.

In addition, a comparison between LC and EV precursors in each histogram in Fig. 6 shows that the LC effect is more easily recognized in the data and thus more useful as an indicator of impending space weather disturbances.

The same conclusions can be made from Fig. 7 which shows the results from an analysis of 133 geomagnetic storms between March 2001 and December 2007 [23: Rockenbach et al., 2009]. One can see on the left panel that 86% of the SS, 30% of the IS and 15% of the MS had precursors observed by the GMDN with the number of NP events decreasing with the magnetic storm intensity. The right panel illustrates a prediction capability of GMDN and shows that LC precursors were observed more frequently between 9 and 12 hours before the SSC. Remarkably, the LC precursor of a super storm was observed as early as 18 hours prior to the SSC. It is worth mentioning that since strong geomagnetic storms are rare, the statistics should be viewed with caution.

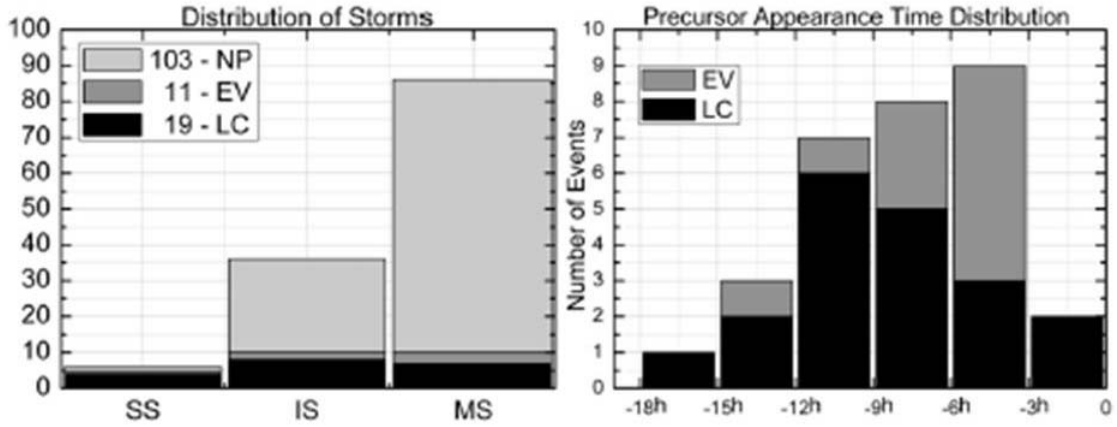

Figure 7: Histograms of magnetic storms intensity and the appearance time of LC and EV precursors; "NP" represents no-precursor cases; MS – Moderate Storms, IS – Intense Storms, and SS – Super Storms [23: Rockenbach et al., 2009].

3.4 "Loss-cone" precursors in depth

3.4.1 First-order anisotropy analysis for searching for precursors

We describe a methodology [24: Rockenbach et al., 2011] used to analyze LC precursors and highlighted in [25: Trichtchenko & Kalugin, 2011]. Let us consider a count rate of CR muons corrected for the atmospheric pressure variation, called intensity. The LC precursor is observed as a deficit of intensity when the sunward IMF direction is monitored by the muon detector. To provide an accurate analysis of LC events and improve the precursor observations, it is necessary to properly remove the contribution from the diurnal anisotropy (DA), which always exists in space with an amplitude comparable to the intensity deficit because of the LC anisotropy [26: Fushishita et al., 2010]. The DA, when observed by a detector on the Earth, produces a diurnal variation which is generally different in different directional channels. We derive the anisotropy by fitting the following function

$$\begin{aligned} I_{i,j}^{fit}(t) = I_{i,j}^{0}(t) &+ \xi_x^{GEO}(t)\left(c_{1i,j}^{1}\cos(\omega t_i) - s_{1i,j}^{1}\sin(\omega t_i)\right) \\ &+ \xi_y^{GEO}(t)\left(s_{1i,j}^{1}\cos(\omega t_i) + c_{1i,j}^{1}\sin(\omega t_i)\right) \\ &+ \xi_z^{GEO}(t)\, c_{1i,j}^{0} \end{aligned} \qquad (1)$$

to the observed hourly count rate $I_{i,j}^{obs}(t)$ of muons at universal time t in the j-th directional channel of the i-th muon detector [27: Okazaki et al., 2008; 28: Kuwabara et al., 2004]. In Eq. (1) t_i is the local time at the location of the i-th detector and $\omega = \pi/12$. The coupling coefficients $c_{1i,j}^{1}$, $s_{1i,j}^{1}$ and $c_{1i,j}^{0}$ relate the observed muon intensity to the primary CR intensity in free space [28: Kuwabara et al., 2004]; they are calculated by assuming a rigidity independent anisotropy.

The best-fit parameters $\xi_x^{GEO}(t)$, $\xi_y^{GEO}(t)$ and $\xi_z^{GEO}(t)$ denote three components of the anisotropy which are defined in a local geographical coordinate system (GEO), in which the *z*-axis is directed toward geographic north, the *x*-axis is in the equatorial plane and directed to the zenith of a point on the Earth equator at 00:00 local time, and the *y*-axis completes the right-handed coordinate set. Thus, for example, $\xi_z^{GEO}(t)$ represents the north-south anisotropy [27: Okazaki et al., 2008]. These best-fit parameters along with $I_{i,j}^0(t)$ are determined by minimizing *S* defined, for example, in the case of one detector with two viewing directions, as

$$S = \sqrt{\frac{1}{M}\sum_{m=1}^{M} s^2(t_m)} = \sqrt{\frac{1}{2M}\sum_{m=1}^{M}\left[\frac{\left(I_{1,1}^{obs}(t_m) - I_{1,1}^{fit}(t_m)\right)^2}{\sigma_{1,1}^2} + \frac{\left(I_{1,2}^{obs}(t_m) - I_{1,2}^{fit}(t_m)\right)^2}{\sigma_{1,2}^2}\right]},$$

where $s(t_m)$ is hourly residual of the best fitting at the time $t = t_m$, M is the total number of hours used for the best fit calculations and $\sigma_{i,j}$ is the count rate error for the (*i,j*) directional channel.

Now we define a part of $I_{i,j}^{obs}(t)$, associated with the DA, as follows [24: Rockenbach et al., 2011]

$$\begin{aligned} I_{i,j}^{DA}(t) = \bar{I}_{i,j}^{0}(t) &+ \bar{\xi}_x^{GEO}(t)\left(c_{1i,j}^1 \cos(\omega t_i) - s_{1i,j}^1 \sin(\omega t_i)\right) \\ &+ \bar{\xi}_y^{GEO}(t)\left(s_{1i,j}^1 \cos(\omega t_i) + c_{1i,j}^1 \sin(\omega t_i)\right) \\ &+ \bar{\xi}_z^{GEO}(t)\; c_{1i,j}^0 \end{aligned} \qquad (2)$$

The best-fit parameters in Eq. (2) are defined as the 12-hours Trailing Moving Averages (TMAs), i.e.

$$\bar{I}_{i,j}^{0}(t) = \frac{1}{12}\sum_{t-11}^{t} I_{i,j}^0(t)\,,$$

$$\bar{\xi}_x^{GEO}(t) = \frac{1}{12}\sum_{t-11}^{t} \xi_x^{GEO}(t)\,,$$

$$\bar{\xi}_y^{GEO}(t) = \frac{1}{12}\sum_{t-11}^{t} \xi_y^{GEO}(t)\,,$$

$$\bar{\xi}_z^{GEO}(t) = \frac{1}{12}\sum_{t-11}^{t} \xi_z^{GEO}(t)\,.$$

Comparisons between the 12-hours and the 24-hours TMA of the best-fit parameters show that the former are better than the latter for observation of the LC effect [24: Rockenbach et al., 2011].

To remove the contribution of the DA from the data for precise analysis of the LC precursor, we subtract $I_{i,j}^{DA}(t)$, defined by Eq. (2), from the observed intensity $I_{i,j}^{obs}(t)$

$$\Delta I_{i,j}^{cal}(t) = I_{i,j}^{obs}(t) - I_{i,j}^{DA}(t). \quad (3)$$

As a result we obtain the directional intensity distribution free from the DA. Moreover, to visualize the precursor signatures more clearly, we suppress the statistical fluctuations which are larger in the inclined channels. For this purpose, instead of $\Delta I_{i,j}^{cal}(t)$, we use the "significance" defined as [24: Rockenbach et al., 2011]

$$s_{i,j}^{cal}(t) = \frac{\Delta I_{i,j}^{cal}(t)}{\sigma_{i,j}} = \frac{I_{i,j}^{obs}(t) - I_{i,j}^{DA}(t)}{\sigma_{i,j}} \ .$$

Remark 1. Since the difference $\Delta I_{i,j}^{cal}(t)$ is calculated using TMAs, it is not affected by the variation occurring after time *t* [26: Fushishita et al., 2010]. This is important for real time predictions in space weather forecasting [24: Rockenbach et al., 2011].

Remark 2. In some works, to avoid spurious diurnal variation, instead of $I_{i,j}^{obs}(t)$, the following is used

$$\widetilde{I}_{i,j}^{obs}(t) = I_{i,j}^{obs}(t) \frac{\bar{I}_{1,1}^{obs}(t)}{\bar{I}_{i,j}^{obs}(t)}$$

with the 24hr TMAs [27: Okazaki et al., 2008; 28: Kuwabara et al., 2004].

For the analysis of muon intensity distributions the calculated values of $\Delta I_{i,j}^{cal}(t)$ can be represented in two ways. One of them is to show the results for all of the directional channels in the form of a two-dimensional color contour map where the latitude of incident direction spanning from the north (upper) and south (lower) directions in the field of view is scaled along the vertical axis, while the longitude from the east (right) and west (left) directions is on the horizontal axis. Additionally, in the map there are contour lines of pitch angle measured from the observed IMF direction; the pitch angle is calculated for CRs incident to each directional channel with the median primary energy appropriate to that channel [29: Munakata et al., 2005]. As an example, intensity distributions observed in 121 directional channels with a muon hodoscope at Mt. Noricura (Japan) over 6 hours preceding the SSC are shown in Fig. 8 [25: Munakata et al., 2005] where the LC precursor can be identified by a region of the deficit intensity (displayed by blue color) localized around small pitch angle. Similar intensity distributions were analyzed in [30: Nonaka et al., 2003) and [26: Fushishita et al., 2010].

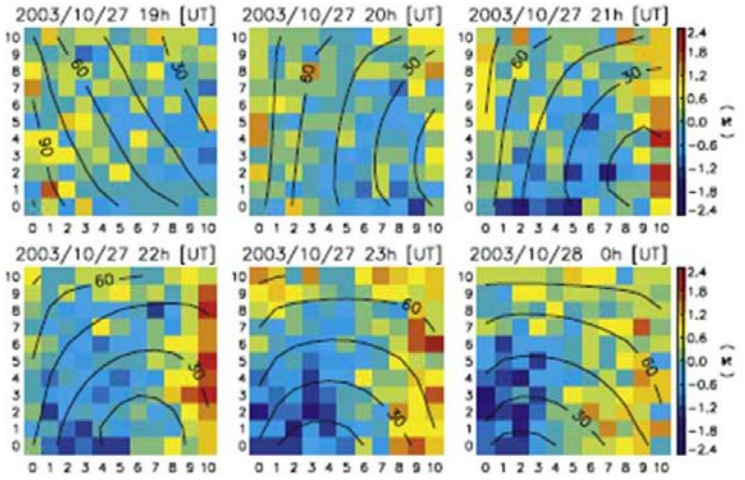

Figure 8: The intensity distributions observed with a muon hodoscope at Mt. Noricura (Japan) over 6 hours preceding SSC. In the panels the LC precursor relates to the region of deficit intensity displayed by blue color [29: Munakata et al., 2005].

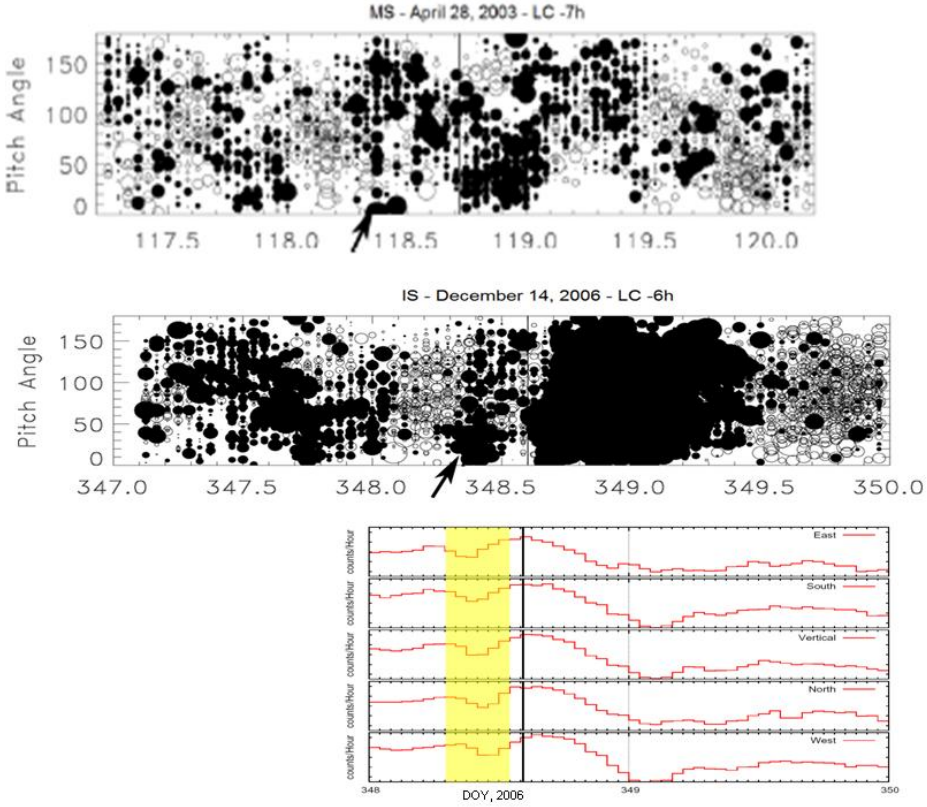

Figure 9: Examples of LC precursors observed by São Martinho da Serra's muon telescope on April 28, 2003 [23: Rockenbach et al., 2009] and on December 14, 2006 [31: Schuch et al., 2009; 24: Rockenbach et al., 2011] at the top and the bottom respectively.

Another way to represent muon intensity relative to the omnidirectional intensity is to use a two-dimensional map with measurements along two coordinate axes of time and pitch angle. An implementation of this technique is illustrated in Fig. 9 which shows the pitch angle distribution of CR intensity vs. time observed by São Martinho da Serra's muon telescope during the geomagnetic storm on April 28, 2003 [23: Rockenbach et al., 2009] and on December 14, 2006 [31: Schuch et al., 2009; 24: Rockenbach et al., 2011] at the top and the bottom respectively. The pitch angle of each direction of viewing is defined as the angle between the sunward IMF direction and the viewing direction of *j*-th directional telescope in *i*-th muon detector of the GMDN [18: Munakata et al., 2000]. The open and solid circles represent, respectively, an excess and deficit of CR intensity relative to the DA intensity in accordance with Eq. (3), and the diameter of each circle is proportional to the magnitude of deficit or excess. In the top figure, the LC effect can be seen clearly approximately 7 hours before the SSC shown by the vertical line and can serve as a precursor of the storm. At the bottom, additionally, is shown the intensity recorded with five single channels. One can see that LC has 3hr duration implying about 45^{o} width and onsets first in the eastward viewing channel, then in the vertical and westward channels, as expected for an anisotropic depression of the CR intensity [31: Schuch et al., 2009].

3.4.2 Analysis of LC precursors for recent geomagnetic storms

Observations of galactic CR intensity during an LC precursor period related to an IP shock arrival on October 28, 2003 were obtained in [29: Munakata, et al., 2005]. The authors used a large single muon detector on the top of Mt. Norikura (Japan) and analyzed 121 directional channels which cover 360^{o} of the azimuth angle and 0^{o} to 55^{o} of the zenith angle. The estimated median energy of CR is in the range from 48 GeV (for the vertical channel) to 80 GeV (for the most inclined channel).

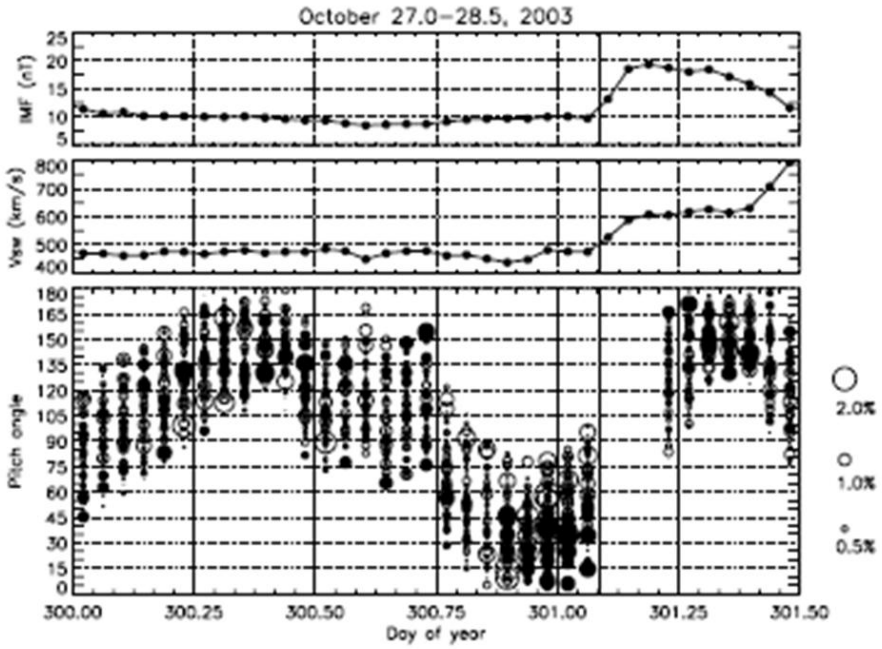

Figure 10: The IMF magnitude, solar wind velocity and muon intensity on October 27-28, 2003. [29: Munakata, et al., 2005].

In the lower panel in Fig. 10 is shown the intensity relative to the average muon intensity in each hour as a function of the pitch angle of the incident direction lagged by 1 hour as a rough correction for the solar wind transit time between the ACE satellite and the Earth. The pitch angle is calculated using one-hour averages of the ACE IMF data (level 2). Each circle represents an intensity of muons in a single directional channel relative to the omnidirectional intensity as a function of time (abscissa) and a pitch angle corresponding to the viewing direction (ordinate). Open and solid circles represent, respectively, an excess and deficit of the intensity, the diameter of a circle is proportional to the magnitude of the excess or deficit. The hourly data of the IMF magnitude and the solar wind velocity (V_{sw}) are shown in the top two plots of Fig. 10. One can see a signature of LC precursor (solid circles) localized around 0^o pitch angle during ~7 hours prior to the SSC indicated by a vertical line when IMF and V_{sw} experience a sharp increase. Based on analysis of a 2D map of the intensity, it was reported a lead time of 4.9 hr for the LC precursor. However, in [29: Munakata, et al., 2005] there were difficulties in establishing the direction in which the shock was propagating.

A precursor of FD related to an intense geomagnetic storm on December 14, 2006 was analyzed in [26: Fushishita et al., 2010].The data were obtained using the GMDN by monitoring the directional intensity of CR with median energies ranging from ~50GeV to ~110GeV. To analyze the data they improved the method in [29: Munakata, et al., 2005] by eliminating the influence of the diurnal anisotropy (DA) and by a better visualization of the signatures of CR precursors. As a result a significant LC signature was recorded by the Hobart detector at ~20 hr before SSC and then by the São Martinho detector with a larger amplitude at ~-6hr. A weak LC signature was first recorded more than a day prior to the SSC onset. This suggests that the LC precursor appeared only 7 hr after the CME eruption from the Sun, when the IP shock driven by the CME was located at 0.4 AU from the Sun (i.e. the average shock speed was about 2381 km/s).

Figures 11 and 12 relate to the event on December 14, 2006. At the time of the SSC the amplitude (-6.45%) of the LC anisotropy was more than twice the FD size (cf. Fig. 11 (b) and Fig. 12). The peak K_p index was 8+. The long lead time of the LC precursor was 15.6 hr. In [26: Fushishita et al., 2010], it was also found excess intensity from sunward IMF direction clearly observed during ~10 hr preceding the SSC. This was the first detailed observation with muon detectors of the precursor due to the shock reflected particles.

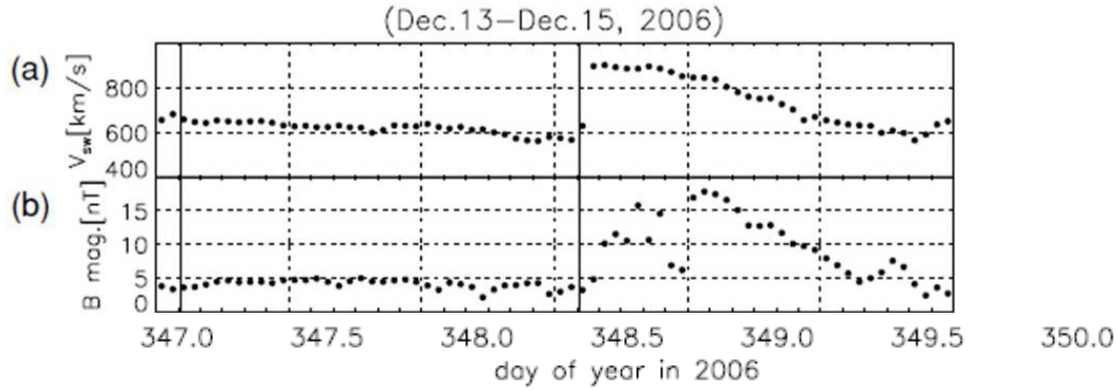

Figure 11: The hourly data (Level 2) of the solar wind velocity (a) and the IMF magnitude (b) measured by the ACE over a three-day period between 2006 December 13 and 15 [26: Fushishita et al., 2010].

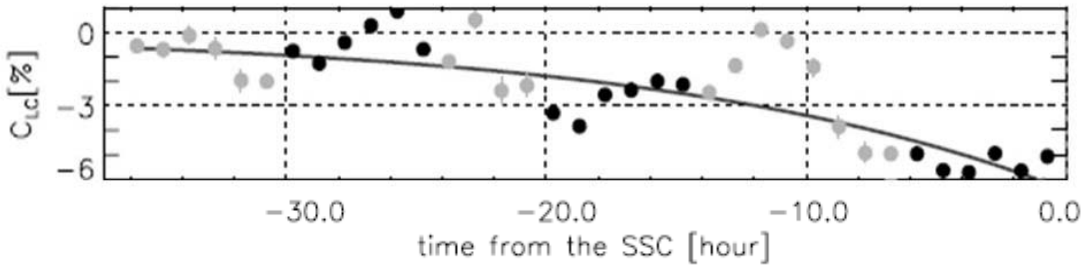

Figure 12: The amplitude of the LC anisotropy ($C_{LC}(t)$) with black and grey circles displaying the parameters obtained when the sunward IMF direction is monitored by the GMDN and is out of the Field of View (FOV) of the GMDN respectively. The solid line is an exponent-trial function of the time as the best fitting to the black circles [26: Fushishita et al., 2010].

In [23: Rockenbach et al., 2009], the authors analyzed 133 geomagnetic storms monitored by the GMDN from 2001 to 2007 to identify their precursors and found CR precursors to be observed on average 7.2 hours in advance of the SSC. These storms were sorted by their intensity using the Dst index in [24: Rockenbach et al., 2011] to find a dependence of a presence of storm precursors on the storm intensity as shown in the top of Table 1. The rest of the table shows, as an example, a particular storm from each class and an advanced time for LC precursor's observations by an indicated station prior to the SSC for the storm. It follows from Table 1 that the stronger the storm the longer the precursor time. However, this conclusion should be regarded as preliminary as the number of strong storms considered is not sufficient for a statistical treatment (on the other hand, the occurrences of strong storms are infrequent).

Figure 13 shows the pitch angle distributions of muon intensity in time calculated by Eq. (3) for the storms listed in Table 1 [24: Rockenbach et al., 2011]. (The event on December 14, 2006 is also considered in [26: Fushishita et al., 2010] and described above.) A pitch angle 0^o corresponds to the sunward IMF direction. SSC occurrence is shown by a vertical line. Open and solid circles represent, respectively, an excess and deficit of CR intensity relative to the average, and the diameter of each circle is proportional to the magnitude of deficit or excess. Figure 14 shows the pitch angle distribution of the CR intensity on November 9, 2004 ten hours prior to the SSC at t = 314.583 indicated by arrow in the top panel of Fig. 13.

Table 1: Distribution of storms accompanied by LC precursors.

Types of storms by their intensity (number of storms)	Moderate Storms (89)	Intense Storms (37)	Super Storms (7)
Example of a storm	October 24, 2003	December 14, 2006	November 9, 2004
Advanced LC observations (by station)	5 hrs (Hobart)	8 hrs (São Martinho)	10 hrs (Hobart)

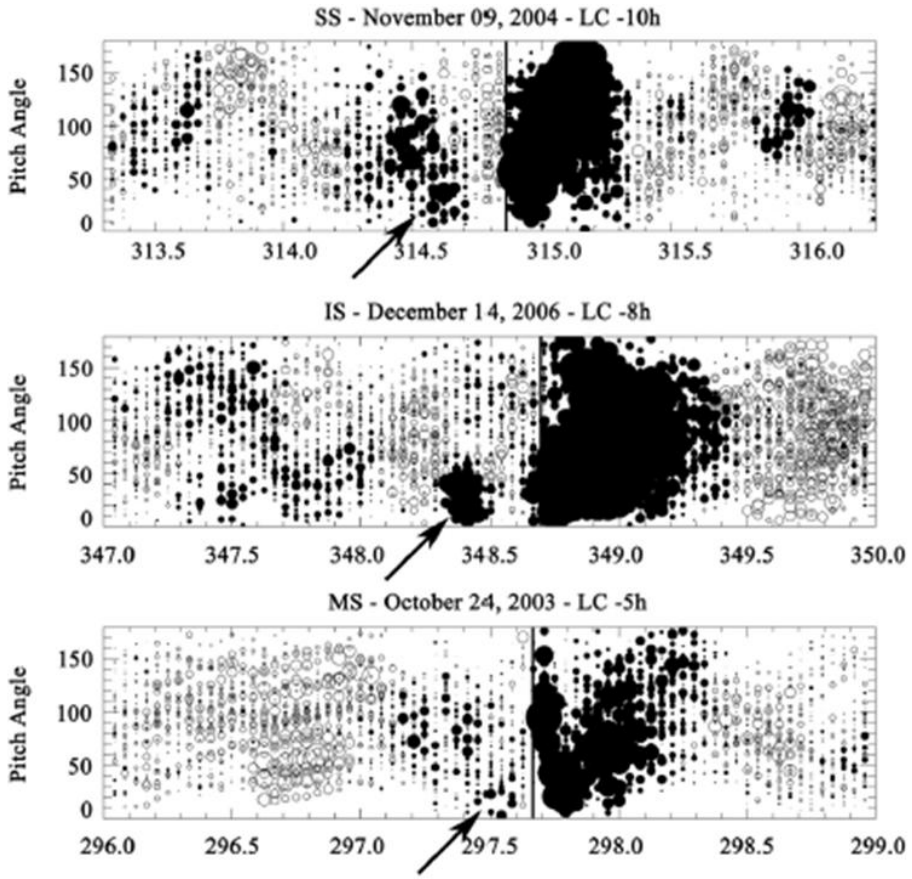

Figure 13: Pitch angle distributions of CR intensity for storms of different intensity before and after the SSC occurrence shown by vertical lines [24: Rockenbach et al., 2011].

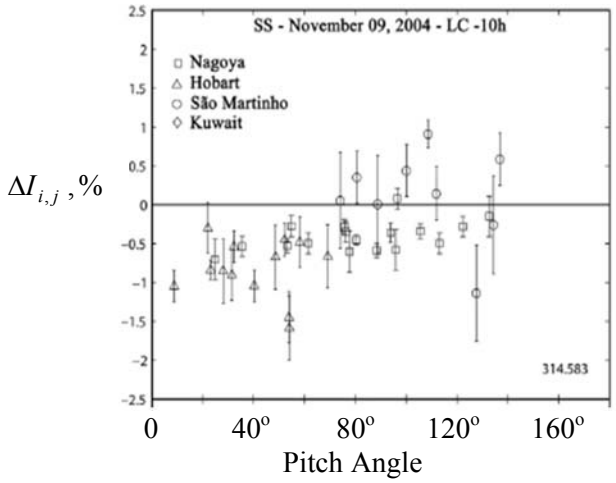

Figure 14: Cut of the top distribution in Fig. 13 at t = 314.583 indicated by arrow there [24: Rockenbach et al., 2011].

A similar analysis was applied to 22 storms observed with good coverage in [18: Munakata et al., 2000] where it was concluded that the lead time of observed precursors relative to the SSC is typically 8 hours and can be as much as 12 hours (see subsection 3.3). Moreover, the authors believe that LC precursors may often be observable in muon data earlier because the appearance time of LC precursors is often determined by the changing network coverage, i.e. the precursor seems to be already present when network viewing direction moves into the sunward IMF direction. In other words, with more stations for observations of precursors the lead time can be found to be larger than the values mentioned above.

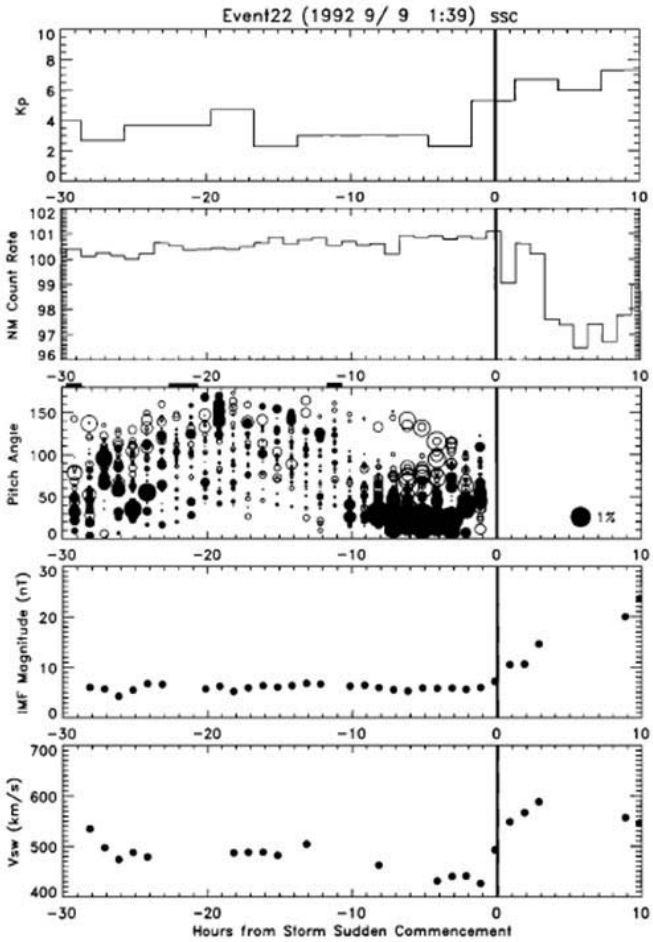

Figure 15: Observations for the period covering the geomagnetic storm on September 9, 1992 (from top to bottom): Kp index, McMurdo neutron monitor relative count rate, anisotropy derived from the muon telescopes, IMF magnitude and solar wind velocity [18: Munakata et al., 2000].

Figure 15 shows observations for the period covering SSC of the storm on September 9, 1992, one of the 22 storms mentioned above. The anisotropy measured by the muon telescopes appears as the third plot from the top. The open and solid circles represent an excess and a deficit of CR intensity relative to the average and the diameter of each circle is proportional to the magnitude of deficit or excess (see 1% scale to the right of the plot). There is evidence for a loss cone 25 hours prior the SSC [18: Munakata et al., 2000] but due to poor network coverage from -23 hours to -10

hours the statistical significance is not sufficient to be certain and the appearance time is conservatively stated as about 10 hours before the SSC [32: Jansen et al., 2001]. McMurdo neutron monitor observations (on the second plot from the top) show the long lasting nature of the event. A similar remark can be made about events occurred September 5, 1982, February 20, 1992, March 23, 1993 and September 24, 1998 [18: Munakata et al., 2000].

A correlation between LC-precursor depth and FD amplitude was discussed in [18: Munakata et al., 2000] and [33: Nonaka et al., 2005b]. Although the incidence of precursors increases with storm size, the correlations are far from perfect because the LC effect is determined not only by the FD amplitude but also other factors such as the upstream mean free path and the magnetic field angle at the shock. A trend found in [33: Nonaka et al., 2005b] on the basis of analysis of storm events observed with GRAPES-3 during period 2001-2002 confirms these considerations in Fig. 16 where two categories of data associated with the start of the FD are shown.

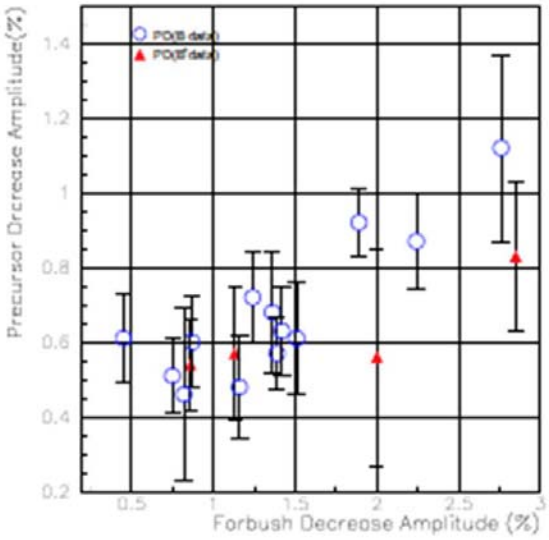

Figure 16: A trend between LC-precursor depth and FD amplitude [33: Nonaka et al., 2005b].

Anisotropy can be used to derive the CR density gradient associated with the drift of CR [34: Bieber & Evenson, 1998; 27: Okazaki et al., 2008]. The density gradient in turn is used to deduce ICME geometry and orientation [35: Kuwabara et al., 2009], which is important to predict the effect of ICME on Earth's magnetosphere. One of the difficulties of such an approach is that the commonly used diffusive approximation becomes invalid at some limiting rigidity while the transition between diffusive and non-diffusive behaviours is not yet well understood [27: Okazaki et al., 2008]. Thus, theoretical modelling of CR response to propagation of the ICME is required in order to understand the limitations.

4 Theoretical modelling of CR variations during space weather event

For further study and better understanding of LC precursor, different physical models are currently being developed. For example, in [20: Ruffolo et al., 1999] and [36: Petukhov & Petukhov, 2009] some models were built to describe the dynamics of CR intensity. Below we consider a general example of the model for CR transport in space.

4.1 Model of CME-driven storm

When interplanetary CME is travelling in space with a speed higher than the local magnetosonic wave speed, it generates a shock ahead of it [37: Hudson et al. 2006; 38: Shen et al., 2007]. The shock is followed by a turbulent sheath (Fig. 17) with large fluctuations in both the strength and the direction of the magnetic field [39: Burlaga et al., 1981].

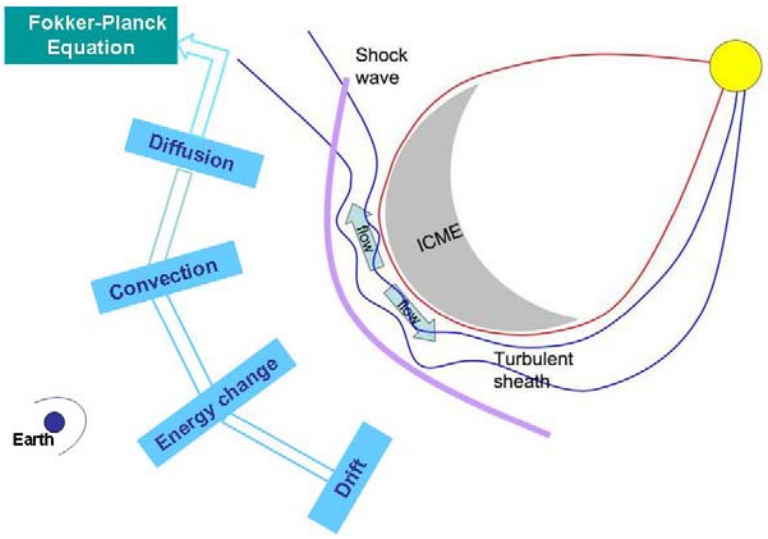

Figure 17: A structure of a solar disturbance.

Following Parker's theory [40: Parker, 1965] the fundamental equation for the transport of CRs in the heliosphere is a Fokker-Planck diffusion equation with the terms corresponding to the four physical processes shown in Fig. 17. As a result, an equation for the particle concentration can be written as [41: Dorman & Katz, 1977]

$$\frac{\partial N}{\partial t} = \underbrace{\nabla(\kappa \nabla N)}_{\text{Diffusion}} - \underbrace{\vec{V}_{SW} \cdot \nabla N}_{\text{Convection}} - \underbrace{\vec{V}_d \cdot \nabla N}_{\text{Drift}} + \underbrace{\frac{p}{3}\frac{\partial N}{\partial p}\text{div}\vec{V}_{SW}}_{\text{Energy change}} ,$$

where t is time, V_{SW} is the solar wind speed, V_d is the drift velocity, and p is the momentum of a CR particle. The drift velocity of a particle with charge q, momentum p, and speed v in magnetic field $\vec{B}$ can be written as [42: Jokipii, Levy & Hubbard, 1977]

$$\vec{V}_d = \frac{p\mathrm{v}}{3q}\nabla\times\left(\frac{\vec{B}}{B^2}\right).$$

Thus, to solve the transport equation for simulation of CR particles concentration, one needs to know diffusion tensor κ . All other values can be found from measurements on satellites.

Below we consider an isotropic diffusion model, where κ is a scalar, and verify the validity of the model on the basis of analysis of data from Nagoya muon telescope, McMurdo station and Advanced Composition Explorer (ACE) described in subsection 4.2.

4.2 Sources of data

4.2.1 Nagoya muon telescope

The Nagoya telescope is geographically located at 35°09’ N and 136°58’ E at 77 m above the sea level. It has cutoff rigidity of 11.5 GV and the median rigidity of 60 GV for the vertical directional channel. The average count rate being $2.76\cdot10^6$ particles per hour [43: Fujii, 2011]. High counting rate of the telescope naturally reduces the statistical fluctuations due to the finite counting rates. Then the change of counting rate due to other reasons such as the change of the pulse height distribution has a much more important effect on the stability of the observed rate. Instrumental fluctuations in short time interval (less than a day), mainly originate from changes of the room temperature. In order to reduce this cause, the room temperature of the observation room is air-conditioned to 20±1°C and the temperature variation in the thermostatic chamber containing the telescope is maintained within ±0.1°C throughout the year. By this regulation of the temperature change, the observed intensity has an overall stability of ±0.01% for duration of a few days. The stability in longer time interval is mainly controlled by the variation in the pulse height distribution due to the fatigue of the phototube as well as the change of the scintillation efficiency. As no compensation for these effects were made, a decrease of less than 1% per year in the counting rate was observed.

4.2.2 McMurdo neutron station

To confirm FD effects registered by the muon telescope in Nagoya, pressure corrected data from McMurdo neutron station were used. McMurdo neutron station is geographically located in Antarctica (77°51' S, 166°40' E) with altitude of 48 m above the sea level and distance of 1,360 km (850 miles) north of the South Pole. The cutoff rigidity of the station is 0.3 GV. An accuracy of measurements with the neutron monitor at the station is not available. The large space weather events mostly have FD in both muon and neutron data.

4.2.3 Advanced Composition Explorer

Solar wind parameters and IMF data used in the study are taken from the observations with the Advanced Composition Explorer (ACE) managed by NASA. The ACE orbits the Sun at about 1.5 million km from Earth and 148.5 million km from the Sun (the L1 libration point). The study used 4-min data for solar wind parameters and the 16-second data for the IMF in the Geocentric Solar Magnetospheric System (GSM)

4.3 Identification of large events

The variability of the relative count rate of cosmic-ray produced muons registered in the vertical view direction for 14-year period since 1998 up to early 2012 [44: Kalugin, 2012], shown in Fig. 18 demonstrates long-term (seasonal) variations and the spiking drops (numbered), which are the large events.

The seasonal (periodic) variations have the local minimums during summer seasons and the local maximums during winter seasons. This observation, along with Fig. 19, where is shown a part of the sunspot cycle for the same period (data are taken from [45: NASA]), tells us that the solar activity and CR intensity are in opposite phase. This is due to the fact that a more active solar wind and stronger magnetic field during a higher solar activity reduces the flux of cosmic rays striking the Earth's atmosphere. At the same time, it can be noted that the large events were absent during low part of the solar cycle (2006-2012).

The FD effect can be characterized by amplitude A_{FD} shown in Fig. 20. Since A_{FD} can be measured in different ways, an uncertainty Δ is introduced and shown in the same figures. In case when an event has a many-step decrease, only the first step is taken into account. In Fig. 18, there are numbered the first seven largest Forbush decreases. Figure 21 shows a distribution of the FD amplitude exceeding 1.5% as large FD events are of most interest. One can see that small amplitude events occur most frequently and large amplitude events occur seldom. This is reason why the extreme space weather events are difficult to be studied statistically.

Table 2 lists the largest FD events selected by visual inspection of the intensity plotted in Fig. 18 [46: Kalugin et al., 2012]. Two criteria were applied: (a) event should not be a part of a chain of events unless it is the first one in it; (b) event also should be observed at the McMurdo neutron station. The table includes events with FD magnitude $A_{FD} > 2.5\%$, the rest of data are given for illustrative purposes. In the table, $(v_1 + v_2) / 2$ is an average of the solar wind speed values immediately in front of and behind the shock respectively, registered at ACE at time moments t_1 and t_2; t_{start} is the moment when FD starts. The events are listed by ascending A_{FD}.

By the ratio Δ / A_{FD} the events listed in Table 2 are conditionally broken into three groups: events with the ratio less than 7% (small uncertainty), between 7% and 22% (medium uncertainty) and larger than 22% (large uncertainty). In figures 22 and 23 we represent each event by its value of A_{FD} (Δ is shown as an error bar) and average v of values v_1 and v_2 from Table 2; dashed lines relate to multiple events in the decrease phase to show a total decrease (also shown in brackets in Table 2). The average speed $v = v_1 + (v_2 - v_1)/2$ is chosen as it depends both on background for a shock (v_1) and a jump at the front (v_2-v_1).

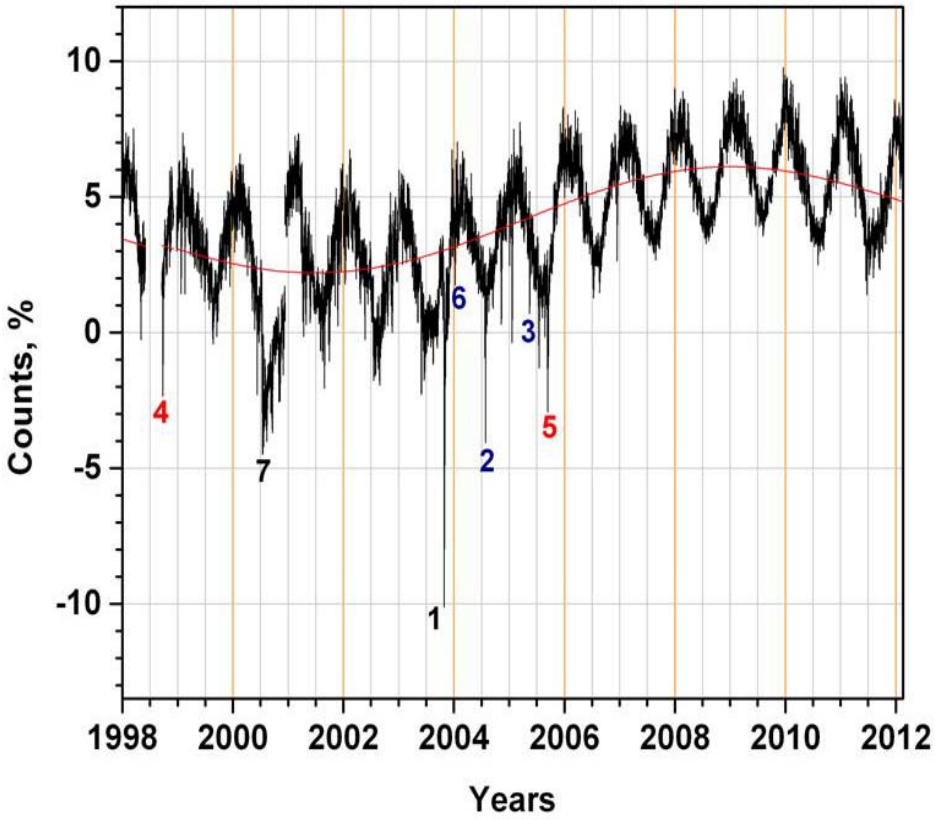

Figure 18: Muon counts by Nagoya telescope.

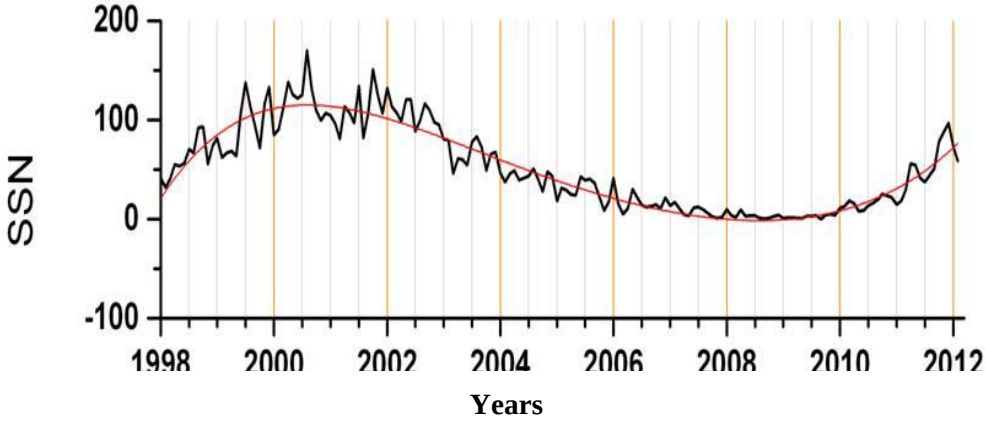

Figure 19: Solar activity in terms of sunspot numbers.

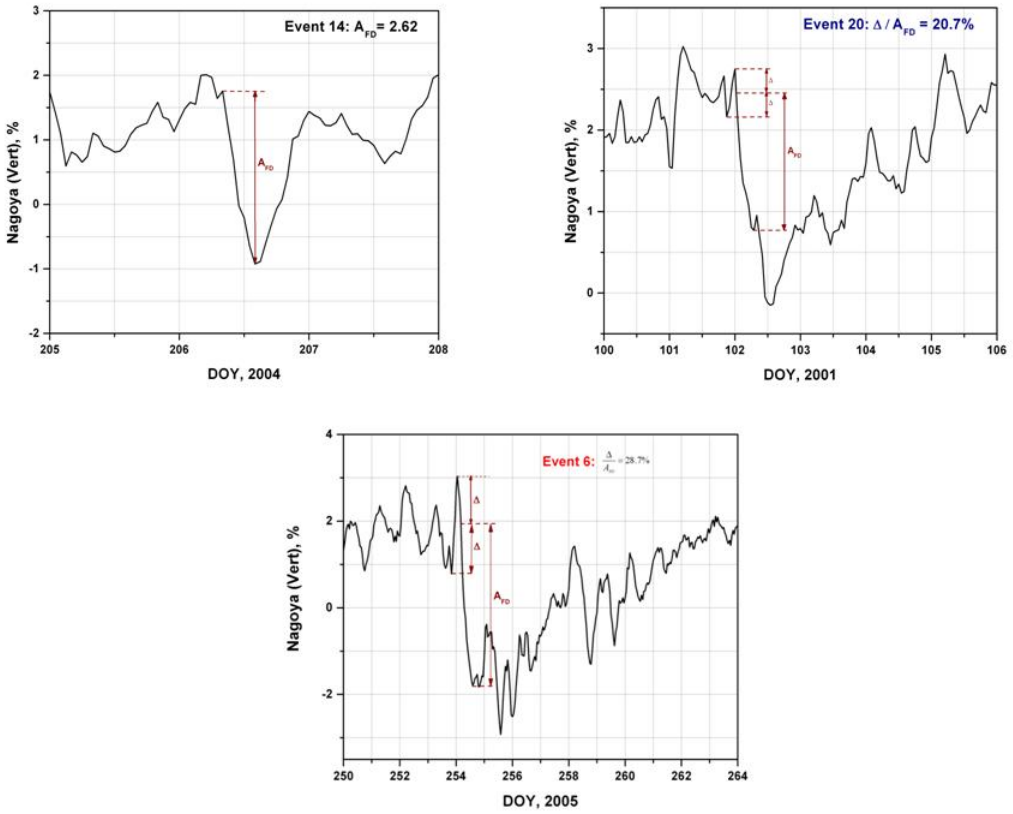

Figure 20: Measurements of FD amplitude.

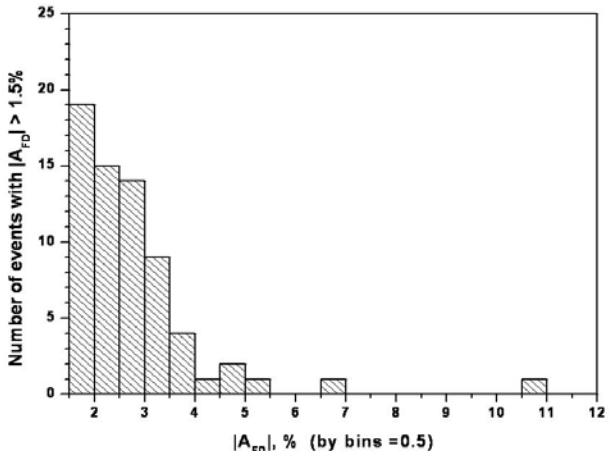

Figure 21: Distribution of the FD amplitude.

Table 2: List of the largest FD events.

No.	Year Day (DOY)	t_1	t_2	$(v_1+v_2)/2$, km/s	t_{start}	A_{FD}, %	Δ/A_{FD}, %
1	2003 Oct 29 (302)	1:00 (302)	7:05 (302)	1263	6:29 (302)	11.02	7.0
2	2004 Jul 26 (208)	22:24 (208)	22:28 (208)	764	0:53 (209)	6.01	10.7
3	2005 May 15 (135)	2:10 (135)	3:49 (135)	643	3:29 (135)	4.09	10.3
4	1998 Sep 24 (267)	23:13 (267)	23:19 (267)	526.5	3:27 (268)	3.85	22.3
5	2005 Sep 10 (253)	15:59 (253)	0:59 (254)	879	3:02 (254)	3.76 (6.97)	28.7
6	2004 Jan 22 (22)	1:03 (22)	1: 07 (22)	566	4:03 (22)	3.30	19.1
7	2000 Jul 13 (195)	9:00 (195)	9:37 (195)	600.5	9:00 (195)	3.22	0
8	2005 Jan 21 (21)	16:42 (21)	16:54 (21)	756.5	18:14 (21)	3.03	8.9
9	2000 Jun 8 (160)	8:39 (160)	8:43 (160)	631.5	8:39 (160)	2.98	0
10	1999 Jan 22 (22)	19:45 (22)	19:49 (22)	575.5	5:02 (23)	2.95	6.4
11	2001 Nov 5 (309)	21:52 (309)	1:52 (310)	573	5:39 (310)	2.68	5.6
12	2001 Mar 27 (86)	1:16 (86)	1:18 (86)	468.5	6:33 (86)	2.67	19.8
13	2001 Sep 25 (268)	18:20 (268)	21:20 (268)	530	20:20 (268)	2.64	6.1
14	2004 Jul 24 (206)	5:36 (206)	5:39 (206)	535.5	7:60 (206)	2.62	1.9
15	2001 Aug 17 (229)	10:15 (229)	10:18 (229)	413.49	10:48 (229)	2.54	33.1
16	2001 Sep 29 (272)	9: 03 (272)	9: 09 (272)	595	19:12 (272)	2.52	20.6
17	2011 Jun 17 (168)	1:59 (168)	2:04 (168)	515	4:01 (168)	2.07	21.7
18	1998 Nov 8 (312)	4:18 (312)	4:23 (312)	546.5	6:14 (312)	1.90	53.7
19	2001 Apr 11 (101)	13:07 (101)	13:15 (101)	553	0:30 (102)	1.64	20.7
20	2001 Apr 28 (118)	4:29 (118)	4:32 (118)	622.5	8:20 (118)	1.38 (3.3)	50.7
21	2006 Dec 14 (348)	13:52 (348)	14:02 (348)	763.5	14:02 (348)	1.30 (2.36)	0
22	2000 Sep 17 (261)	16:55 (261)	16:59 (261)	663	17:02 (261)	0.73 (1.92)	0
23	2001 Apr 4 (94)	14:20 (94)	14:27 (94)	554.5	14:31 (94)	0.70 (2.1)	0

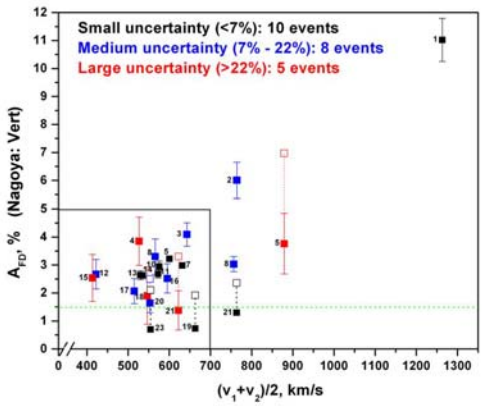

Figure 22: Events listed in Table 2.

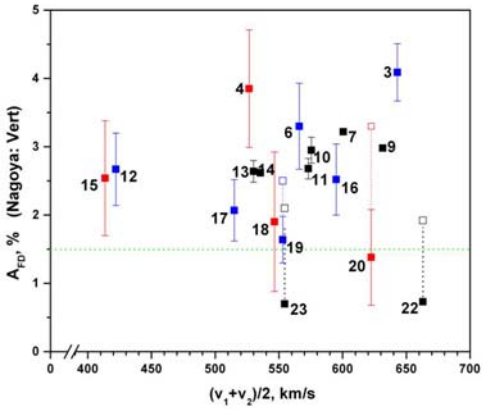

Figure 23: Zoomed-in fragment in Fig. 22.

The figures show that grouping events by some criteria together with a simple propagation model including the solar wind parameters and IMF looks reasonable to continue the analysis of FD events [46: Kalugin et al., 2012].

4.4 Solar wind parameters

The ACE data are combined with Nagoya telescope data and McMurdo neutron station. As an example, data to be analyzed for events No. 3, 10 and 11 listed in Table 2 are presented below. Specifically, the data for event No.3 are presented in Fig. 24 where are shown from the top down neutron and muon count rates, solar wind (proton) speed, temperature and density. Figure 25 shows for the same event the magnitude $|\vec{B}|$ of IMF together with its components and ratio of the variance of $|\vec{B}|$ to $|\vec{B}|$. Small (large) values of this ratio indicate little (significant) variation of the magnitude of IMF.

Similar distributions are presented in figures 26-29 for events No. 10 and 11. A part of curve in Fig. 28 depicted with red color is related to the speed of alpha particles and used here to restore missed values of the solar wind speed during event No.11 (see also subsection 4.5). In all the figures, one can see that a sharp decrease in neutron and muon count rates corresponds to rapid changes in the solar wind parameters and IMF. Therefore it is natural to build a model of FD events based on data on the solar wind and IMF. However, the CR particles, which produce muons in the Earth's atmosphere, travel in the IP space with a speed close to the speed of light *c.* Since the solar wind speed is much less than *c,* the particles can be more affected by the IMF rather than the solar wind itself. Thus, it makes sense to focus on changes in IMF. In addition, many theoretical models for CR propagation involve the power spectrum of the IMF. Therefore, in the analysis of events, a spectrogram for the IMF is incorporated. In subsections 4.7 and 4.8 we consider an application of IMF spectrogram to a diffusion model for CR transport described in subsection 4.6.

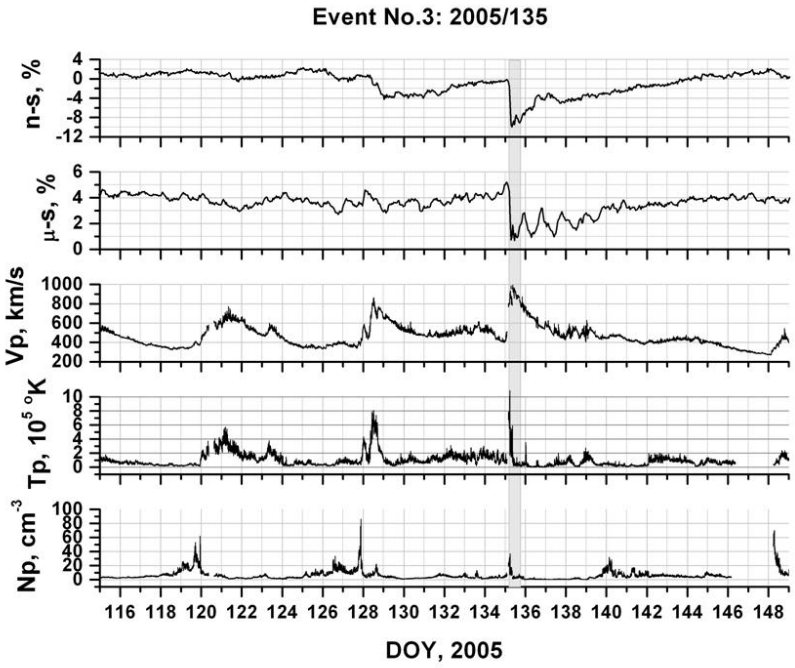

Figure 24: Muon and neutron count rates together with solar wind parameters during event No.3.

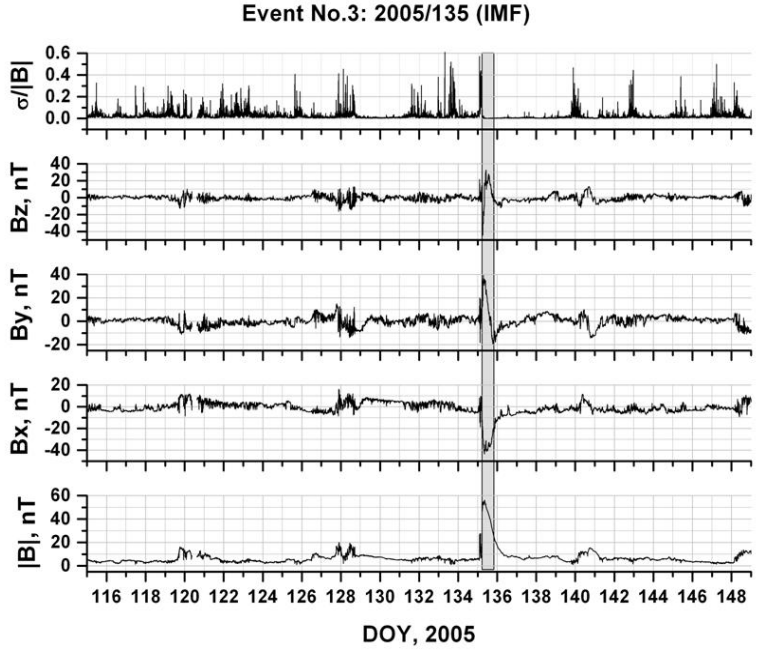

Figure 25: IMF during event No.3.

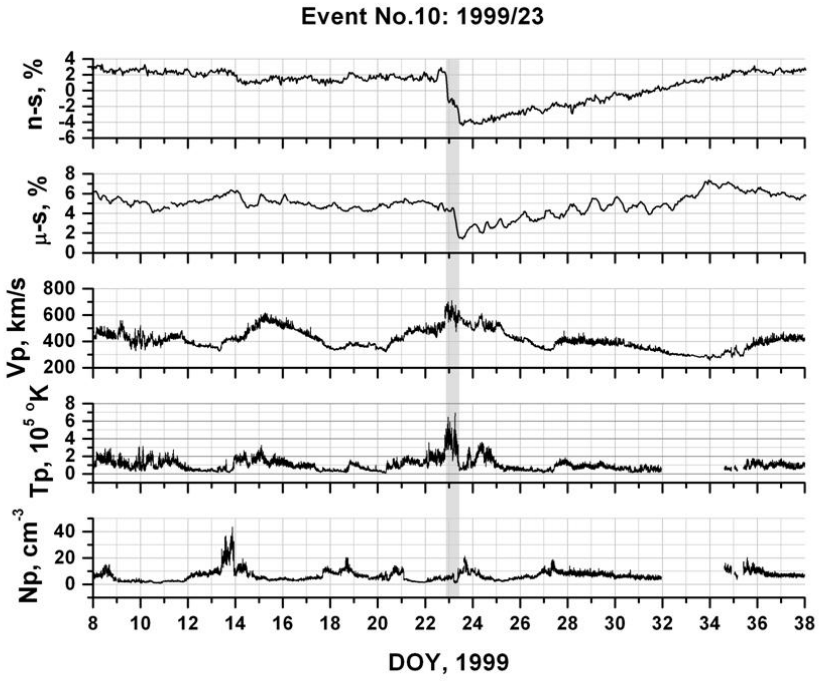

Figure 26: Muon and neutron count rates together with solar wind parameters during event No.10.

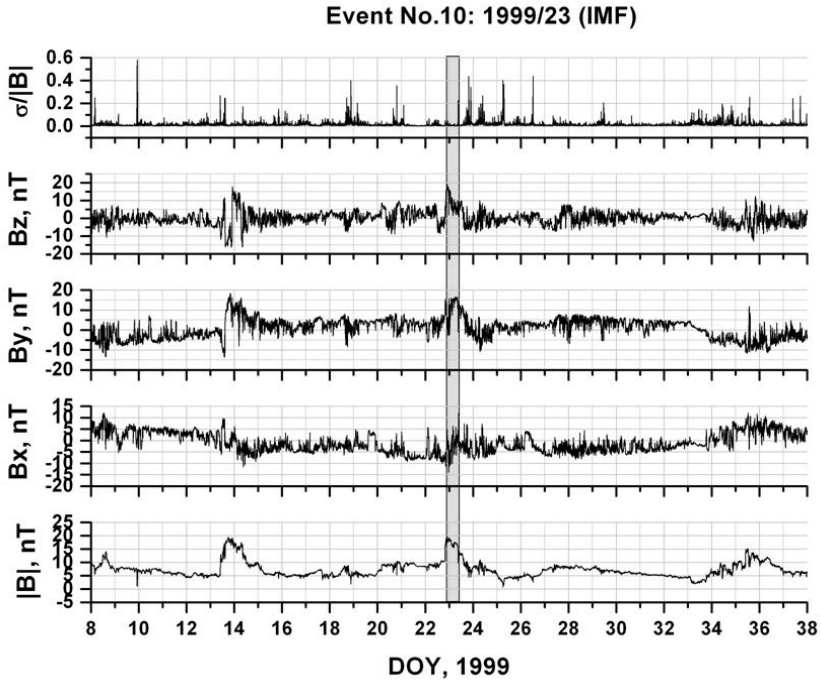

Figure 27: IMF during event No.10.

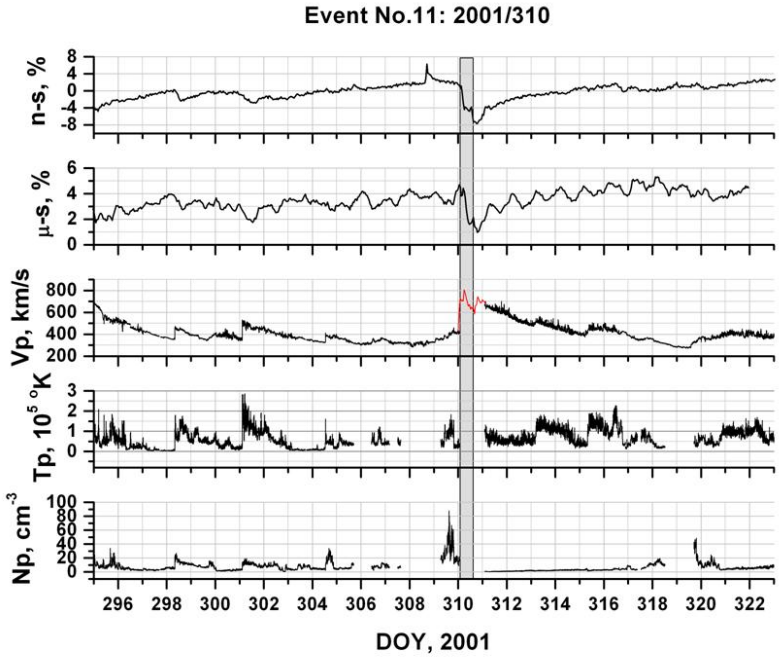

Figure 28: Muon and neutron count rates together with solar wind parameters during event No.11.

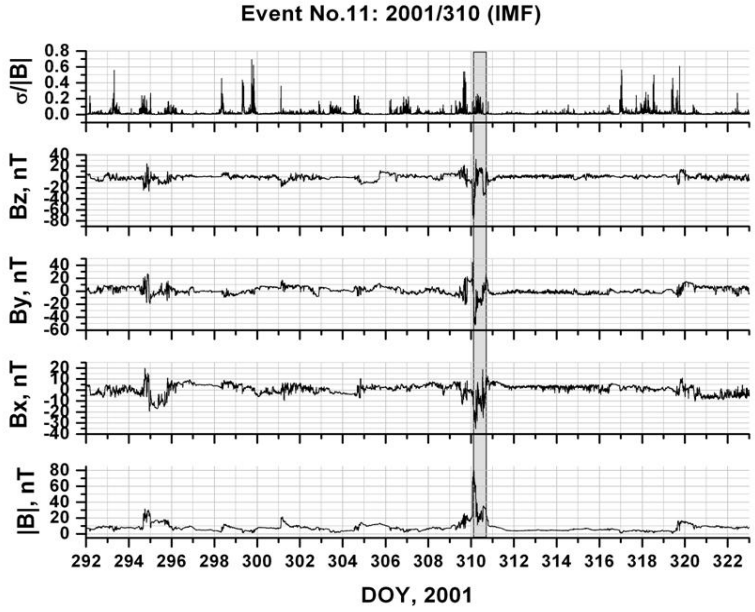

Figure 29: IMF during event No.11.

4.5 Filling gaps in ACE data

During some extreme space weather events ACE data can be missed (see plot for the solar wind speed in Fig. 28). However, these data are important to identify some characteristics of an event, for example, the shock arrival at Earth.

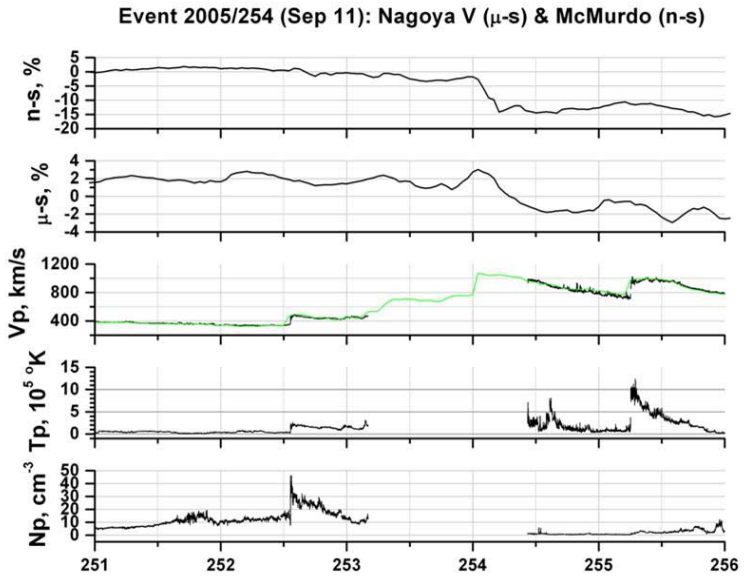

Figure 30: Filling the solar wind speed during event No.5.

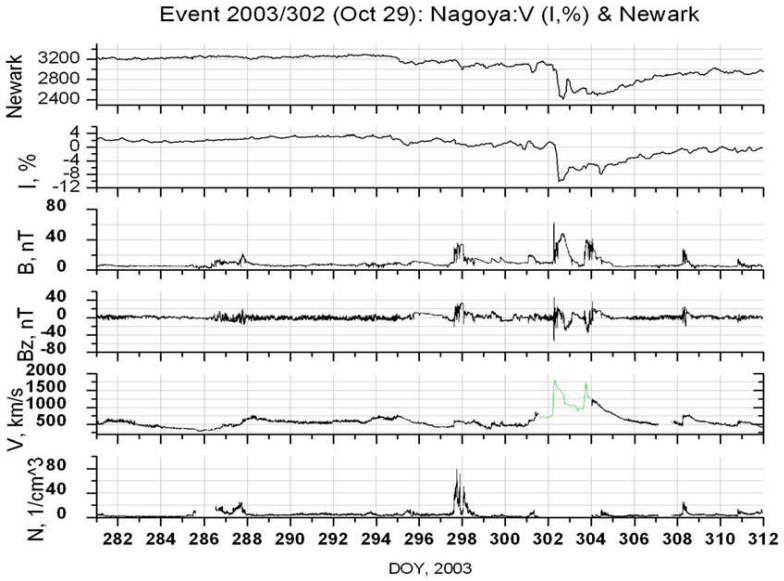

Figure 31: Filling the solar wind speed during event No.1.

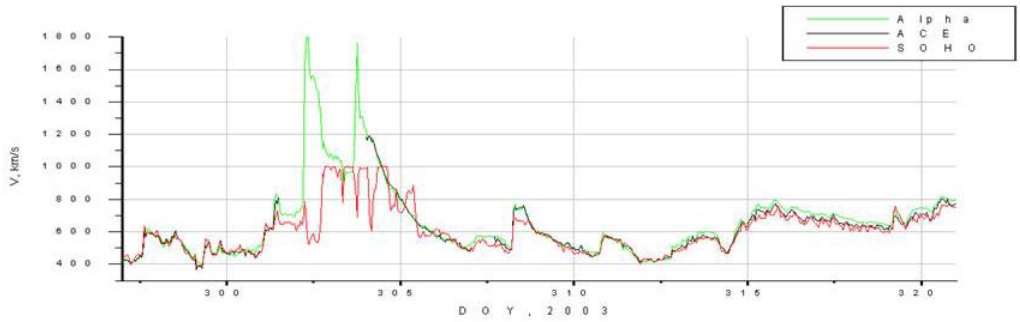

Figure 32: Comparison between different data for the solar wind speed during event No.1.

We found that to restore the solar wind speed data one can use values for the speed of alpha particles measured by ACE at the same time as the solar wind parameters [47: Kalugin & Trichtchenko, 2012]. Examples are shown in figures 30 and 31 for events No. 5 and 1 respectively where the restored parts are depicted with green color. In addition, Figure 32 shows SOHO data for event No. 1 to see that it is a less appropriate candidate to restore the solar wind speed taken from ACE.

4.6 Diffusion model

A charge particle in a magnetic field travels with a helical motion around a "guiding" magnetic field line. Due to fluctuations of the magnetic field charged particles can "jump" from one guiding line to another. Thus, it is mainly the fluctuating part of the field that causes the scattering that leads to diffusion of particles [48: Jokipii & Coleman, 1968]. In other words, a diffusion of particles is determined by the distribution of magnetic field fluctuations $\vec{B}'$ and it is convenient to represent the magnetic field as $\vec{B} = <\vec{B}> + \vec{B}'$, where $<\vec{B}>$ is an averaged magnetic field. The fluctuations can be characterized by their power spectrum and in order to use it in computations of the diffusion coefficient we assume that the magnetic field inhomogeneities are statistically isotropic [49: Jokipii, 1967].

In their motion in a disturbed magnetic field charged particles encounter transverse waves propagating perpendicular to the mean magnetic field. A perturbing force changes the parallel component of velocity and hence the pitch angle, i.e. the angle between the particle's velocity vector and the local magnetic field. The charged particles scatter mainly at the field fluctuations which allow the particle gyration to match the spatial wavelength [50: Quenby et al., 2013]. Therefore the resonant frequency is given by $f_{res} = kV_{SW} / 2\pi$, where V_{SW} is the solar wind speed and $k = \omega_B / \mathrm{v}$ for gyrofrequency ω_B and particle velocity v along the field [50: Quenby et al., 2013].

Here we consider particles at high energies when a ratio of the two-point correlation length λ_c in the random magnetic field is much less than gyroradius r_g of particle in the mean magnetic field [51: Klimas & Sandri, 1971],, i.e. when

$$\chi = \frac{\lambda_c}{r_g} << 1 . \qquad (4)$$

The correlation length λ_c shows a distance over which the random magnetic field still "remembers" its neighbour value, the gyroradius is the radius of the circular component of motion of a charged particle in the magnetic field. The above described effects of waves are more important for particles with intermediate and low energies. However, to understand a connection between the diffusion coefficient and a model for the power spectrum of fluctuations used below one should have a whole picture not only the high-energy limit [52: Klimas & Sandri, 1973]. Besides, one needs to set limits of applicability of the diffusion model under consideration.

To apply a diffusion model developed in [51: Klimas & Sandri, 1971] and [53: Fisk et al., 1974], in addition to the condition (4) we assume that

$$\varepsilon = \frac{\alpha}{(\chi\eta)^2} << 1 , \tag{5}$$

where $\alpha = \sqrt{\pi}\lambda_c /(6L_s)$, L_s = 1a.u. is a size of the system containing the particles and $\eta = \sqrt{< \vec{B}' \cdot \vec{B}' >} \big/ |< \vec{B} >|$. Then, in the high-energy limit, the diffusion coefficient is a scalar given by [51: Klimas & Sandri, 1971]

$$\kappa = \frac{1}{3}\frac{\mathrm{v} r_g^2}{\lambda_c \eta^2} \ . \tag{6}$$

Since the magnetic rigidity R of a charged particle in the mean field is $R = |< \vec{B} >| r_g$, the formula (6) is in agreement with the rigidity dependence $\kappa \sim (\mathrm{v}/c)\cdot R^2$ given in [54: Jokipii, 1971; 55: Volk, 1975] for particles with R > 10 GV. However, in [56: Kachelrieß, 2007] it is given a different expression for the diffusion coefficient which is connected with (6) as $\kappa \cdot \lambda_c / r_g$. Under condition (4) this is a significantly reduced estimation of the diffusion coefficient compared to formula (6).

It is also interesting to compare the expression (6) with the diffusion coefficient in a turbulent magnetic field which, under the assumption that it is statistically isotropic, is given by [57: Urch, 1977] (after correcting misprinting)

$$\kappa' = \frac{1}{6}\frac{\mathrm{v}^2}{\int_0^\infty G(\mathrm{v}\tau) d\tau} \ ,$$

where $G(r)$ is the isotropic part of the auto-correlation function of the magnetic field. Following [57: Urch, 1977] the integral can be estimated as

$$\int_0^\infty G(\mathrm{v}\tau) d\tau \cong \int_0^{\lambda_c/\mathrm{v}} G(0) d\tau = \omega_{B'}^2 \frac{\lambda_c}{\mathrm{v}} \ ,$$

where $\omega_{B'}$ is a gyrofrequency associated with the stochastic field. If we introduce a gyroradius $r'_g = \mathrm{v}/\omega_{B'}$ in the stochastic field, we obtain

$$\kappa' = \frac{1}{6}\frac{\mathrm{v}\, r'^2_g}{\lambda_c} \ .$$

Then the ratio of the diffusion coefficients can be written as

$$\frac{\kappa'}{\kappa} = \frac{1}{2}\left(\frac{R'}{R}\right)^2 ,$$

where R' is the rigidity in the stochastic field. Thus particles with a larger rigidity in the mean field potentially are less subject to diffusion in the stochastic field.

To find λ_c we consider the one-dimensional power spectrum for the transverse fluctuations perpendicular to the mean field direction in the form [53: Fisk et al., 1974]

$$P_\perp(f) = P_\perp(0)\ \frac{1 + 2\nu\ \dfrac{(f/f_c)^2}{1+(f/f_c)^2}}{\left[1+(f/f_c)^2\right]^\nu} \ , \qquad (7)$$

where $f_c = V_{SW}/2\pi\lambda_c$. Note that for high-energy particles $f_{res} << f_c$ which is equivalent to Eq. (4) and verified in subsection 4.8.

4.7 Power spectrum estimation

To estimate power spectrum it was used a spectrogram for the transverse component of IMF fluctuations computed for 4-min averages of the ACE IMF data (level 2).

To compute the transverse component of IMF fluctuations we rotate the original coordinate system *xyz* (blue color in Fig. 33) about the axis passing through the origin and perpendicular to the plane of vector <***B***> and *z*-axis (the plane of the figure) on such angle that the vector <***B***> lies in a new (*x,y*)-plane (green color). Then in the new coordinate system $<B_z>=0$ and $\left(0, 0, \hat{B}'_z\right) \perp < \hat{B} >$.

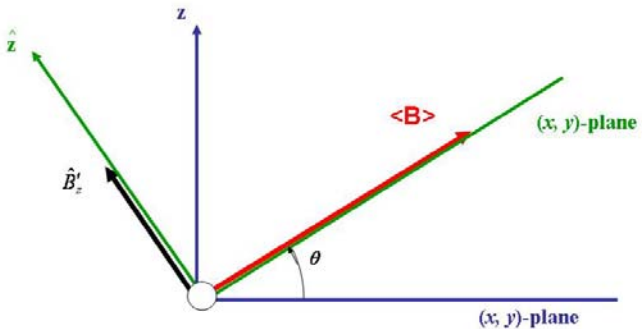

Figure 33: Computation of transverse IMF fluctuations.

The spectrograms were built as a time-frequency representation for a 12-day period embracing an event under study using the discrete short-time Fourier transform normalized by the peak signal gain of a window [58: Harris, 1999]

$$P(n,k)=\left|\frac{\sum_{m=0}^{L-1} b(m)w(n-m)e^{-i2\pi mk/L}}{\sum_{m=0}^{L-1} w(m)}\right|^2,$$

where $b(m)=\hat{B}'_z(t_m)$ is the value of the transverse component of the magnetic field at time $t = t_m$ and $w(n)$ is the Gaussian window of length L defined as [59: Haykin & Liu, 2009; 60: Stergiopoulos, 2009]

$$w(n)=\exp\left[-\frac{1}{2}\left(\frac{n-L/2}{\sigma L/2}\right)^2\right]$$

with $\sigma \le 0.5$. The Gaussian window was chosen as it has optimal resolution [61: Boashash, 2003; 62: Hale, 2006]. Particularly, the Gaussian window provides a joint time and frequency resolution superior to all other window functions such as Hanning, Hamming, Kaiser, Bartlett, and so on [63: Allen & Mills, 2004]. The parameter σ controls the width of Gaussian window so that a larger value of σ leads to a narrower main-lobe and higher side-lobes [58: Harris, 1999]. To get the maximum frequency resolution, in computations it was chosen the maximum value $\sigma = 0.5$. The length of the window L=256 was chosen because the value $1/(256\cdot 4\,\text{min}) = 1.63\cdot 10^{-5}$ Hz corresponds to the values of then found characteristic frequency (see values for f_c in Table 3 below). Besides, this value of L is the maximum among integer powers of two when a dependence of power spectrum on time has not been changed significantly in increasing L. A similar analysis with different values of L is given in [64: Ikelle & Amundsen, 2005].

4.8 Results

The approach used for power spectrum estimation was reported in [65: Kalugin & Trichtchenko, 2013]. Here we demonstrate it by taking into consideration events No. 3, 10 and 11 considered in section 4.5. The spectrograms for these events are shown in figures 34-36. In all the figures, the top panel shows a profile $P(f)$ obtained as a horizontal cut of spectrogram at the moment when the power spectrum has the absolute maximum. Fitting the profile by function (7) gives estimation of f_c. The vertical cuts of spectrograms are shown at frequencies close to the found f_c.

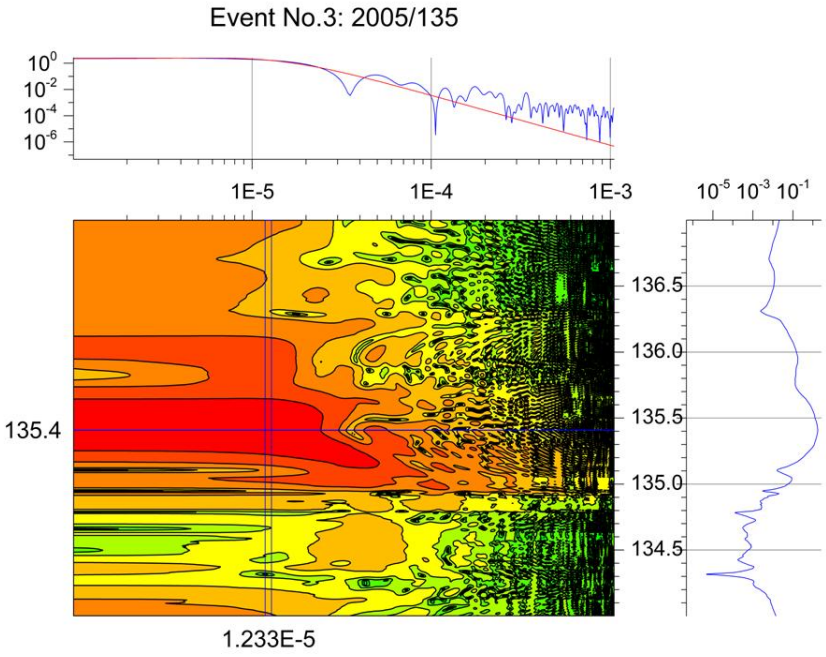

Figure 34: Spectrogram for transverse IMF during event No.3.

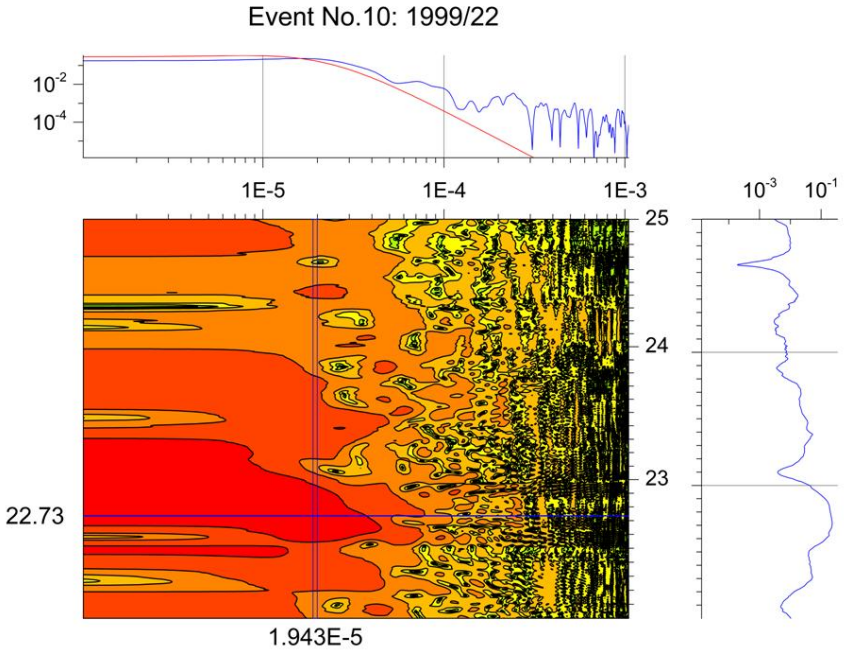

Figure 35: Spectrogram for transverse IMF during event No.10.

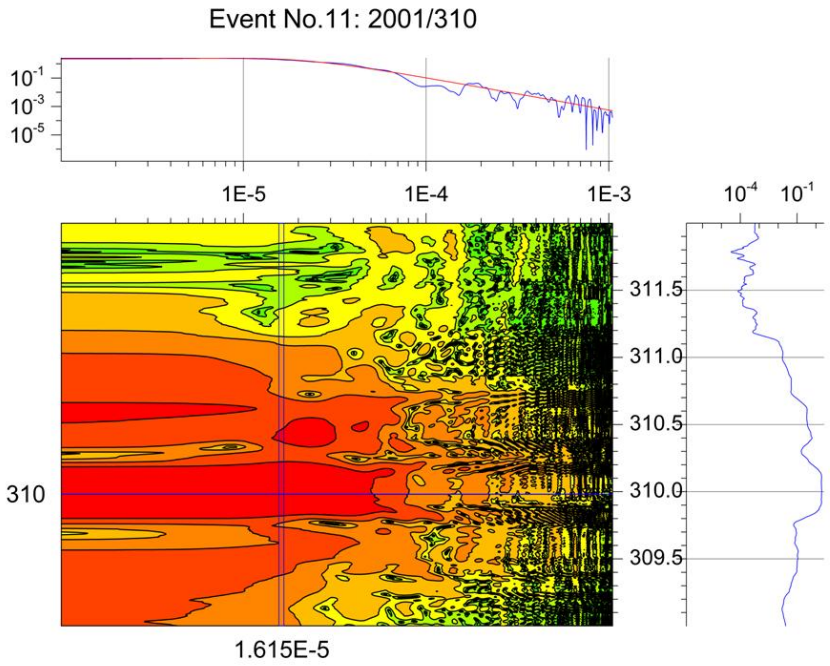

Figure 36: Spectrogram for transverse IMF during event No.11.

Using ACE data we fill up the first four columns of Table 3 where gyroradius is computed for 60-GV protons (which is the median rigidity for Nagoya muon telescope, see subsection 4.2.1). After retrieving values of f_c from the spectrograms shown above we are able to fill the last three

columns by computing the values of the dimensionless parameters χ and ε introduced in (4) and (5). Table 3 gives typical values of parameters χ and ε for events No. 3, 10 and 11 together with other parameters. It follows that one can regard the conditions (4) and (5) to be satisfied and therefore the diffusion approximation in high-energy limit is valid and the model is acceptable.

Table 3: Analysis of diffusion model.

Event No.	$\lvert\langle \mathbf{V_{SW}} \rangle\rvert$, km/s	$\lvert\langle \mathbf{B} \rangle\rvert$, nT	η	r_g, a.u.	f_c, μ Hz	λ_c, a.u.	χ	ε
3	519.79	2.93	6.83	0.45	12.4	0.044	0.098	0.029
10	409.43	4.74	5.58	0.28	19.5	0.022	0.079	0.033
11	411.75	1.98	8.14	0.67	16.0	0.027	0.040	0.075

The results of the analysis of the diffusion process performed in the report allow us to come to the next step in modeling CR modulation, i.e. to solve the CR transport equation for the particle concentration $N(t,\vec{r},p)$, shown below following [66: Langner & Potgieter, 2005]

$$\frac{\partial N}{\partial t} + \left(\vec{V}_{SW} + \vec{V}_d\right)\cdot \nabla N = \nabla(\kappa \nabla N) + \frac{p}{3}\frac{\partial N}{\partial p}\mathrm{div}\vec{V}_{SW} ,$$

where t is time, $\vec{r}$ is radius-vector, p is the momentum of particle, V_{SW} is the solar wind speed, V_d is the drift velocity expressed in terms of particle velocity v, charge q and magnetic field $\vec{B}$ as

$$\vec{V}_d = \frac{p\mathrm{v}}{3q}\nabla \times \left(\frac{\vec{B}}{B^2}\right) .$$

Here $q = e$, $\mathrm{v} \approx c$, $p = \sqrt{E^2 - m_p^2 c^4}\,/\,c \approx E/c$, where c is the speed of light, m_p is the mass of proton and E is the total energy of particle. The quantities V_{SW} and $\vec{B}$ are taken from ACE data. The coefficient of diffusion is

$$\kappa = \frac{1}{3}\frac{\mathrm{v}\, r_g^2}{\lambda_c \eta^2} ,$$

where $\eta = \sqrt{\langle \vec{B}' \cdot \vec{B}' \rangle}\,\big/\,|\langle \vec{B} \rangle|$, $\vec{B} = \langle \vec{B} \rangle + \vec{B}'$, $r_g = p/(|q|\,|\langle \vec{B} \rangle|)$, λ_c is the correlation length of B'. The boundary conditions for solving the transport equation are chosen depending on a particular geometry and computational domain.

Thus methods for analysis of muon and ACE data combined with theoretical and numerical models allow us to study effects of solar disturbances on cosmic ray intensity. A similar approach can be applied to the neutron component but with a different expression for the diffusion coefficient.

5 Overview of curent situation in muon detection for space weather applications

To be sensitive to the type of particle that acts as a precursor to magnetic storms, the detector should be able to provide some energy discrimination and directional information. The hypothesis is that the precursor particles will display differences in the momentum spectrum or differences in the direction of arrival compared to the regular CR.

5.1 Viewing directions of muon detectors

The CR particles approaching the Earth encounter the geomagnetic field and are deflected by it so that the highest energy particles experience the least deflection. Therefore, if the particles are sufficiently energetic (such as cosmic ray particles), they propagate inside the magnetosphere and enter the Earth's atmosphere producing neutrons and muons. In principle it should be possible to trace the path of such a particle until it reaches the ground as long as we have a sufficiently accurate mathematical description of the field. Such an approach would require particles from all space directions to be traced to the ground to determine the response. It is more practical to trace particles with the same rigidity (which is momentum per unit charge) from the location of the detector station through the field to free space because they will follow the same path as particles arriving from the space [12: Duldig, 2001]. When calculated in this way it is found that for a given rigidity there may be some trajectories that remain forever within the geomagnetic field or intersect the Earth's surface. These trajectories are termed "forbidden" as they indicate that the site is not accessible from space for that rigidity and arrival direction at the station. The particle trajectories that escape to free space are called "allowed" and associated with the accessible directions which are known as asymptotic directions of approach [67: McCracken et al., 1962; 68: McCracken et al., 1968; 69: Shea et al., 1965; 70: Smart et al., 2000]. The set of accessible directions, dependent on rigidity, defines the *asymptotic cone of view* (or the asymptotic cone of acceptance) for a given station. On the other hand, for a given arrival direction at the station there is a minimum rigidity below which particles cannot gain access. This is termed the geomagnetic cutoff for that direction at that location and time [12: Duldig, 2001]. Above the minimum cutoff rigidity for a given arrival direction there may be a series of accessible and inaccessible rigidity windows known as the penumbral region [71: Cooke et al. 1991]. The penumbral region ends at the rigidity above which all particles gain access for that arrival direction. It is worth noting that cutoff rigidity of CRs being dependent on geomagnetic field decreases with increasing geomagnetic disturbance level [72: Danilova et al., 1999].

A conceptual illustration of an asymptotic cone of acceptance is presented in Fig. 37 [73: Shea & Smart, 1982]. The tracing of the allowed trajectories from the station through the Earth's magnetic field to IP space results in a family of trajectories that define an *asymptotic cone of acceptance.* The increased geomagnetic bending that lower rigidity particles undergo is illustrated by increased bending of the trajectories curving to the right. The direction of the trajectory at a distant surface, such as the magnetopause boundary, is the *asymptotic direction* of approach. The locus of points formed by the individual trajectory asymptotic directions depicted by the dotted line is used to illustrate the asymptotic cone acceptance [73: Shea & Smart, 1982].

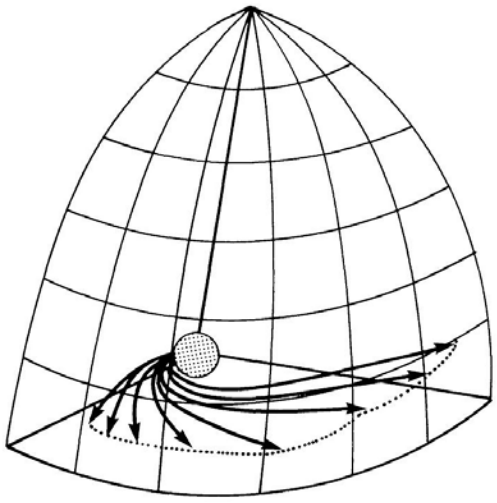

Figure 37: Conceptual illustration of an asymptotic cone of acceptance [73: Shea & Smart, 1982].

As the Earth rotates, CR incident on a given location must pass through different regions of the magnetosphere. Therefore the asymptotic directions are functions of the time of day [74: Bieber et al., 1992] and on the local time. As an example, Fig. 38 shows the daily variation of proton cutoff rigidities along the 260°E meridian [75: Smart et al., 1969].

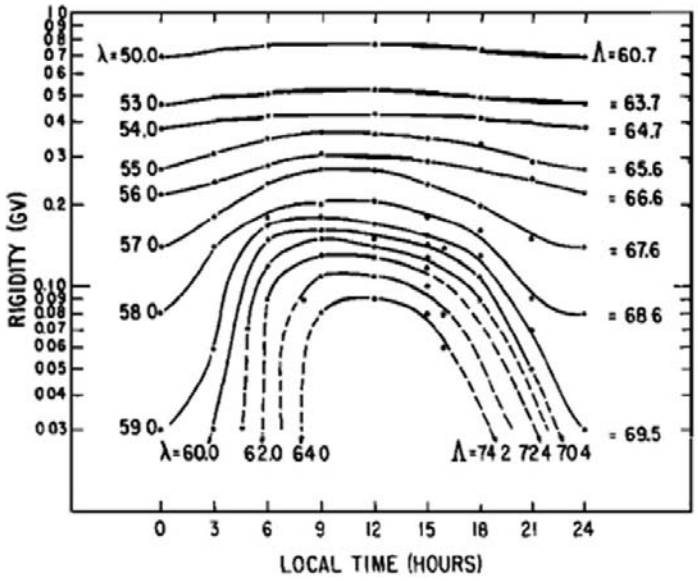

Figure 38: The daily variation of proton cutoff rigidities along the 260° E meridian. The data points represent the calculated values and the dashed lines indicate extrapolated values. λ indicates the geographic latitude along the 260° E meridian and Λ denotes the invariant latitude [75: Smart et al., 1969]

Thus, the *asymptotic direction* of a CR particle represents its direction of motion when entering into the magnetosphere. They are computed by means of numerical back-tracing of the particle trajectories in the geomagnetic field which is usually represented as a sum of magnetic fields from internal and external sources [72: Danilova et al., 1999; 74: Bieber et al., 1992; 75: Smart et al., 1969]. The magnetic field of internal sources is described by International Geomagnetic Reference Field (IGRF) models. The magnetic field of external sources is represented by the models of magnetospheric current systems such as ring currents, magnetopause currents and the magnetosphere tail currents.

For polar or even mid-latitude muon detectors that only respond to high-energy particles, the asymptotic cones of acceptance are restricted to specific regions of the celestial sphere. Thus if multiple stations simultaneously observe an anisotropic solar CR flux, it is possible to de-convolve the flux direction in space and the anisotropy [76: Cramp *et al.*, 1995]. If these stations are located at different geomagnetic cutoffs, it is possible to deduce the CR spectra [77: Smart & Shea, 2000]. Similarly, if a number of CR stations, each having asymptotic cones of acceptance viewing a different portion of the celestial sphere, rotate through a slowly evolving CR anisotropy, then it is possible to de-convolve the spatial anisotropy as in [78: Nagashima et al., 1994].

5.2 Global Muon Detector Network

Muon detectors have some advantages compared to neutron monitors because of a number of useful properties muons possess. Particularly, energy of muons is higher than energy of other particles, therefore when muons penetrate through a thick absorber other particles are stopped allowing muons to be easily detected. In addition, muons have minor energy losses and small angular displacement allowing determination of the incident directions of the primary cosmic rays. Thus, muons provide a way of measuring CR flux with high accuracy and low noise.

Today there is an informal tight collaboration between different teams working at muon stations all over the world. This network is constantly being developed, extending and including different organizations and institutes from different countries, namely, Japan, Brazil, USA, Australia, Kuwait, Armenia, Germany [79: Schuch, 2006]. In Germany, particularly, the MuSTAnG space weather muon telescope is currently being developed at the University of Greifswald to contribute to the development of European space weather technologies and services [32: Jansen et al., 2001; 80: Jansen & Behrens, 2008]. The most consistent part of the international collaboration is the Global Muon Detector Network (GMDN) which is described in several papers, e.g. in [27: Okazaki, 2008; 81: Braga et al., 2010] and today includes four muon stations listed in Table 4.

The GMDN detectors (specified in Table 4) have identical design, except for their detection area, consisting of two horizontal layers of plastic scintillators, vertically separated by 1.73 m, with an intermediate 5 cm layer of lead to absorb the soft component. Each layer comprises an array of 1m2 unit detectors, each with a 1 m x 1 m plastic scintillator viewed by a photomultiplier tube of 12.7 cm diameter. The Kuwait University detector consists of four horizontal layers of 30 proportional counter tubes (PCTs). Each PCT is a 5 m long cylinder with 10 cm diameter, having a 50 μm thick tungsten anode along the cylinder axis. A 5 cm layer of lead is installed above the detector to absorb the soft component. It is a hodoscope designed specifically for measuring the

''loss cone'' anisotropy, which is observed as a precursor to the arrival of interplanetary shocks at Earth and is characterized by an intensity deficit confined to a narrow pitch angle region.

Table 4: Information on GMDN detectors.

Station	Detection area, m^2	Number of viewing directions	Geographic Latitude	Geographic Longitude	Altitude, m
Nagoya (Japan)	36	17	35.1° N	137.0° E	77
Hobart[1] (Australia)	9 / 16	25	42.9° S	147.4° E	65
São Martinho (Brazil)	28	21 x 21	29.4° S	308.2° E	488
Kuwait (Kuwait)	9	23 x 23	29.4° N	48.0° E	50

[1)] There are shown two values for detection area which was enlarged from 9 m^2 to 16 m^2 in December 2010.

The GMDN began in December 1992, as two-hemisphere observations using a pair of muon detectors at Nagoya (Japan) and Hobart (Australia), which have detection areas of 36 m^2 and 9 m^2, respectively. Each of these detectors is multidirectional, allowing the recording of intensities in various directions of viewing. Another small (4 m^2) prototype detector in São Martinho (Brazil), was added to the network in March 2001 to fill a gap in directional coverage of the network over the Atlantic and Europe and then was upgraded in December 2005 by expanding its detection area to 28 m^2. In March 2006, the GMDN was completed to its current design, by the installation of a new detector at Kuwait University (Kuwait), with a detection area of 9 m^2.

The GMDN covers almost the entire globe, though it still has gaps remaining in its directional coverage over North America and the southern Indian Ocean (Fig. 39). Initial detection and tracking of a CME using muon detectors requires full coverage of the globe, as the earth rotates and different regions have a field of view that changes through the day. The gap over North America is particularly concerning and is an area where Canada could make a major contribution.

It is also worthwhile to mention the muon detectors other than GMDN telescopes that are also playing important role in international muon detector network. These detectors together with GMDN detectors are listed in Table 5 grouped by detection area *S*. The detectors underlined are those that publish or can publish data in real time.

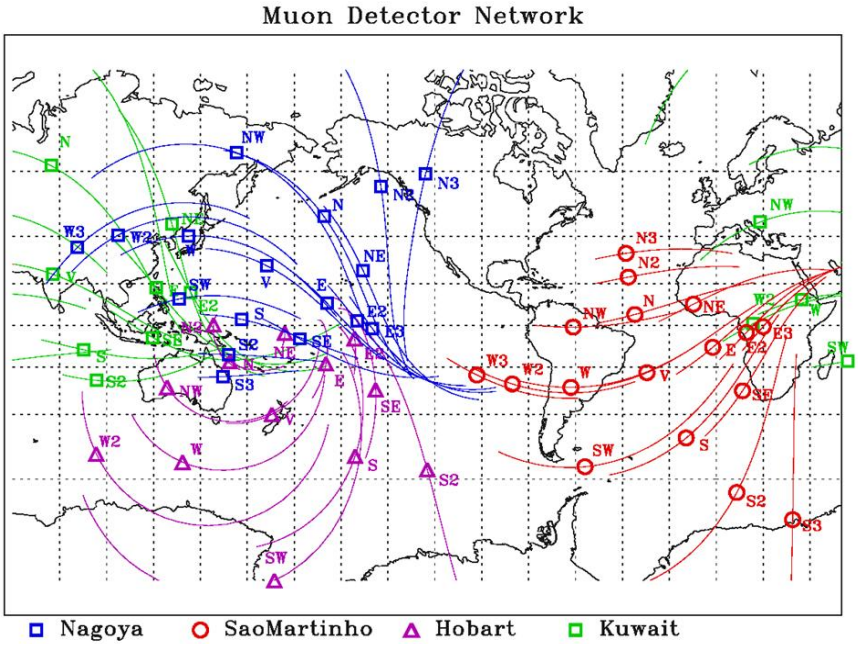

Figure 39: Asymptotic directions and global coverage by GMDN.

Table 5: International Muon Detector Network.

Detection area S	Number of detectors	Locations
$S \geq 9\,m^2$	6	Telescopes: Nagoya, Sao Martinho, Hobart Hodoscopes: Kuwait, Moscow (URAGAN), Ooty (GRAPES-III, 560 m^2)
$S \sim 2 \div 6\,m^2$	10	Greifswald, YangBaJing, Novosibirsk, Yakutsk CT at 0, 7, 20 и 40 mwe, Moscow CT Cube, Yerevan, Mawson
$S \sim 1 m^2$ (school devices)	>10	Santyago, Putre, Adelaide, Leonsito, Musala, Blagoevgrad, Belgrad, Hafelekar, Lodz, University Rochester (USA).

We note that the LC anisotropy has a small angular scale structure ~ 30^o. Therefore, observations require a relatively good angular resolution and high statistical accuracy [33: Nonaka et al., 2005b]. Recent success in two-dimensional observation of LC effects is mainly due to observations by muon telescopes with angular resolution smaller than ~ 10^o [30: Nonaka et al., 2003; 82: Fujimoto et. al., 2003; 29: Munakata et al., 2005]. Accumulation of LC events allows extraction of average and typical properties and features of LC effects as well as their correlations with the FD.

5.3 Real-time CR monitoring for space weather

An extension of the international muon detector network and recent achievements in data analysis have allowed the development of a real-time monitoring system of high-energy CRs for space weather applications. A LC display and bidirectional streaming display show the pitch angle distribution of the CR intensity variation. They can detect the precursor anisotropy prior to the arrival of the ICME and particle bidirectional streaming inside the ICME. See Fig. 40 with details explained in the figure caption.

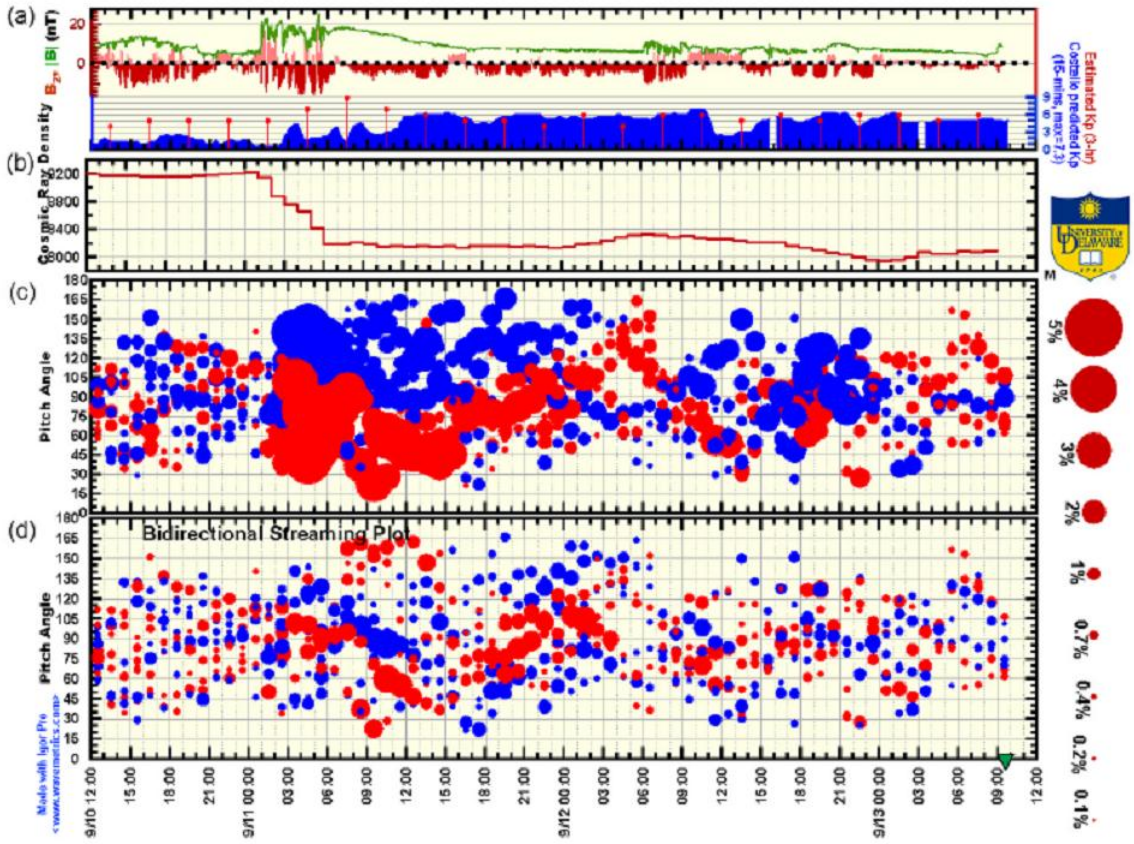

*Figure 40: Sample LC display and bidirectional streaming display in September 2005. (a) Plotted are 1-min ACE magnetic field magnitude |**B**| (green) and north-south component Bz (north, pink; south, red) in GSE coordinates. Also plotted are 3-hour estimated Kp index (red) and the 15-min predicted Costello Kp index (blue). (b) CR density. (c) CR intensity (circles) measured by a single Spaceship Earth station relative to the CR density. Red and blue circles indicate the deficit and excess intensity, respectively, and the radius of the circle scales with the magnitude of the deficit or excess; see right side of plot for scale. (d) Residual deviation after subtracting the fitted first-order anisotropy from each station. Red and blue circles represent deficit and excess relative to first-order anisotropy. In panels (c) and (d), the vertical axes indicate the pitch angle [83: Kuwabara et al., 2006].*

The first-order anisotropy analysis shows the particle flow direction and its magnitude. Individual station count rates tell us the time and scale of the Forbush decrease and ground-level-enhancement event at a single location. These displays are made by real time data processing and are updated to a World Wide Web server. It provides a new tool for space weather forecasting and for specifying conditions in the near-Earth space environment. This tool will become even more useful and reliable in the future, as more stations of the worldwide muon detector network together with neutron monitor network become available in real time [83: Kuwabara et al., 2006].

A distribution of particle intensity is shown in Fig. 41 [19: Asipenka et al., 2009]. The red circles show intensity deficit and yellow circles indicate intensity increase on different longitudes before and after the occurrence of the geomagnetic storm that happened on September 9th, 1992. One can see on the top panel that first, the closer the shock arrival time at Earth (vertical line), the more the red circles. Secondly, on September 7th one can clearly observe an increase in the number of red circles. As in the case of the aforementioned events, an intensity deficit can serve as a precursor of the storm.

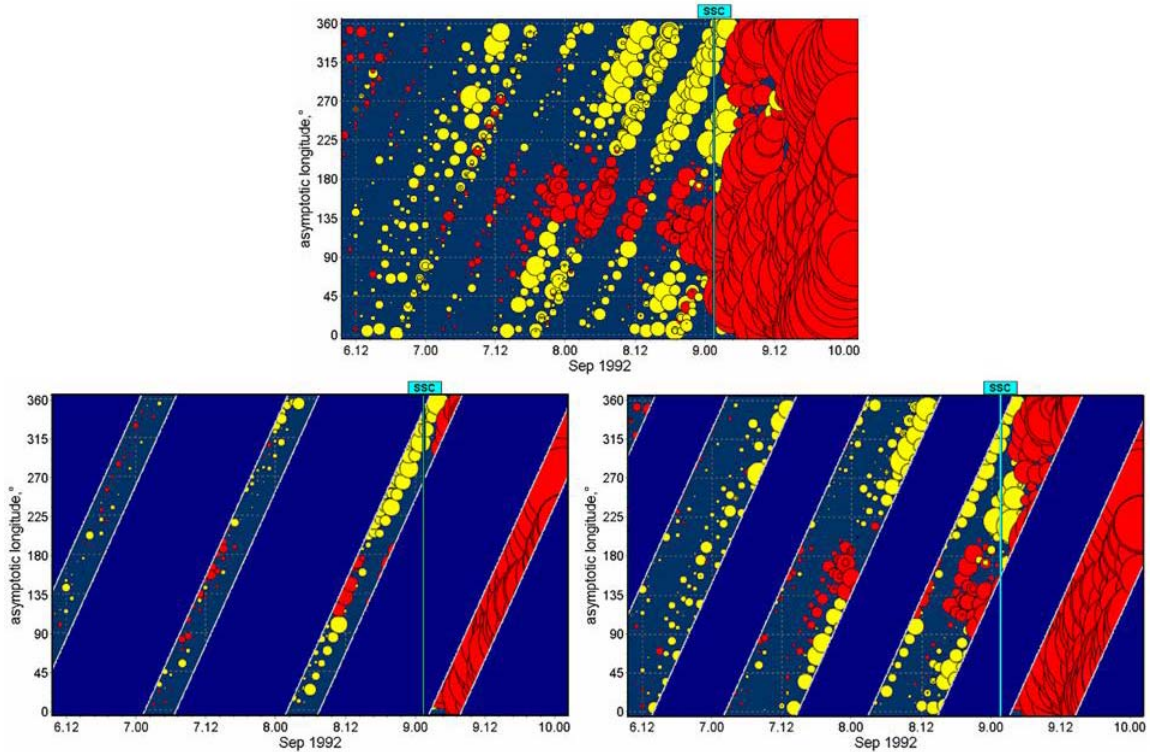

Figure 41: Precursors in real time observations.

The lower panels illustrate the same effect but with measurements taken from a few stations only. As a result, at a fixed time we do not have information about the particle intensity on all latitudes and so it is hard to analyse such data. Thus the sky coverage in the asymptotic directions of the stations should be as full as possible.

5.4 Canadian Muon Workshop

A workshop of experts was organized and held on 17-19 October 2011. This was located in the resort of Petite Rouge at St Emile de Suffolk in Quebec, which provided a distraction-free venue allowing all participants to focus on the questions in hand. There were 19 participants including 2 from Carleton, 1 from DRDC and 6 from NRCan. Several international experts were invited to give talks including:

John W. Bieber of the Bartol Research Institute, University of Delaware, USA.
Professor Bieber is the Principal Investigator of the University of Delaware Neutron Monitor program which operates cosmic ray neutron detectors at several locations including Inuvik, Nain, Fort Smith and Peawanuck. They generate an automatic alarm when a Ground Level Enhancement (GLE) starts. Professor Bieber has published extensively in this field.

Frank Jansen of the DLR German Aerospace Centre, Institute of Space Systems, Bremen, Germany. Dr. Jansen has written on the effects of space weather on aviation and communications and is an expert on European Space weather activities. He has participated in MUSTANG, a Bremen based cosmic ray detector using 2m x2m scintillation counters coupled to PMT's with wave length shifting fibres.

Lev Dorman of the Israel Cosmic Ray and Space Weather Centre and Emilio Segre Observatory. Professor Dorman is the author of a book titled "Cosmic Rays in the Earth's Atmosphere and Underground", and a respected authority on cosmic rays.

Kazuoki Munakata of Shinshu University, Matsumoto, Japan. Professor Munakata is the Co-ordinator of the Global Muon Detector Network (GMDN), an international collaboration which consists of nine institutions in seven countries: Japan, USA, Brazil, Australia, Kuwait, Armenia and Germany.

Victor Yanke of the Institute of Terrestrial Magnetism, Ionosphere and Radio Wave Propagation (IZMIRAN), 142092, Troitsk, Moscow, Russia. Dr. Yanke is director of the lab, and team leader on the Moscow ST Muon Multi-Directional Telescope.

Eugenia Eroshenko of the Institute of Terrestrial Magnetism, Ionosphere and Radio Wave Propagation (IZMIRAN), 142092, Troitsk, Moscow, Russia. Dr. Eroshenko works on the Moscow detector and also maintains the data repository for cosmic ray events.

The workshop was most useful in establishing several critical points which are
• Ground based detection of neutrons will not provide as good an early warning as muons, since their origin is in the lower energy cosmic rays.
• Ground based neutron detection is useful in confirming the arrival of a GLE.
• Directionality is an important characteristic of muon detectors – though not at the level of milliradians – an angular resolution of ±10 degrees is fine.
• A large angular range or coverage is required up to ±60 degrees or more.
• There is a need for a detector to cover North America, it is the one region of the globe which is not currently covered by the GMDN.
• A single detector will always have a high false positive rate, only when confirmed by several detectors in a network similar to the GMDN, will the false positive rate be reduced.

When the directions of approach in IP space beyond the magnetopause are mapped on a projection of extended geocentric coordinates, the set of accessible directions in space for each CR particle detectable at a specific location is uniquely defined in terms of geocentric coordinates. For conceptual purposes these asymptotic directions of approach are plotted on an extended Earth projection in order to help visualize the spatial region of cosmic-ray anisotropy with respect to the geocentric coordinate system [73: Shea & Smart, 1982].

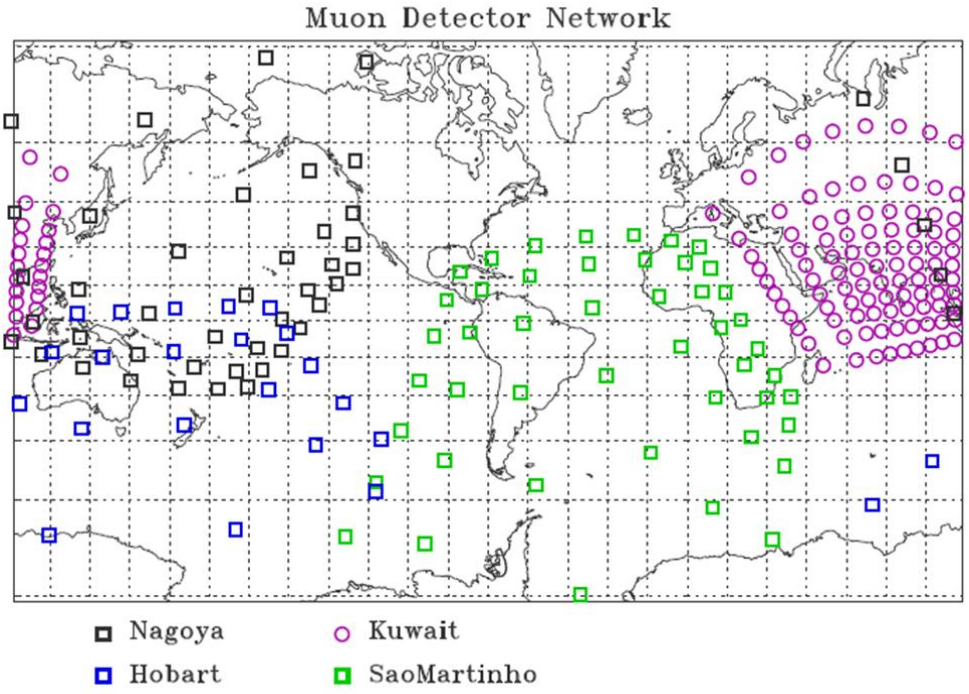

Figure 42: The current GMDN sky-coverage.

Figure 42 shows the world map projection of the asymptotic directions of approach computed for the GMDN stations at the median rigidity while figures 43 and 44 show the same projection with addition of the proposed Canadian muon detector in Ottawa and Vancouver respectively. The calculations are performed for each telescope of 5m x 5m proportional counter array with 11 x 11 =121 directions using the muon response function derived by [84: Murakami et al., 1979]. The values for cut-off rigidity are 1.7 GV and 2.6 GV for Ottawa and Vancouver respectively, the median rigidity is 52.4 GV and 52.5 GV in the same order. In addition, Fig. 45 shows asymptotic directions for a suggested station in Inuvik, Canada.

One can see that in Fig. 42, the region above North America and Atlantic are not covered but in figures 43 and 44 the presence of a muon detector in Ottawa and/or Vancouver appears to eliminate the deficiency of GMDN. A station in Inuvik would be also interesting because Inuvik has a very rare (unique) distribution of the asymptotic directions, especially in polar zone. The overlapped areas in the figures can be used to provide more accurate data in the network.

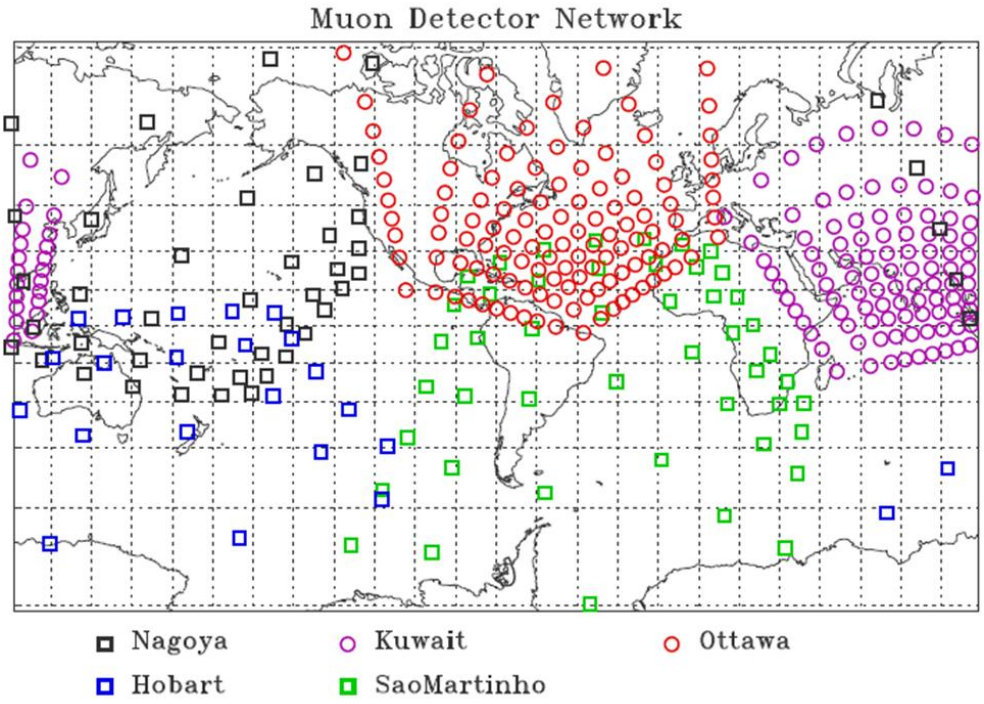

Figure 43: GMDN sky coverage extended by adding a proposed detector in Ottawa (cf. Fig. 42).

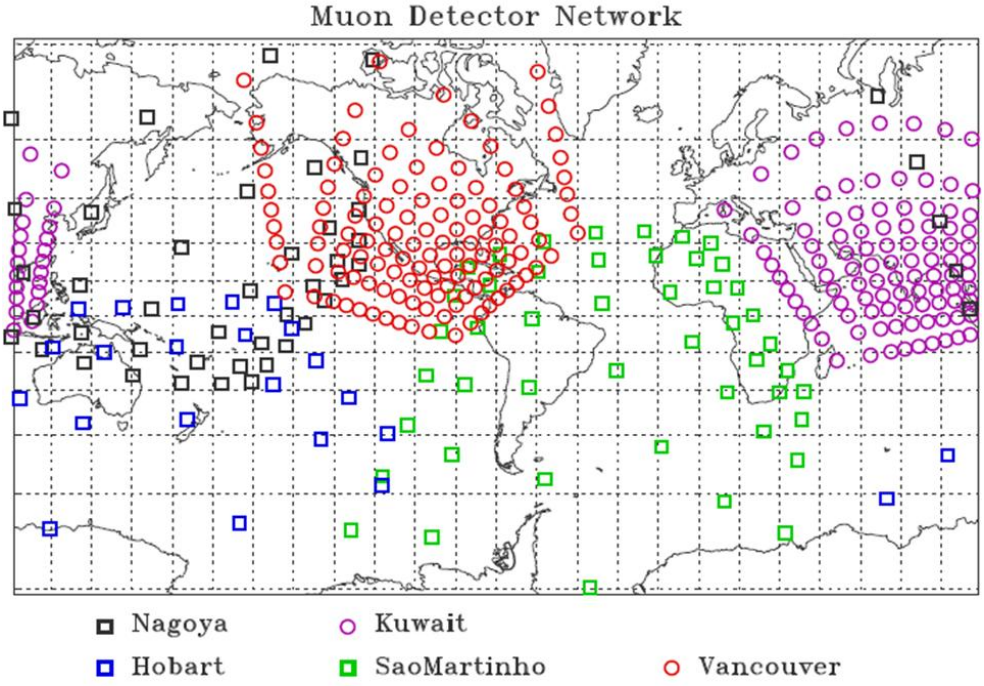

Figure 44: GMDN sky coverage extended by adding a proposed detector in Vancouver.

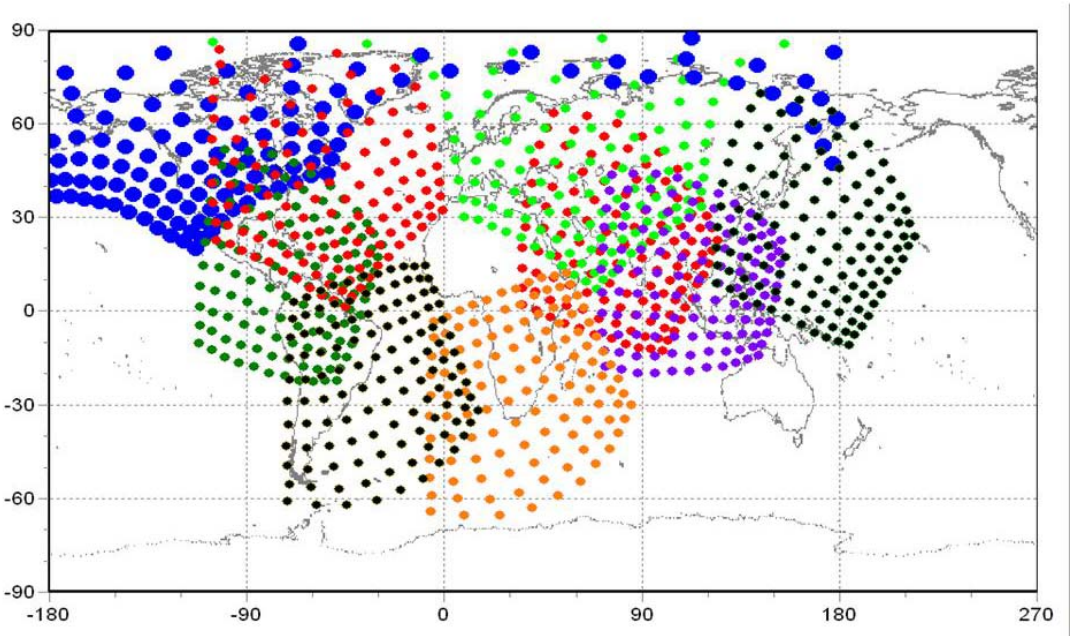

Figure 45: Maps of asymptotic directions with stations in Inuvik (big blue circles) and Ottawa (red circles overlapped with blue ones).

We emphasize that filling the mentioned gap by the presence of a proposed muon telescope in Ottawa would be of great importance as the interpretation of most cosmic ray modulation phenomena requires good latitude coverage. The prototype development that has been done at Carleton University is described in Section 6.

It should also be noted that Canada has a great experience in using ground-based CR detectors which were developed and located in different provinces, e.g. in Ontario (Ottawa and Deep River), in British Columbia (Victoria), in Alberta (Calgary) [85: Bercovitch & Davidson, 2012]. Unfortunately, today some of them are out of operation.

In October 12, 2012 NRCan organized a meeting [86: Knudsen et al., 2012] to discuss ways to bring the neutron monitor in Calgary back into operation after it ceased operation in 2011.

6 Experimental development

6.1 Technology choices for the muon detector design

The GMDN is composed of several detectors one of which is based on gas-filled detectors (at Kuwait University) and the other stations are composed of plastic scintillation counter detectors. Both of these technologies were evaluated.

Gas filled detectors rely on the deposition of ionization as a charged particle moves through an enclosed gas volume. A high voltage is used to sweep the electrons created towards a thin anode wire where they are amplified in a very high electric field causing an avalanche. Unfortunately many of these processes depend on the pressure: the initial ionization deposition, the drift velocity of the electrons and finally the amplification on the electron avalanche all depend on the pressure. The first two processes have a linear dependence – which is quite small, the latter has an exponential dependence which can be quite large. It is therefore quite difficult to provide enough gain to overcome the electronic thresholds in all situations, and at the same time avoid saturation of the electronics, which reduces the overall accuracy of the devices.

Another option is to use scintillation counter devices. These are fairly immune to pressure variations and with careful design can avoid temperature effects. From a point of view of maintaining a long term monitoring facility they offer many advantages over the gas filled detector. However they tend to be more expensive than gas filled detectors for the same technical specifications: positional accuracy etc. As a result a prototype gas-filled detector (named FOREWARN) was constructed and started taking data in February 2012 [87: Boudjemline, 2012].

The Muon tracking system built at Carleton University uses available devices that were used in the past by a different experiment [88: Boudjemline, 2011; 89: Boudjemline, 2010]. This provided us with some components for use which was of great importance due to the limited project duration. The goal is to track cosmic-ray muons by providing the hit position and so the angular distributions in two directions. The research group at Carleton University had to perform all stages from the evaluating of the system performance, to prototype design, data collection and their evaluations for their representation of CR variations. This work also provided experience in running a large array of scintillation counters which is very important for the feasibility study. The detector is not ideally designed for contributing to the GMDN, having a limited angular range and positional accuracy that is two orders of magnitude too fine. However it will give experience in the type of pressure, temperature and diurnal corrections that are required to be sensitive to the initiation of solar storms.

6.2 Computer simulations of muon detector

The muon detector is aimed in a vertical direction and has an angular acceptance of up to +\- 25 degrees. It will record the direction of charged particles with an accuracy of around 2 milliradians (mr). Though fixed, it has sensitivity to particles coming directly from the Sun during a period of 4 hours around noon. It is also sensitive to particles which might be following the magnetic field lines: orientated at 20 degrees to the vertical in Ottawa.

6.2.1 Preliminary simulations of detector components

The initial design of the main detector is shown in Fig. 46, which comprises two planar drift chambers (DC1, DC3) with active areas of 1.2m x 0.4m. They are placed above each other with a gap of 1m between them. Scintillation counters (Sc1 - Sc5) are placed above and below the drift chambers to provide the main trigger and to provide left/right discrimination (L, R).

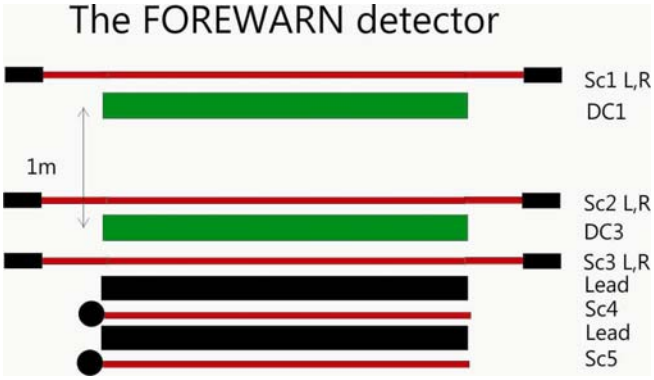

Figure 46: Initial scheme of the FOREWARN detector.

The spectrometer is comprising two layers of 4" (10cm) lead interspersed with scintillation counters. The data from these scintillators will not be included in the main trigger but will be recorded in coincidence with the drift chamber data. There is some sensitivity to the low energy spectrum: the elevation above sea level and the cut-off rigidity are 145m and 1.25GV respectively.

Two different calculations were done to simulate the telescope components. The first one was for setting the vertical position Z of the drift chambers, the X and Y positions of the scintillators and the size of the absorbers. The second was for a study of the absorption of CR particles in different lead thicknesses.

The first simulation generates events using $\cos\theta^2$ distribution. The spatial resolution in the drift chambers used is 3mm in each direction. In the direction perpendicular to the wire X, the side where the muon traversed the chamber is decided by the scintillator above each chamber. An example is given in Fig. 47, where the left and right sides are defined with respect to plane x=0 so that for chamber 1 (red color), the scintillator 1 (blue color) corresponds to the left side and the

scintillator 2 (blue color) to the right side. Since the spatial resolution in the drift chambers is limited, the system has the left-right ambiguity led to mis-reconstructed events. Figure 47 shows such an event which is at the right of the chamber 1 (a white small spot near the plane x = 0) while the information of the event is obtained from the scintillator 1 corresponding to the left side (a black small spot close to x = 0).

The number of mis-reconstructed events depends on the distance between chambers and decreases with the distance. On the other hand, increasing the distance will reduce the flux within the geometrical acceptance. Thus there exists an optimal value for the distance between chambers, which can be found by simulation with CRY Software. One of the acceptable values for the distance was found to be 50cm when the fraction of mis-reconstructed events is 1.3%.

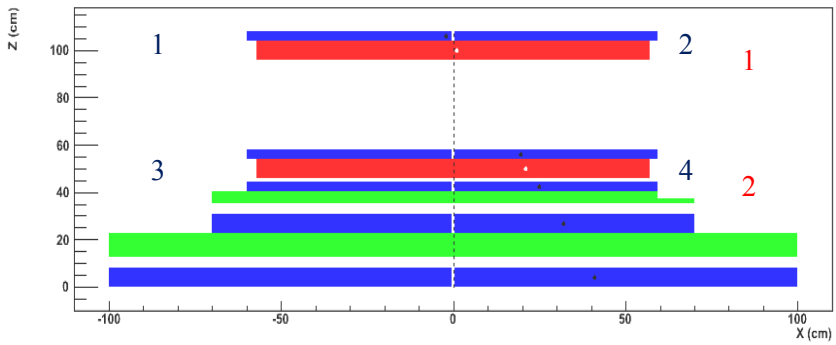

Figure 47: Example of a mis-reconstructed event due to left-right ambiguity. The event is at the right side of the chamber 1, but the information obtained from the scintillator is left.

The angular distribution of the reconstructed tracks has been compared to the true distribution as shown in Fig. 48. If nonregular events occur at a large angle, they will be easily distinguished. The main disagreement between both is due to the spatial resolution. Few events due to the left-right ambiguity can be seen at the bottom plot of the same figure.

The spread of the events in the iron support slabs define the size of the lead that we should use (Fig. 49). Unfortunately, in Y direction, the available scintillators were not wide enough and cannot cover the desired width. This can be corrected by an angular cut using the muon hit positions at the drift chambers.

To study the absorption of events in the lead, cosmic-ray particles were generated using Cosmic-ray Shower Library (CRY) [90: CRY software] at 0^o altitude and 45^o latitude (cf. Ottawa: 45.4^o N, 75.7^o W). Only charged particles were selected. Figure 50 shows the total flux as a function of the particle momentum up to 10GeV/c. Only muons, electrons and protons are plotted. The flux of kaons and pions is negligible.

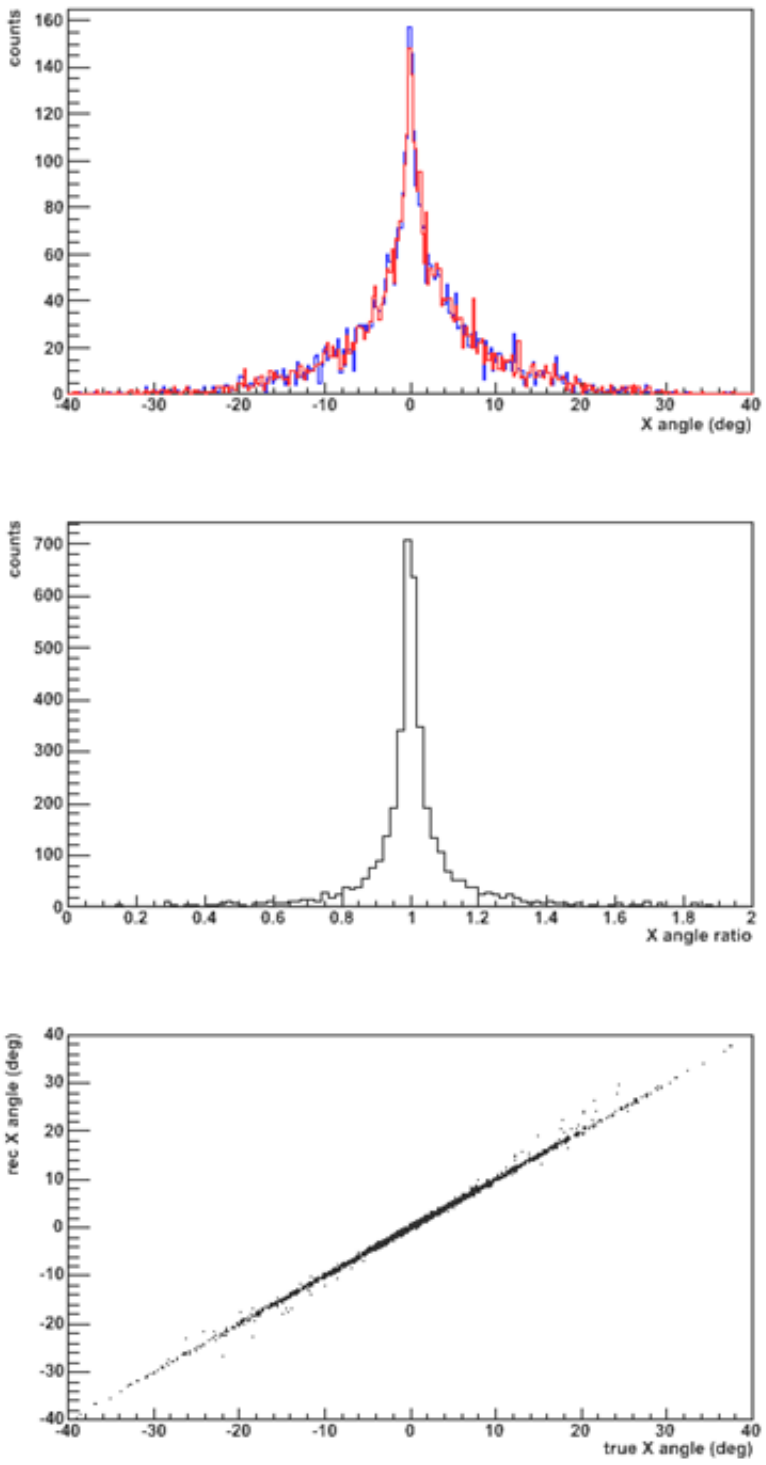

Figure 48: Top: true (blue) and reconstructed (red) angular distributions. Middle: Ratio of distribution. Bottom: reconstructed versus true.

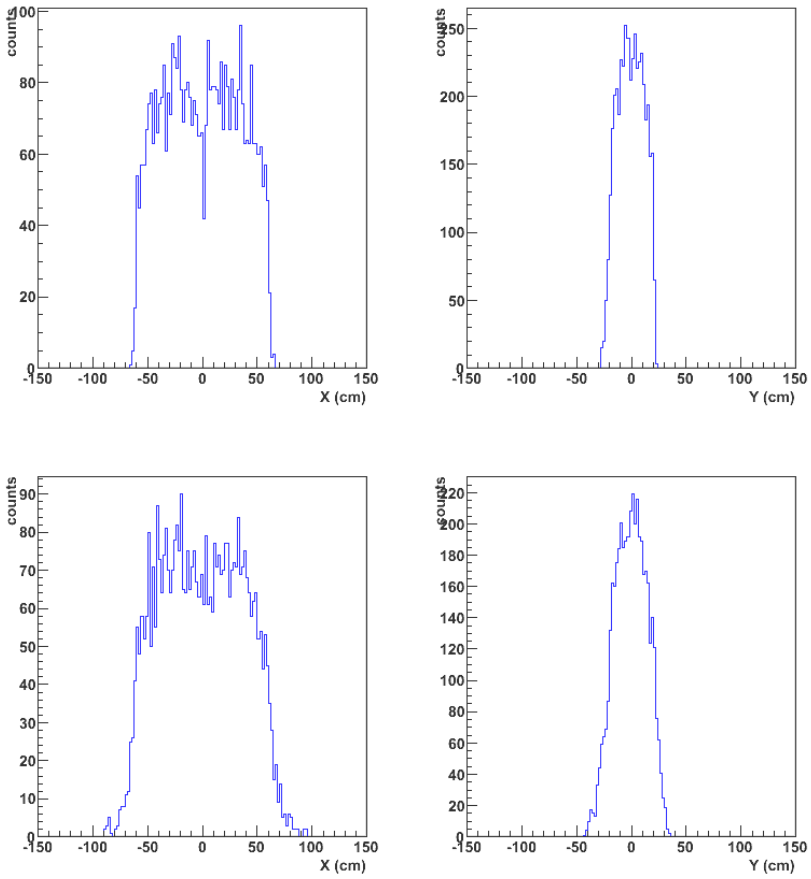

Figure 49: X and Y distribution on the bottom of the lead layers (top of iron support slabs).

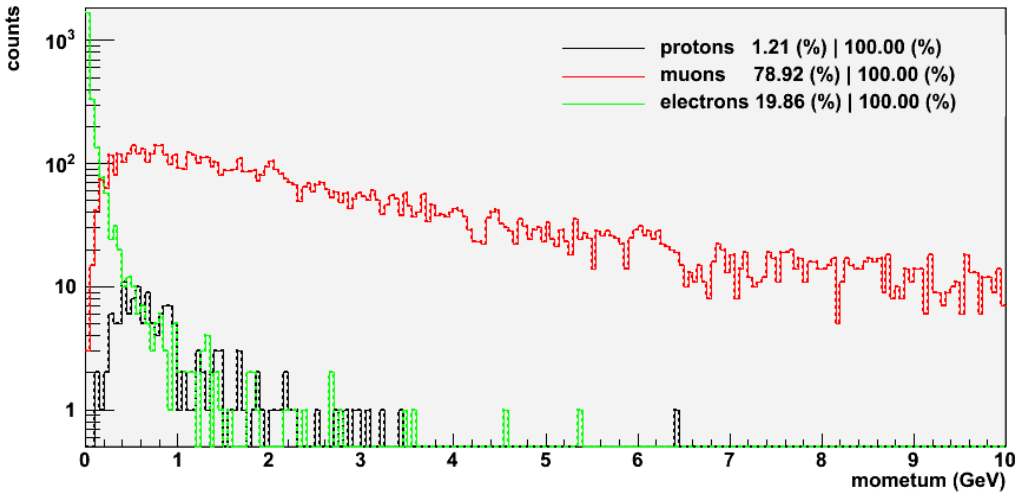

Figure 50: Cosmic ray flux obtained with CRY software.

The influence of the lead thickness on the flux of each particle has been also modelled (Fig. 50 corresponds to the zero-thickness case). The modeling was based on [91: Groom et al., 2001] and web databases ESTAR [92: ESTAR program] and PSTAR [93: PSTAR program] developed at The National Institute of Standards and Technology (NIST) in US. As is shown in Fig. 51, thickness of 5cm of lead (first layer) is enough to cut all electrons, while 15 cm thickness of two lead layers cut muon with momentum below ~0.25 GeV/c. The ideal is to use a thicker lead layer but, unfortunately, this amount of lead was not available. The resulting dependence of the mean minimum momentum on the thickness of the lead is shown in Fig. 52.

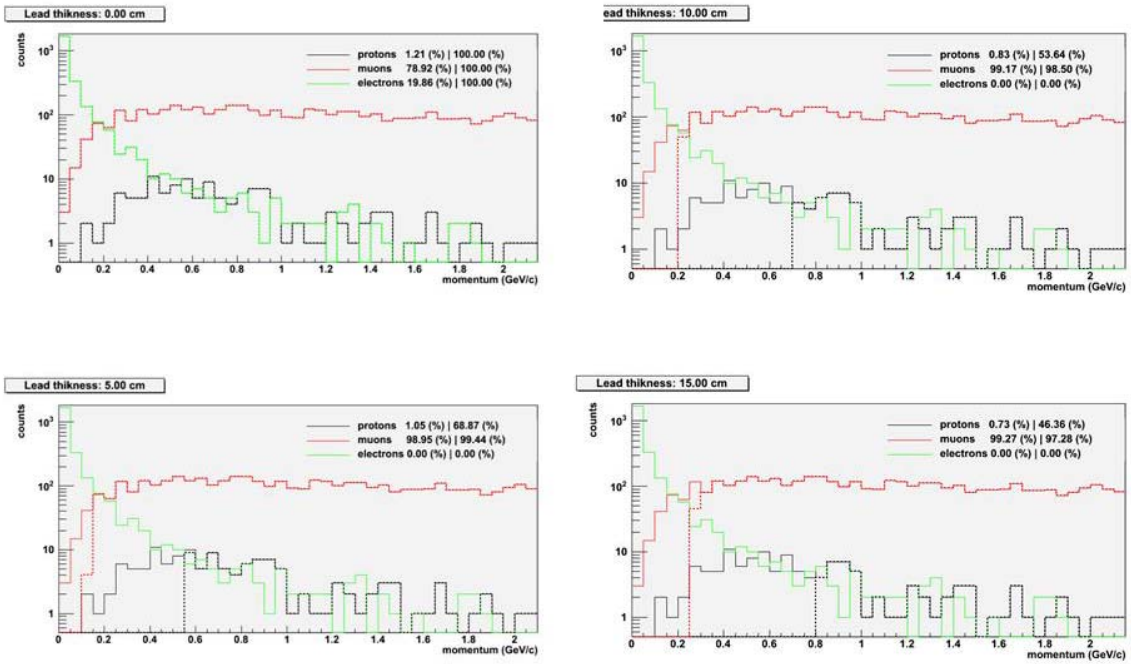

Figure 51: Effect of lead thickness on the fluxes of particles. Solid lines are the initial fluxes, dashed lines are events which traverse a given lead thickness.

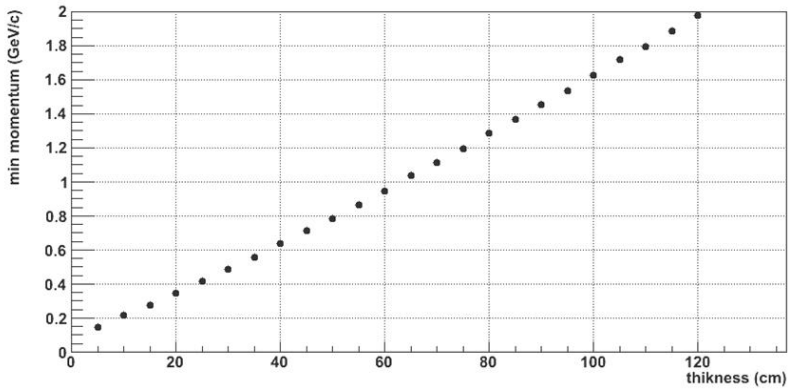

Figure 52: Mean minimum muon momentum which traverses a given lead thickness.

Note that these numbers are an average value. The fluctuation in the energy loss is not taking into account. To study the energy loss in the whole system in details, the GEometry ANd Tracking (GEANT4) simulation package has been used [94: GEANT4 software] as shown in the following part.

6.2.2 GEANT 4 Simulation of muon tracking system

The main parameters involved in simulation of the response are the geometry of the detector, the type of particles involved and the physics used for each particle.

The geometry and different trigger stages is shown in Fig. 53, plotted with GEANT4 software. Tables 6 presents components of detector materials used in simulations and Table 7 lists the materials used for the simulation.

Table 6: Materials of components used for GEANT4 simulation.

	Type	#	Thickness	Material	Formula	Density (g/cm^3)
Trigger	Plastic scintillator	10	6 x 0.3 cm 4 x 1.5 cm	Polystyrene	C8H8	1.04
Detector	Drift chamber	2	7.1 cm	See table 2	See table 2	See table 2
Absorber1	Lead	2	10 cm	Lead	Pb	11.35
Absorber2	Iron	2	2.5 cm	Iron	Fe	7.87

Table 7: Drift chamber materials used for GEANT4 simulation. The numbers are shown for a single drift chamber.

	Material	#	Thickness	Density (g/cm^3)
Active	Argon gas	1	1.5 cm	1.78×10^{-3}
Electrodes/ shielding	Copper	4	60 mm	8.96
G10 skin	SiO2	4	3.1 mm	1.91
Styrofoam	Polystyrene	2	2.5 cm	0.03

The main secondary cosmic ray particles include electrons, muons and protons. The particles have been generated using CRY software [90: CRY software]. The physical processes for each type of particles taken into account in the simulation are listed in Table 8.

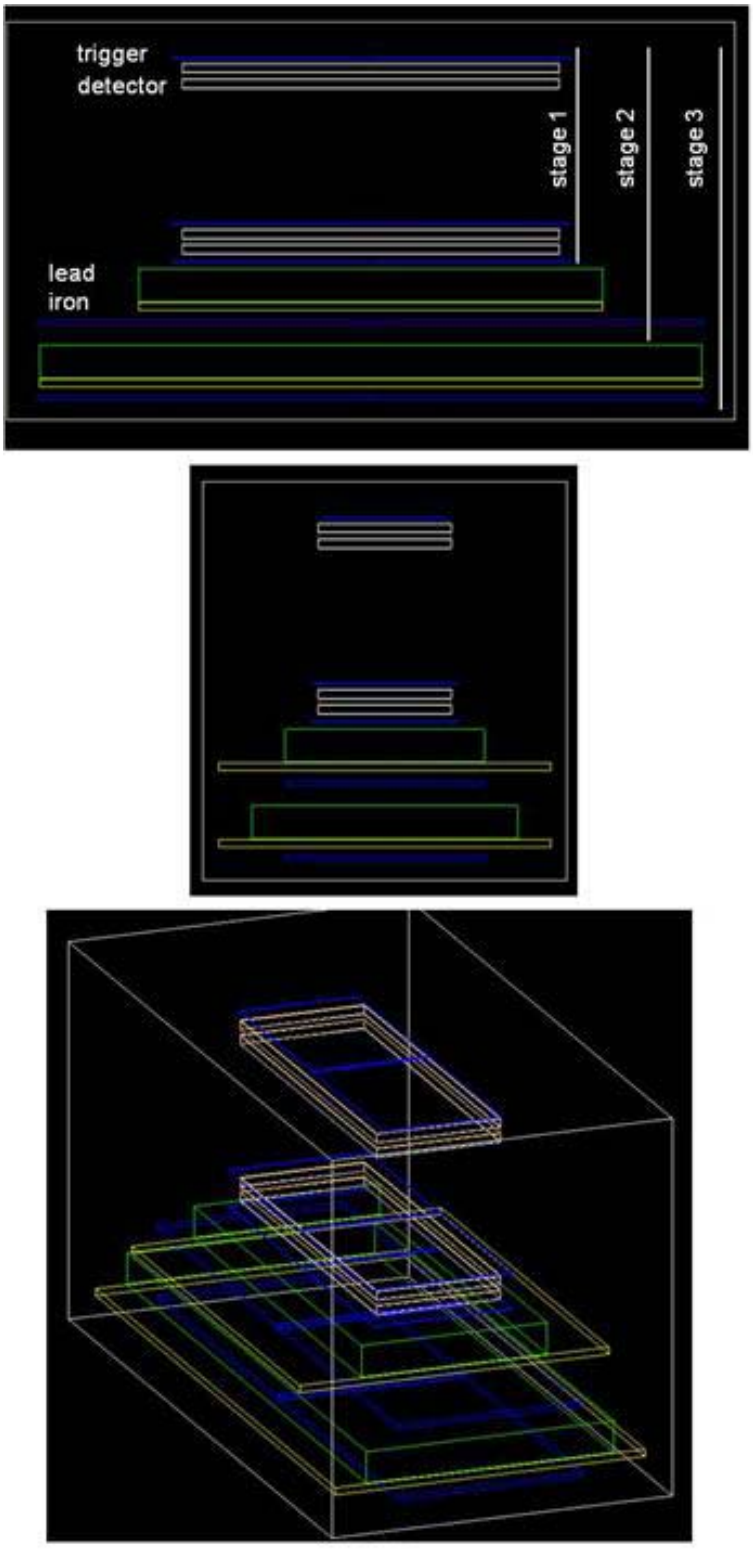

Figure 53: Geometry of Forewarn Detector plotted with GEANT4 simulation.

Table 8: Physics used for each particle in GEANT4 simulation.

Particle	Multiple scattering	Ionization	Bremsstrahlung	Pair production
Proton	x	x		
Electron	x	x	x	
Muon	x	x	x	x

As demonstration, GEANT4 simulation of a 0.5GeV/c muon track is presented in Fig. 54.

Interaction of muons, electrons and protons during their propagation through layers of the FOREWARN detector are modelled and shown in Fig. 55. It presents the interaction of each particle with different materials of the detector. Most of the muons traverse the whole system. Electrons can make it up to the second stage only. Most of them are trapped in the first and second stage. In the case of protons, some of them are absorbed in the first lead layer and some in the second lead layer. Few of them can make it to the last stage. The energy loss for each trigger stage is shown in Fig. 56.

Summary of the expected number of events for each trigger stage is presented in Fig. 57. From top to bottom: stage 1, 2 and 3. In each plot (each stage), the solid lines are the generated fluxes. The dashed lines are the survived events due to the geometrical acceptance and to the energy loss in different materials. Three columns presented at the top left corner of each figure are (from left to right):

- Fraction (in %) of each particle to the total number of events.

- Fraction (in %) of each particle to the generated number of events for the same particle type.

- Fraction (in %) of each particle to particles survived in stage 1.

The last fraction is the most important. It allows us to compare the detected number of events in each stage. It follows from Fig. 57 that the number of muons in the second and third stages will be reduced by 5% and 17%, respectively, compared to the main stage (stage 1). The minimum muon momentum is around 0.2 and 0.4 GeV/c in these stages, which is in good agreement with the previous calculations [90: CRY software].

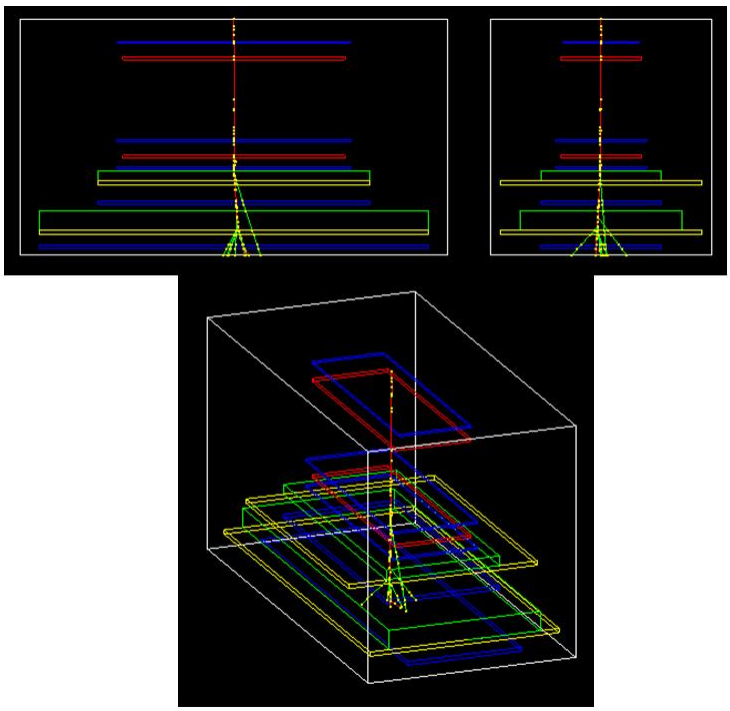

Figure 54: GEANT4 simulation of FOREWARN Detector. An example of a 0.5GeV/c muon is shown.

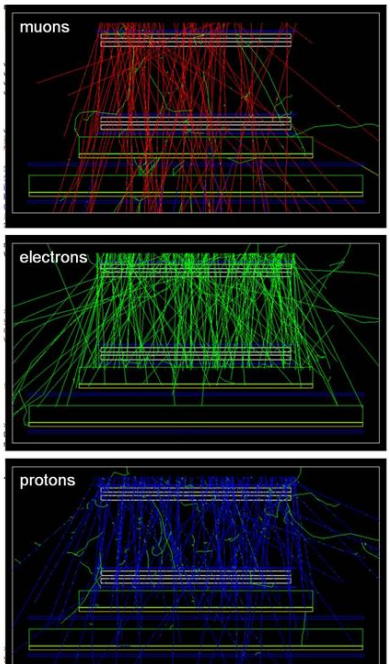

Figure 55: Particle interaction with different materials. Each particle is shown separately. Gammas are not shown for better visual view. Secondary electrons are shown in green in each plot.

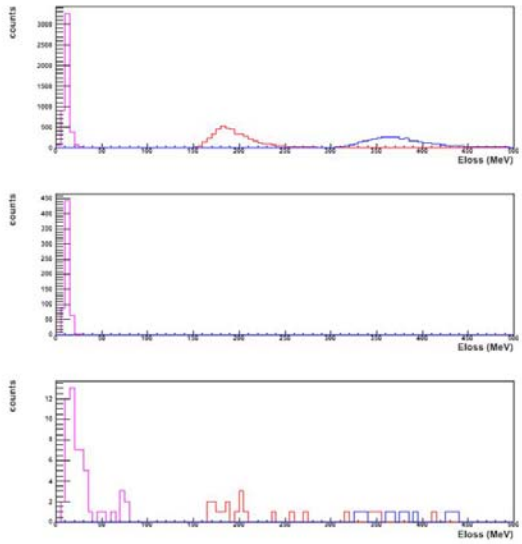

Figure 56: Energy loss for each trigger stage and for each particle.

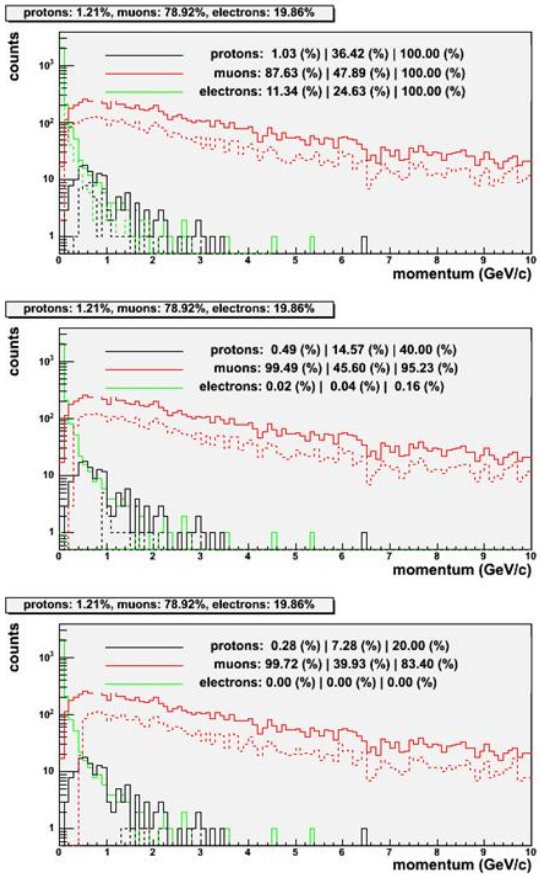

Figure 57: Expected number of events for each trigger stage. The initial fraction of each particle is the same and is shown at the top of each plot.

6.3 FOREWARN detector construction

6.3.1 Drift chambers

The muon detectors are a single wire drift chambers. Two chambers are available and cover an area of 40 x 114 cm^2 each. With a muon flux of 1 $min^{-1}cm^{-2}$, the expected number of muons per chamber is then 4560 min^{-1}. The muon flux is reduced mainly because of the geometrical acceptance of the system. The distance between both detectors has been chosen according to Monte-Carlo simulation results.

Another important point is the ambiguity left-right for this type of detector. With a single anode wire, the information that we measure in the direction perpendicular to the wire is the drift time. Since the wire is located in the centre of the chamber, only external trigger can provide the side where the muon traversed the chamber.

6.3.2 Triggers

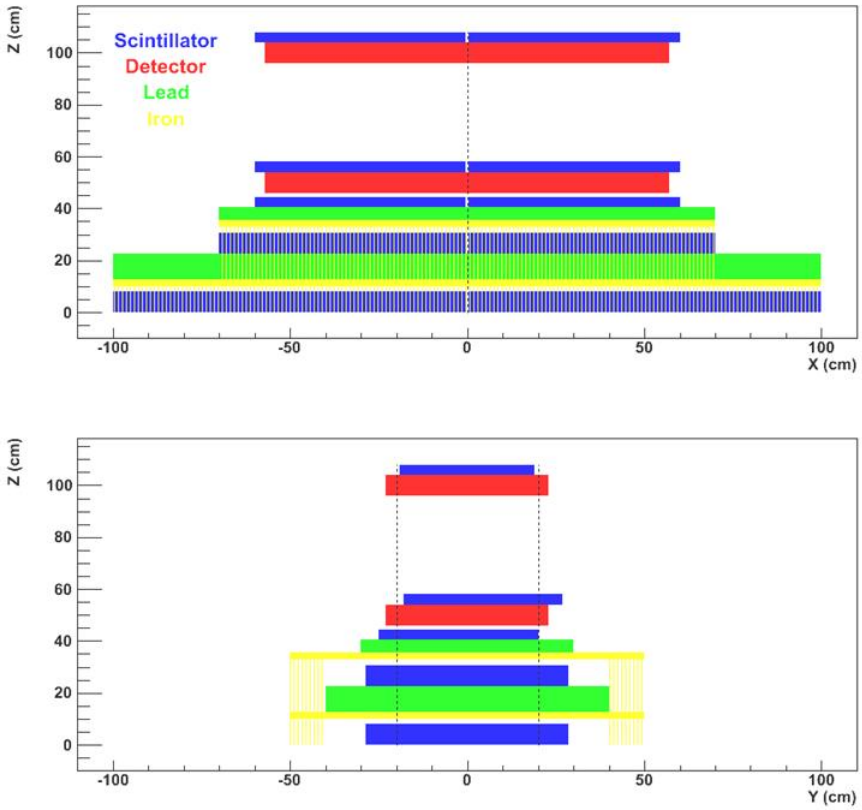

Figure 58: Design of FOREWARN detector. The thickness for each component is the total thickness (active + support + shielding + ….). Example: the scintillators sit on a piece of wood.

The triggering is done using plastic scintillators. Five planes are used as shown in Fig. 58. Each plane consists of two scintillators. In the first three from the top, the main trigger, the scintillators are sitting at each side of the anode wire. The other planes consist of two scintillators which sit one over the other to compensate their inefficiency. The main trigger will track all type of events. The first stage (stage-1) consists of the main trigger in coincidence with the scintillators below the first lead layer to cut low energy particles. The second stage (stage-2) gives information about the minimum muon momentum. Figure 59 shows a scheme of all coincidences.

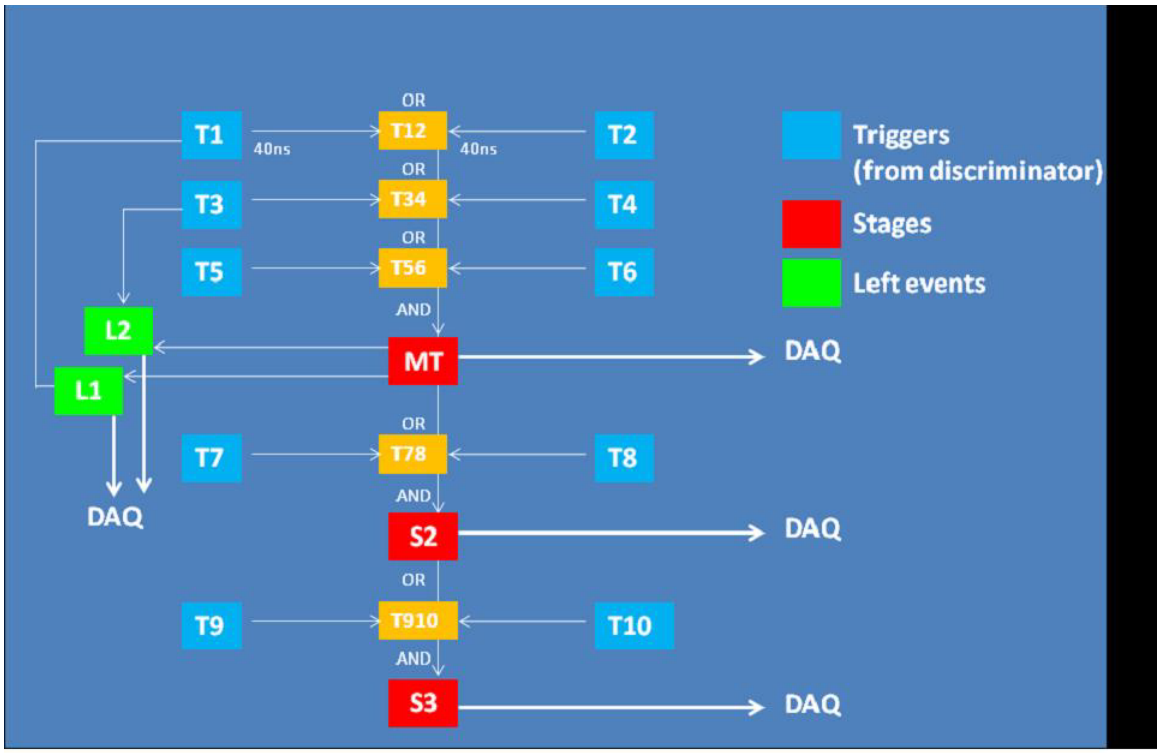

Figure 59: Scintillator coincidence scheme.

6.3.3 Absorbers

Two stages of lead are used to absorb low energy particles like electrons, protons and particles which results from scattering into the roof or from any type of present radioactivity. The thickness is 10 cm each. Each lead layer consists of a many lead pieces of 5 x 10 x 20 cm^3 (~12kg each) and sit on 2.5cm iron slab.

Photos in Fig. 60 shows the construction steps in building the FOREWARN tower and the ready detector.

Figure 60: Construction of FOREWARN detector (add photo of the complete thing).

6.4 Analysis of FOREWARN system performance

6.4.1 Data analysis

The trigger gives information about the count rate but not the direction of the events. We define a trigger event as an event observed in at least the main trigger and which do not have a zigzag path from scintillator plane to another. The second scintillator stage which supposes to filter the background and keeps only the muons, is not efficient at 100% and must be corrected. The measured efficiency of a single scintillator is shown in Fig. 61. Assuming that all scintillators with the same size have the same response, the same figure shows as well the combined efficiency obtained from two sintillators (from stage-1 or stage-2) by using an .OR. between both.

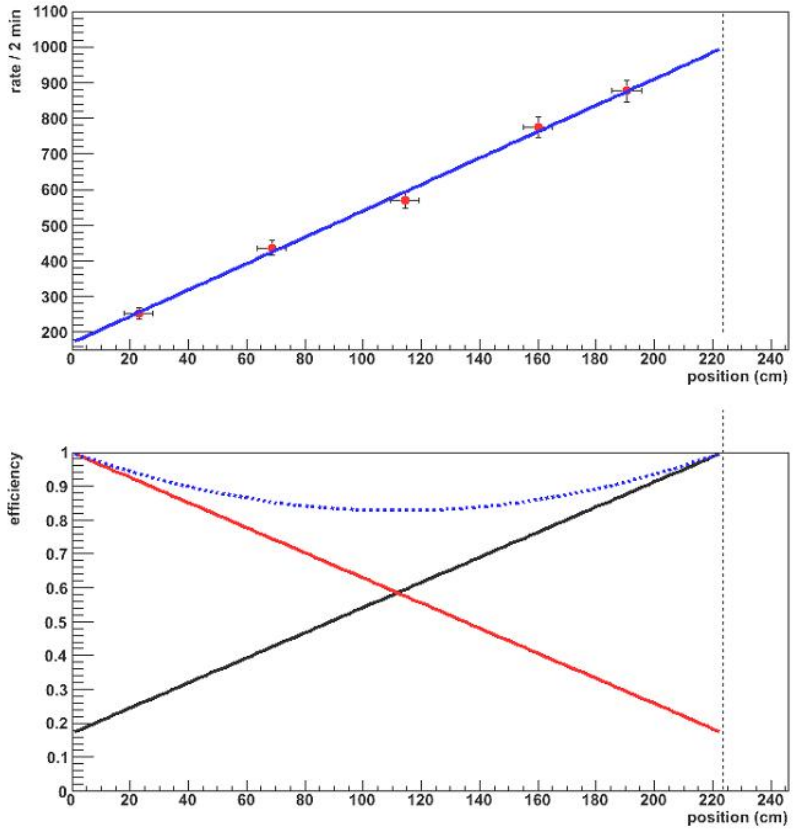

Figure 61: Top: measured muon rate as a function of the position along the scintillator. A pair of smaller scintillators is used for event coincidence. Bottom: efficiency of two scintillators sitting one over the other (back and red) and the combined efficiency in blue using an .OR.. The efficiency is assumed = 1 (100%) close to the PhotoMultiplier Tube (PMT).

The new stage-1/trigger event is defined as follow: S1(1)+S2(1)|S1(0). With S1(1) are events detected in stage-1, S2(1)|S1(0) are events detected in stage-2 but not in stage1. This is a rough correction which should raise the efficiency. The stage-2/trigger can be corrected by using the results from the correction of stage-1. A chamber event is defined as a trigger event and an event which shows a pulse in each chamber (above a certain threshold). The details about the drift

chamber data analysis are given in [89: Boudjemline, 2010]. The inefficiency of both scintillators in both stages is corrected as follows:

- perform a linear fit between the event hit positions in the drift chambers;

- extrapolate the vertical position of each stage;

- reweight each event according to the combined efficiency plot shown in Fig. 61.

6.4.2 Pressure correction

Many parameters can affect the shape of the muon count rate, such as low statistics (small scale system); atmospheric parameters (pressure, temperature, humidity, clouds etc.); solar cycle (primary cosmic ray flux); solar activity (ICME propagation), and others.

In addition to that, the response of the drift chamber is sensitive to the pressure. The primary charge increases with the pressure, but the avalanche gain decreases. The avalanche gain has to be high enough to avoid that the chamber becomes inefficient for some events.

The pressure has the most effect on the flux with the absence of any solar activity. In this analysis, only the atmospheric pressure effect is corrected on the muon count rate using a linear regression method as follows [95: Dorman, 1972]:

$$I_c = I - \bar{I}\,\beta_P\,(P - \overline{P})\ , \tag{8}$$

where I, I_c and $\bar{I}$ are measured, corrected and average muon counts respectively, P is the atmospheric pressure, $\overline{P}$ is an average atmospheric pressure (taken as 1000.0 hPa), β_P is the pressure coefficient in %/hPa. Each correction is usually performed separately for a given directional channel. Due to the effect of the absorption in the atmosphere, the pressure coefficient is negative indicating an anti-correlation between observed flux and the atmospheric pressure [96: Famoso et al., 2005]. The pressure coefficient β_p is obtained using the correlation factor CF from

$$\bar{I} \cdot \beta_p = CF \cdot \sigma_I / \sigma_P\ ,$$

where

$$CF = \frac{\frac{1}{N} \cdot \sum_{i=1}^{N} (I_i - \bar{I})(P_i - \overline{P})}{\sigma_I \sigma_P}\ , \qquad \sigma_I = \sqrt{\frac{1}{N}\sum_{i=1}^{N}(I_i - \bar{I})^2}\ , \qquad \sigma_P = \sqrt{\frac{1}{N}\sum_{i=1}^{N}(P_i - \overline{P})^2}\ ,$$

I_i and P_i are measured muon count and atmospheric pressure for a time bin i. The temperature correction could be made by a formula similar to Eq. (8) where the pressure coefficient β_p should be replaced by the temperature coefficient β_T and the pressure variation $(P - \overline{P})$ by the deviation of the altitude of 100 hPa to its annual average [97: Blackett, 1938; 27: Okazaki et al.,

2008; 81: Braga et al., 2010]. However, this approach has not been used because of the absence of information; instead the surface temperature is used for comparison.

6.4.3 Results

The results are based on data measured for 5 days from January 17 to 22, 2012.

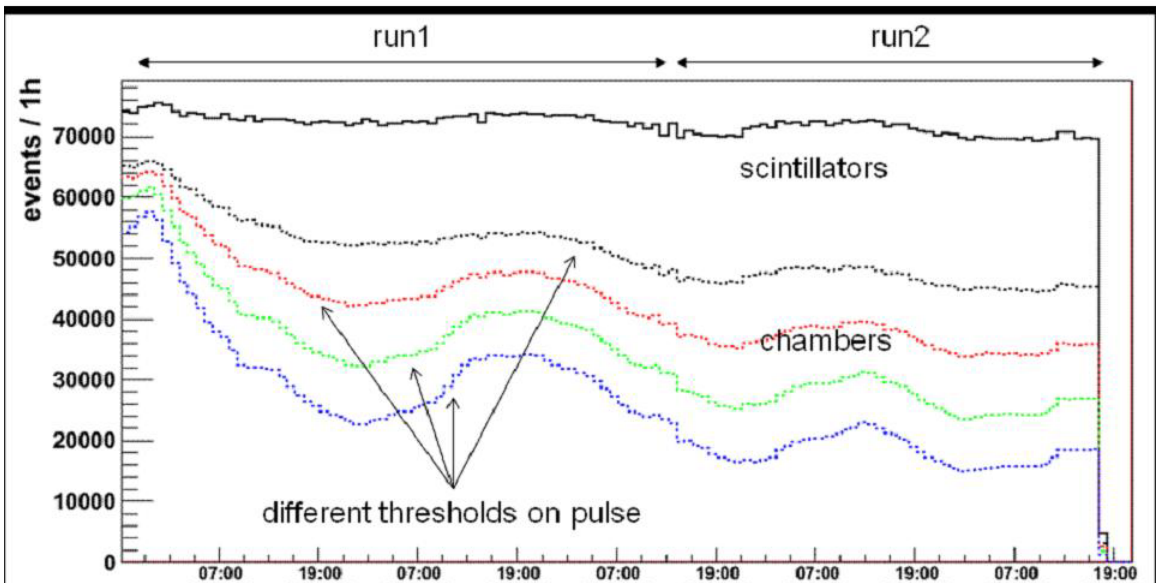

Figure 62: Main trigger: event count rate as a function of time for the scintillators (black) and for the chamber (dashed lines) for different thresholds. The rate decreases for higher thresholds.

Variations of the event count rate obtained from the main trigger and from the drift chambers for different thresholds are shown in Fig. 62. The same variation over time is observed in the scintillators and in the chambers, except that the difference in amplitude between high and low spots is significantly higher in the chamber especially at higher thresholds. This can be explained by a low avalanche gain in the chambers especially at high pressure which make the chamber less efficient. Increasing the gain by increasing the high voltage difference between the anode and the cathode should correct that.

Figure 63 shows the variation of the event count rate for the main trigger compared to the stages observed in the scintillators. The rate decreases with the stages because mainly of the absorption of some events by the lead layers. The remaining events are muons at 99.5% and protons at 0.5% in stage-1 according to GEANT4 simulation. The correction due to the inefficiency of the scintillators in both stages raises slightly the rate by around 11% which is in good agreement with Monte-Carlo.

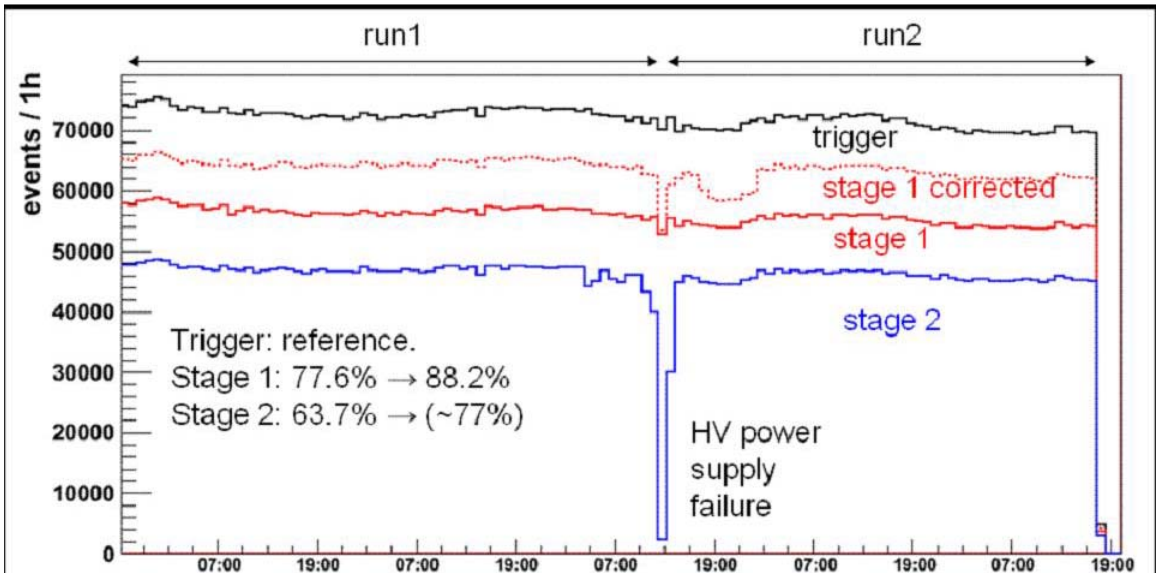

Figure 63: Scintillator event count rate as a function of time for the main trigger (black) and for both stages in red and blue. The dashed line plot shows the corrected rate for stage-1.

A drop in the rate is observed in stage-2 due to a failure in the high voltage power supply. This affects the corrected rate of stage-1 as well as explained in the data analysis section. Note that the pattern does not change from stage to stage.

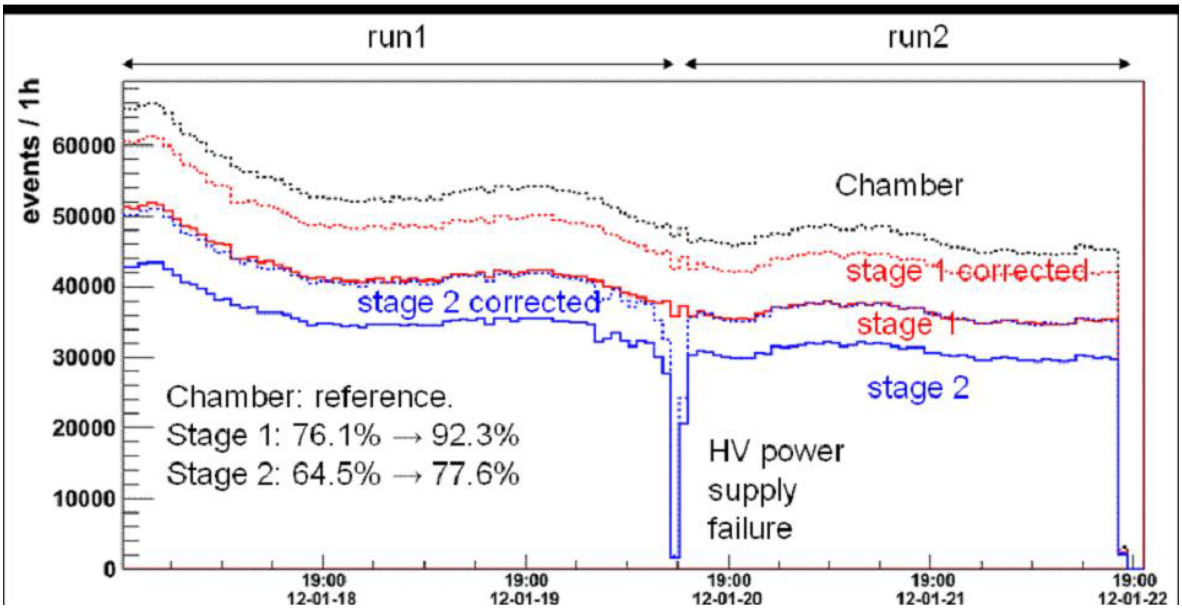

Figure 64: Chamber event count rate as a function of time for the main trigger (dashed black) and for both stages in red and blue. The dashed line plots are corrected rates for both stages.

The rate observed in different stages is important in the case of chamber event, because the chambers can provide direction of the event. Figure 64 shows the variation of the raw and corrected event count rate for different stages using the lowest threshold applied to the pulse. The pattern does not change from stage to stage. The corrected rate is higher than the one obtained with the scintillator, because the previous correction was very rough and not reach the 100% efficiency of the scintillators.

Since the rate in the chamber is biased due to the applied threshold (low avalanche gain), the pressure correction is applied to the scintillator count rate only. Figure 65 shows a comparison between the event count rate, pressure and temperature. Note that these atmospheric parameters have been taken at the airport, few kilometres from Carleton University.

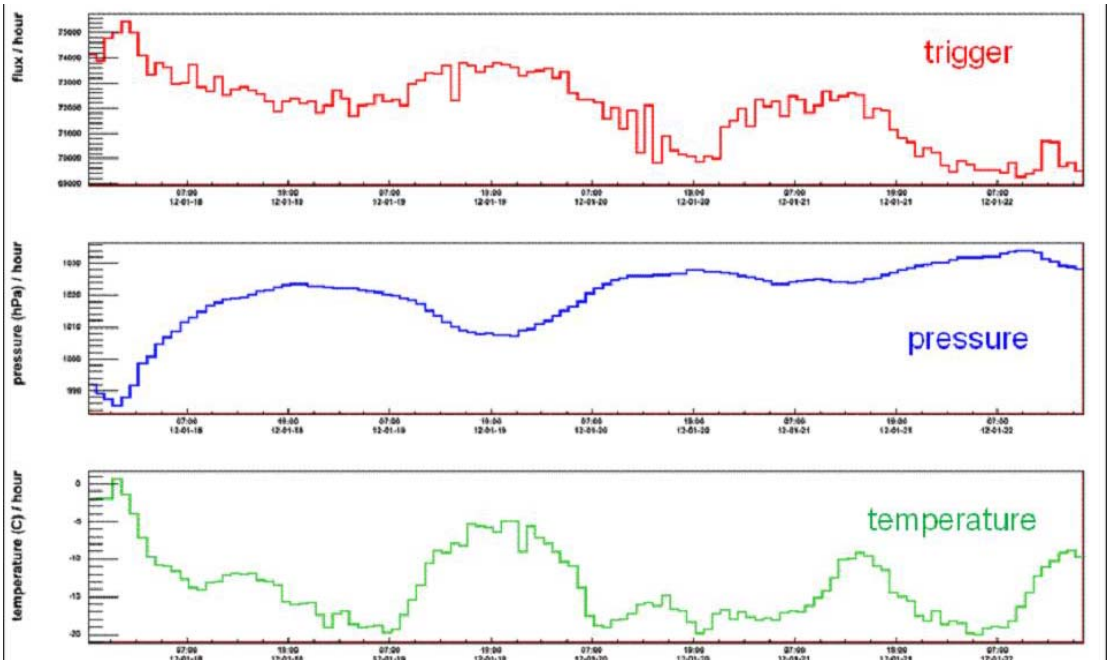

Figure 65: Comparison between the event count rate in the scintillator and the pressure / temperature..

A different way to do a comparison is to plot $100 \cdot Log(X / X_0)$ as shown in Fig. 66, with X is the count rate, pressure or temperature per time bin and $X0$ is the mean value.

From both plots, it is clear that the count rate is anti-correlated to the pressure and correlated to the temperature. Figure 67 shows the correlation before and after correction. The pressure has more effect on the count rate than the temperature for this data set. The correlation drops from -0.85 to -0.02.

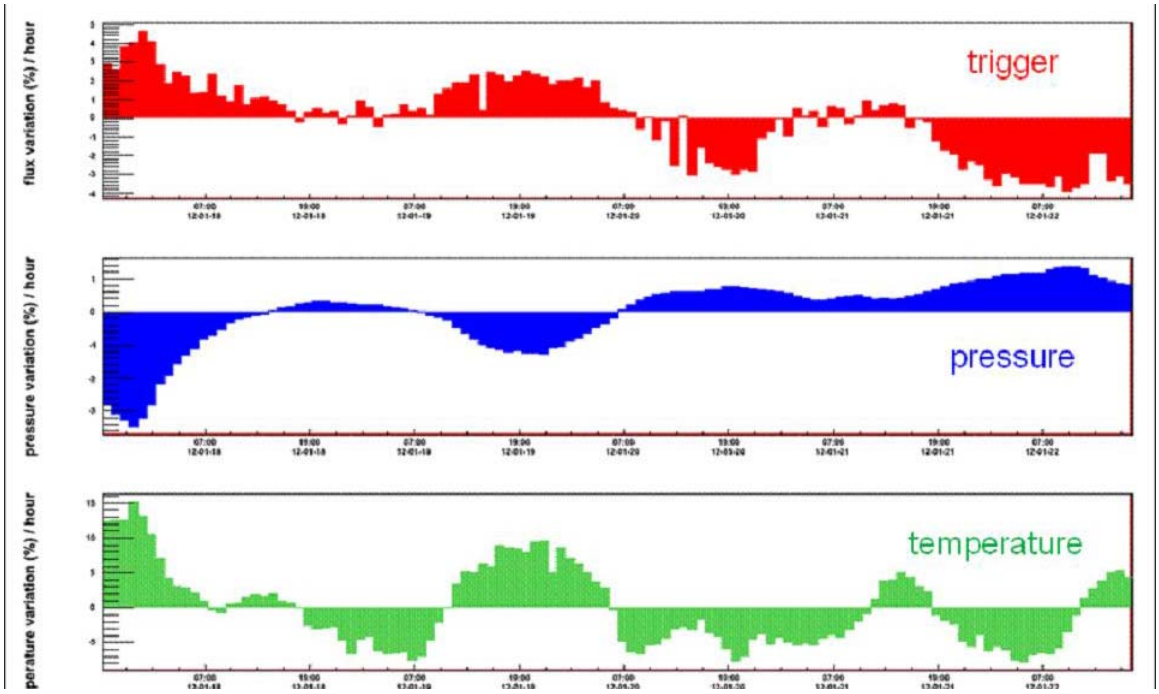

Figure 66: Comparison between the relative variation of the event count rate in the scintillator and the pressure / temperature.

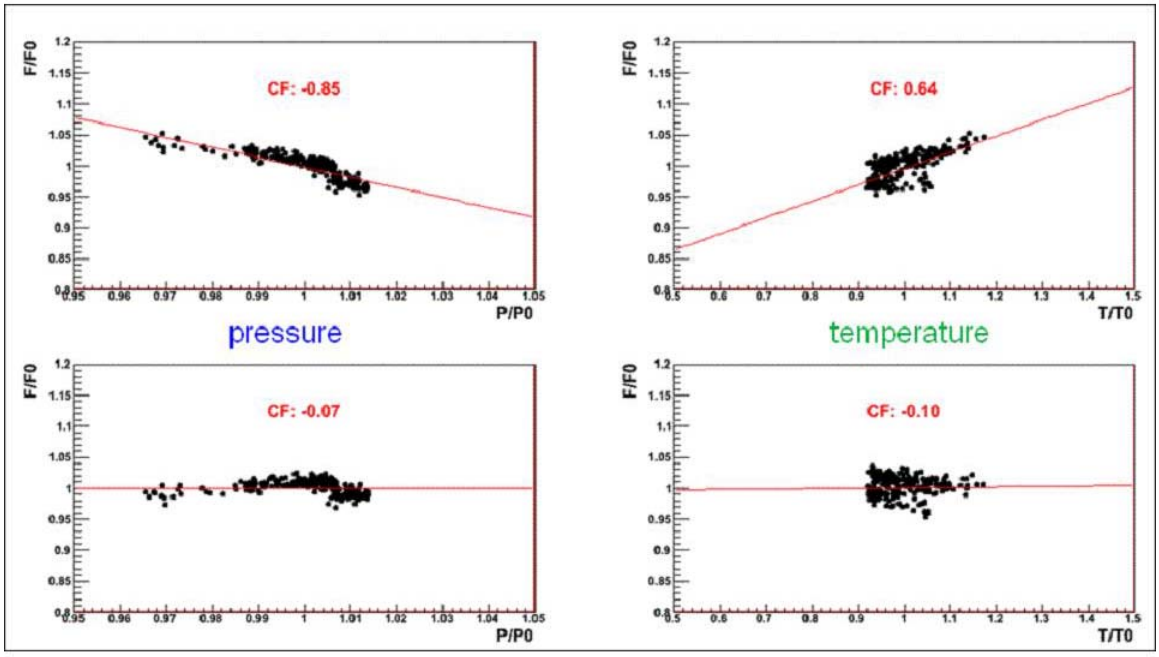

Figure 67: Scintillator relative count rate as a function of the relative pressure and temperature, before and after correction. CF is the correlation factor.

The remaining effect on the count rate from the pressure and temperature is shown in Fig. 68. The event count rate is better corrected with the pressure rather than temperature.

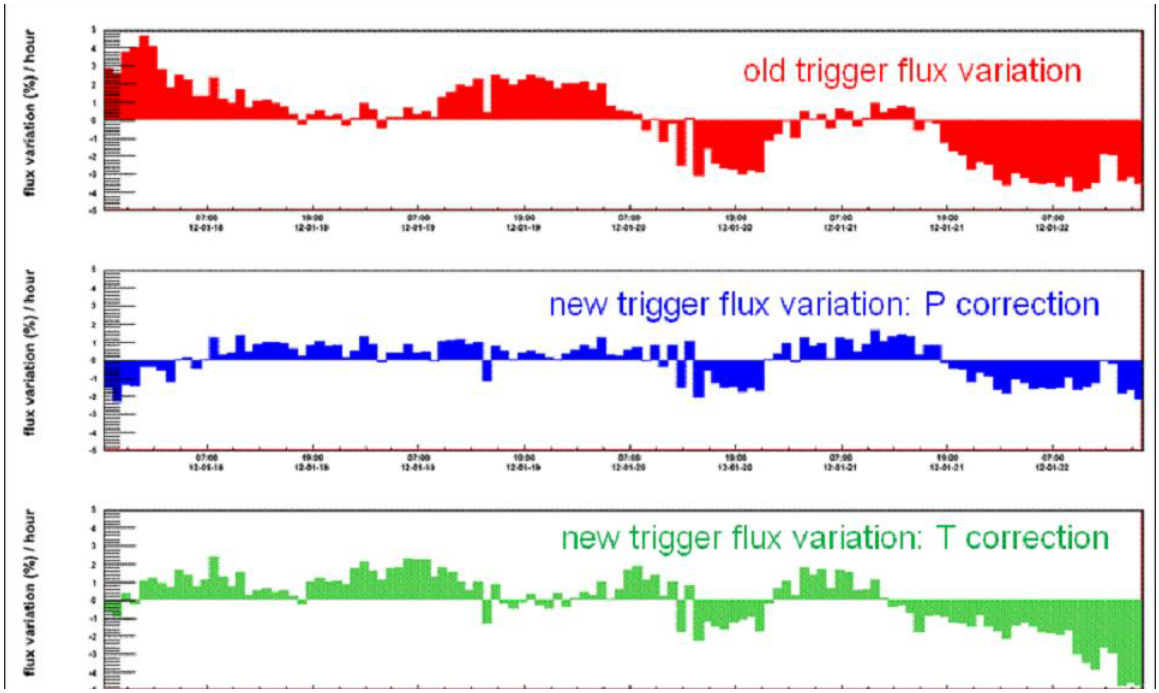

Figure 68: Relative variation in the event count rate before and after pressure and temperature correction.

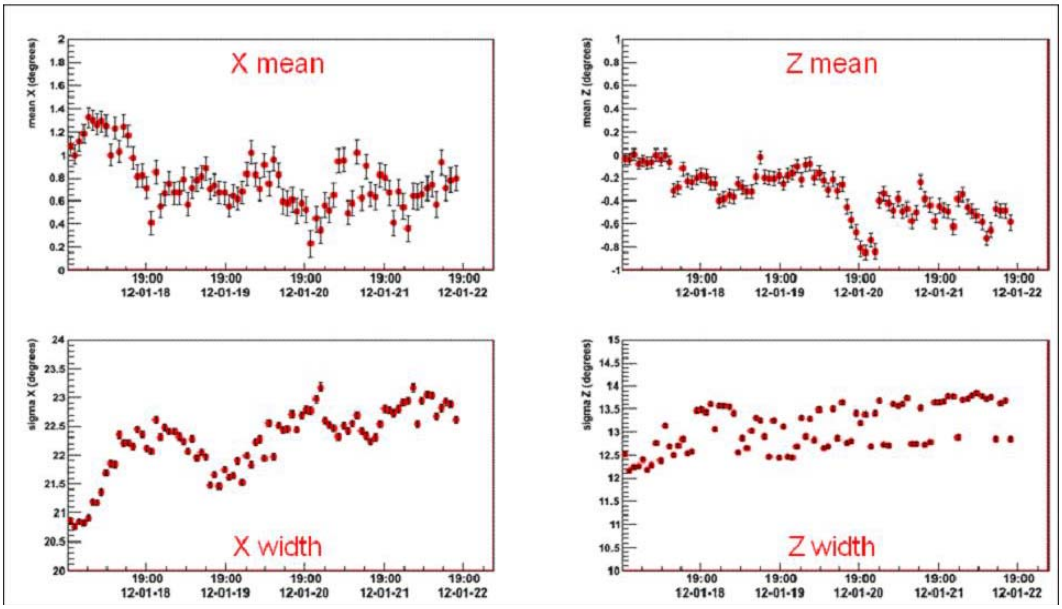

Figure 69: Variations of the mean and the width of the angular distribution versus time for both directions obtained with the drift chambers.

Variations of the mean and the width of the angular distributions in both directions X and Z obtained in stage-1 correspond to 99.5% of muons according to Monte-Carlo, as demonstrated in Fig. 69. The mean for X direction seems to show a periodical variation with a minimum around 8PM and a maximum around 8AM. The X width increases with time and seems to show a periodical variation as well with smaller amplitudes versus time. In Z direction, the shape is not very clear. It does not show an obvious behaviour. It could a better spatial resolution in X direction.

6.4.4 Conclusions

A small scale tracking system has been tested at Carleton to monitor cosmic ray muons. The muon flux rate found is anti-correlated to the atmospheric pressure. This dependence has been corrected easily. The change of the flux due to temperature variation in the atmosphere has not been corrected because of the missing information about the expansion of the atmosphere. This set-up is not ideal to predict the arrival of CME to the earth's atmosphere, but it is a good tool to show the ability of the collaboration to monitor cosmic rays. The advantages of a large detector are listed below.

The design criteria of the future FOREWARN detector are:

- Size is 5m x 5m = 25m^2 , which will provide 9 x 106 counts per hr.
- Angular resolution is approximately ±10^o, i.e. ~ 175 mr.
- Plane separation is about 1.0 m.
- Spatial resolution about 17 cm

The characteristics for each detector (their assembly is shown in Fig. 70) are as follows:

Scintillator strips are 2.5m long, 16cm wide
Angular resolution is approximately ± 9 degrees
Angular coverage 78 degrees
64 channels per layer
Two x,y layers - 256 channels
4 x 64 channel PMTs

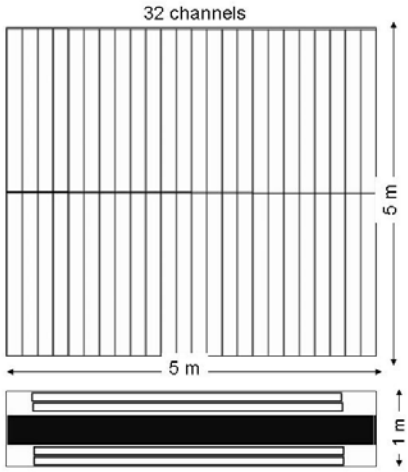

Figure 70: Detector geometry.

The design is proposed for a robust, turnkey CR detector which has the following demanding features:

- Size larger than existing detectors (can be scaled down if necessary)
- Modular construction – easy to access for installation and maintenance
- Simple electronics
- Needed addition to the Global Muon Network

6.5 Proposed detector of new type

There are many applications where a large area detector is required. In ground-based cosmic ray studies large area (5m x 5m) arrays are required to provide sufficient statistics, within a short data taking period of an hour or so, given the fairly low cosmic ray muon rate of 1 per sq. m. per second. In designing detectors to cover this area, one can either set the detector dimensions equal to the array dimensions, or construct many smaller devices and locate them adjacent to each other. In the former arrangement, the challenge is working with large heavy objects that are fairly delicate – either plastic scintillator or large area drift chambers. These require special lifting techniques and many precautions to avoid damage to the sensitive equipment. The other approach is to make many smaller units, which are easier to work with and defective units can be easily replaced. The challenge then, is to provide a calibration method, so that each detector's response can be tracked and balanced with neighbouring detectors to provide an overall uniform response.

This Part follows the second approach, and describes a small unit detector, 2 feet by 2 feet, which can be mass produced to form the basis of a much larger detector. This document describes the base unit, describes noise mitigation techniques, and discusses calibration techniques which will allow a large detector made up of many such units, to perform with a uniform response [98: Armitage, 2011].

6.5.1 Physical Dimensions

In pursuing the idea of using many smaller detector units and assembling them next to each other to cover a large area, one has to minimize the cost per unit otherwise the total cost will be prohibitive. For any detector, a large proportion of the cost is in the electronics used to read it out, therefore the DAQ needs to be kept simple. The tile detector achieves this as it does not require a flash ADC or sensitive TDC's, it only requires a discriminator and pattern unit bit, to record which channel has 'fired'. There is no attempt made to interpolate the position measurement within the boundaries of the unit detector.

While this keeps the electronics simple, the size of the unit detector then determines the granularity – the spatial and angular resolution. Looking at other detectors comprising the Global Muon detector Network, there are 6 muon super-detectors each covering an area of ≥ 9 m^2:

Muon Telescopes in
Nagoya, São Martinho, Hobart;

Muon Hodoscopes in
Kuwait, MEPhI-URAGAN ,
GRAPES-III (Ooty, 560 m2).

The typical angular resolution of these detectors is ± 10 degrees or ± 175 milliradians (mr). In order to match this specification, a 1 foot (30.5cm) square unit would need to be placed 2m above a similar sized unit. With this as a base, such four units (tiles) can then be packed together making a 2 foot by 2 foot (61cm x 61cm) unit, see Fig. 71.

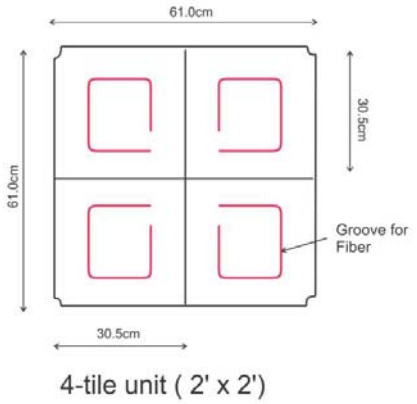

Figure 71: A unit composed of four tiles.

6.5.2 The Readout Fiber

Provision is made for the readout fiber to be located in a groove machined into the top face of the scintillator tile. The tile itself can be 5cm thick, and a groove of 2mm depth by 2mm width, is machined into the upper surface. The wavelength shifting (WLS) fibre (manufactured by the KURARAY company) has an outer dimension of 1.2mm and can be glued into the groove using an optical epoxy. The fiber loops around the tile being located 7.5cm from each edge of the tile. Both ends of the fiber are brought out of the tile and are connected to a photomultiplier. From each scintillator, 2 ends of the same fibre are brought out, so from the 2 feet by 2 feet unit, containing four tiles, 8 data channels need to be accommodated.

6.5.3 The Calibration Fiber

A system of LED Flashers is proposed to provide a continuous calibration and monitoring of the gains of the tile/WLS/photomultiplier. Each tile has provision for a plastic optical fiber (p.o.f.) glued into grooves and pointing towards the far corner of the tile. The LED's can be flashed under computer control and the detection of the light provides a good check of all the detector subsystems.

6.5.4 Support of the Detector

The installation is planned to make use of existing, commercially available flooring systems – in particular the raised floor systems used to accommodate computer networking cables (Fig. 72). The tile detectors can be placed on the sub-floor and the fibres brought out through a hole or slot cut into the removable flooring tiles. The size 2 feet by 2 feet was chosen to match the dimensions of typical raised floor systems.

Figure 72: A typical raised floor system.

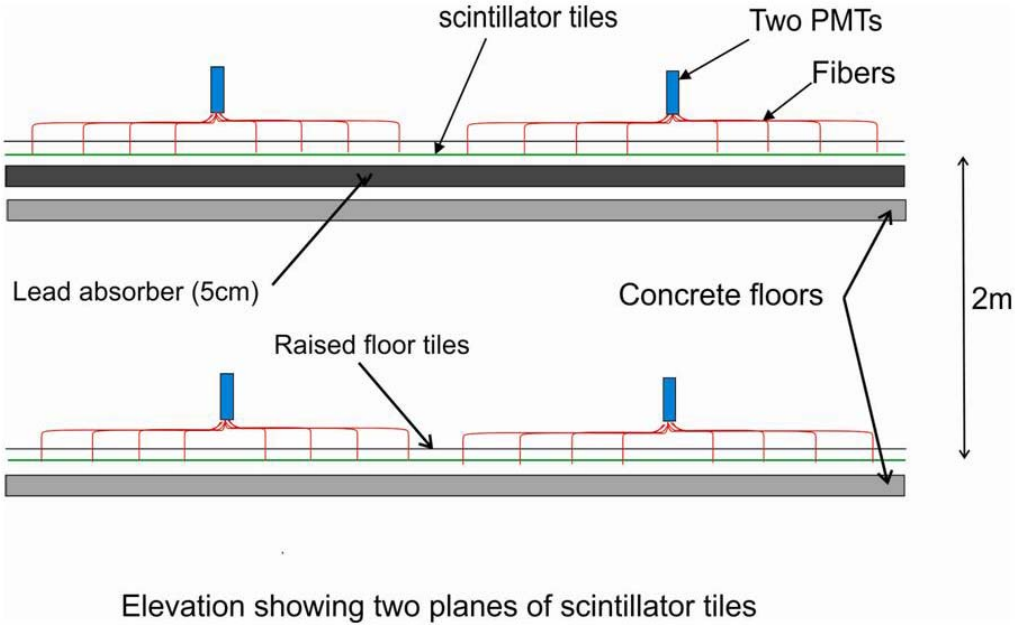

Figure 73: Elevation view of the assembled detector

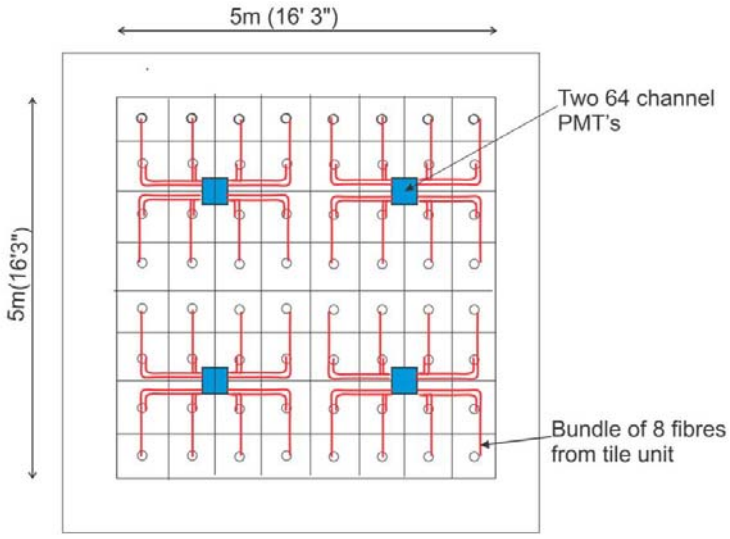

Figure 74: Schematic view of the routing of the readout fibres.

An elevation view is shown in Fig. 73. The electronics and photomultiplier systems can be located and supported on the raised floor system with four central locations providing the resources for a large area of detectors (Fig. 74).

6.5.5 Electronics

The DAQ can be kept simple so as to keep the overall costs within reasonable limits. The readout is essentially a discriminator and coincidence unit, whose output is then latched into a pattern unit when a cosmic ray muon passes through both layers of the detector (Fig. 75). The amplifier/ shaper is used to provide amplitude correction to individual channels based on data from the calibration system.

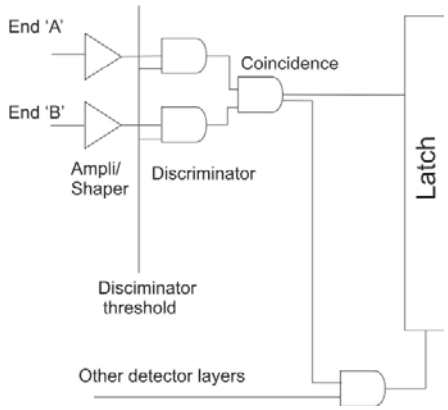

Figure 75: Schematic diagram of detector DAQ.

The coincidence between end 'A' of the fiber and end 'B', provides a method of noise reduction. The individual PMT channels have a large amount of noise inherent in them, and a coincidence at this stage removes most of this.

6.5.6 Response of the Detector

The response has been modelled with GEANT4 (Fig. 76), the obtained angular distribution is shown in Fig. 77.

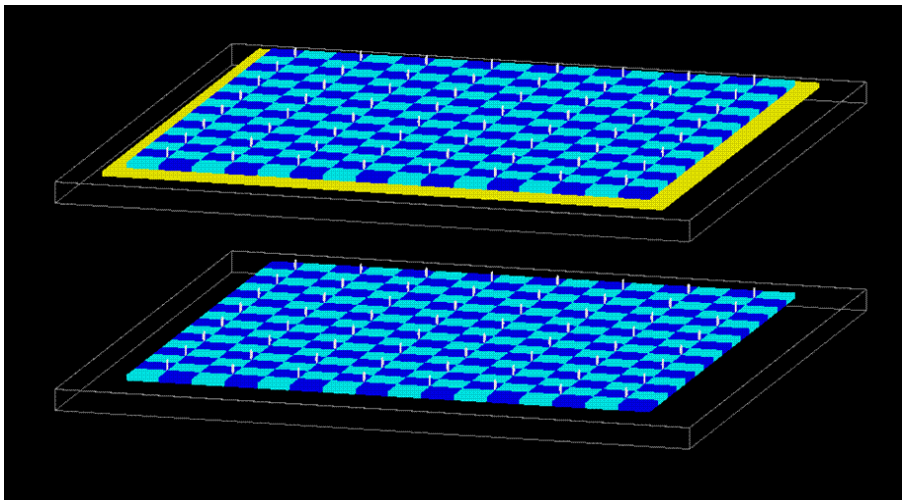

Figure 76: A model of the detector for Geant4: note that light blue and dark blue are used to differentiate between adjacent tiles, yellow is the lead sheet.

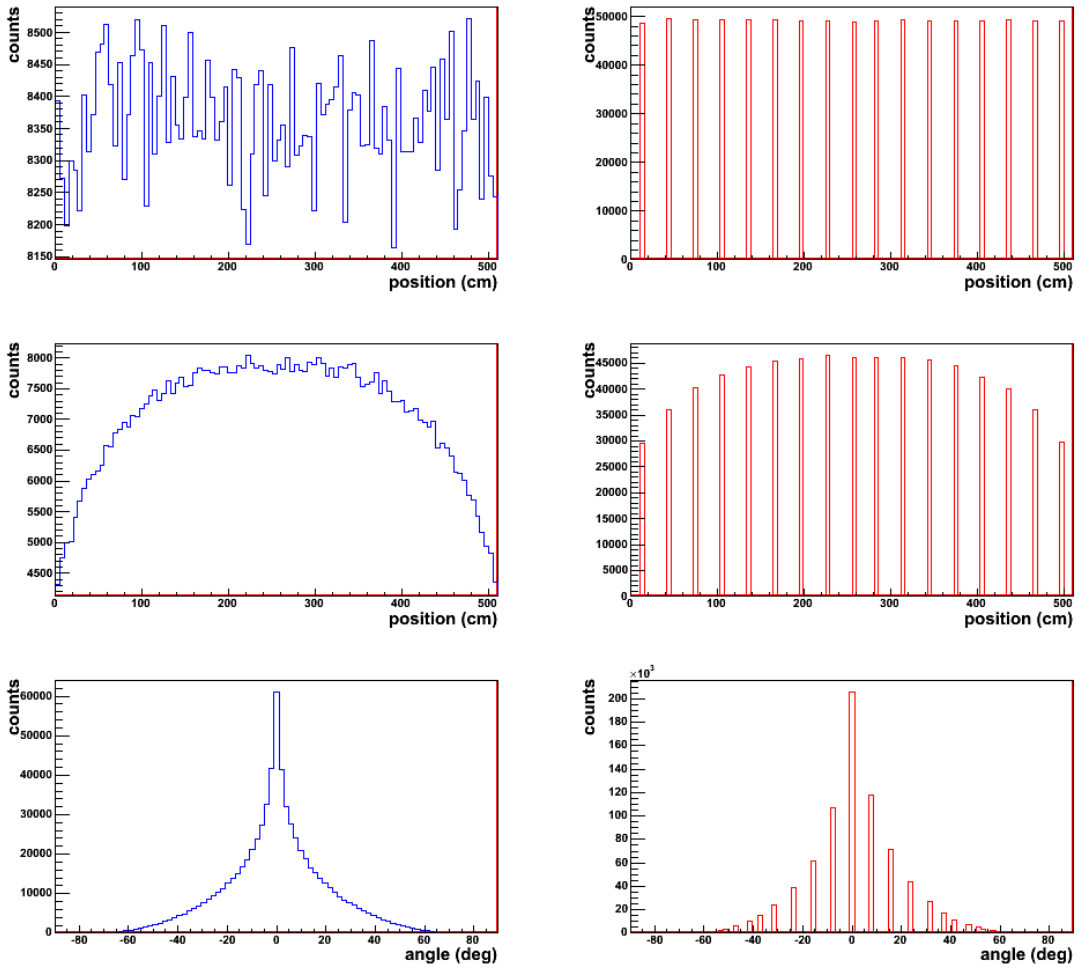

Figure 77: Geant4 generated events – continuous distributions on the left hand side, right hand side shows the effects of detector granularity (16 tiles across the detector).

Uniform distributions in the upper plots, the middle plot shows the spatial distribution resulting from a $\cos^2 \theta$ angular distribution and the lower plot gives the angular coverage, showing the effect of requiring the track to pass through both the upper and lower layer.

7 General conclusions (capability roadmap)

The impacts of space weather storms on electric power grids can result in the widespread and sustained power grid damage. The most severe case known so far is the Hydro Quebec blackout in 1989. The report prepared by National Science Foundation USA in 2008 has pointed out that the impacts can be more severe now, when power grids are more heavily loaded and interconnected.

The space weather events resulting from solar eruptions produce geomagnetic storms which drive geomagnetically induced currents in high voltage transmission lines. These may cause severe damage to critical components of the electrical power grid. Canada is more exposed to the space weather effects than US due to its northern geographic location.

The extreme space weather events are driven by coronal mass ejections (CME) and are often preceded by interplanetary shocks (IP). In turn, these are typically accompanied by strong enhancements of the cosmic rays anisotropy. Such anisotropies represent a key mechanism by which information about the presence of a severe disturbance can be transmitted to remote locations, including upstream of the shock. Since CRs are fast and have large scattering mean free paths (~ 1 AU) in the solar wind, this information travels rapidly and may prove useful for space weather forecasting. Muons being high energy particles and easy to be detected with high accuracy and low noise are more preferable than other particles to provide the advanced warning of approaching solar disturbance.

The aim of this feasibility study was to understand the physical mechanisms of the cosmic rays precursors and to build the prototype muon detector. Thus, it has been divided into theoretical (knowledge development) and experimental (technology development) parts. The theoretical part has been done by researchers at Natural Resources Canada (the Lead Department) and experimental part by Carleton University, Physics Department (the Contractor).

Conclusions from the theoretical part are as follows:

1. Review of the literature shows that in many cases the precursors of the strong disturbance can be identified in post-analysis.

2. More reliable precursor is the Loss-Cone (LC) precursor which is associated with the deficit of the flux (Forbush decrease) in the disturbed interplanetary medium.

3. An analysis of muon data for one of the storms shows a possibility of observing LC precursor up to 25 hours in advance.

4. In order to build a physical model of propagation and modulation of CRs, in particular the Forbush Decrease, one should solve the CR transport equation.

The most challenging task was to define the not known diffusion term in the CR Transport equation, which has been obtained during the execution of the project. An evaluation of a diffusion model for the cosmic ray transport has showed that

- During large FD events the diffusion approximation in high-energy limit is valid for CRs of ~ 50 GeV and higher energy.

- The derived diffusion coefficient can be used in numerical modeling for estimations of terms in the transport equation and to find a relation between FD amplitude and parameters of solar wind and IMF.

- A similar approach can be applied to the neutron component but with a different expression for the diffusion coefficient.

Roadmap step:
The next level in knowledge advancing is to solve the CR transport equation based on the results of the analysis of the diffusion process performed in this report.

In order to gain more predictive power we need to monitor the propagation of solar disturbance between the Sun and the Earth and the way to do this is to monitor the Galactic Cosmic Ray flux using ground based muon detectors.

The Canadian Muon Workshop has shown that the Global Muon Detector Network (GMDN) performs this function around the globe successfully, but there are gaps in the viewing directions which the GMDN is not monitoring and one of them is located in North America.

It has been concluded that placing an additional muon detector at Eastern Canada, Western Canada or Canadian North will give same important and essential addition to provide complete coverage of the whole sky and therefore to provide the complete advanced information on approaching solar disturbance. Thus, a presence of a proposed muon telescope in Ottawa would be of great importance to provide critically needed coverage for a study of CR modulation phenomena observed with GMDN.

Therefore, **the important part of project was to create a prototype muon telescope in Canada**, which has been done by the team at Physics Department, Carleton University.

During the course of project, the prototype gas-filled muon detector has been designed, assembled and data were recorded.

The methodologies of removing the effects of non-solar modulations (atmospheric pressure and temperature) on the data obtained by this prototype telescope were investigated and applied which has been done successfully showing good results.

In addition to the developed prototype gas filled detector, the new tiled detector has been proposed and its design specifications have been provided.

Roadmap step:
The next level in technology advancing is to actually **build the operational muon telescope of the designed size.**

Thus, summarising the results of the work in brief, the following can be pointed out.

1. Today there have been developed a methodology to use muon detectors for space weather forecasting. These methods should be further developed for operational use and Canadian researchers could contribute to solving this global problem of high importance.

2. A study of the prototype muon detector at Carleton University confirmed that ground-based muon telescopes can provide a permanent monitoring of CR intensity.

3. To make accurate analysis of muon data one needs to provide full sky coverage which can be done by adding in a muon detector located in Ottawa and participating in the International Muon Detector Network including the GMDN.

Thus a development of experimental techniques for ground-based measurements of cosmic-ray-produced muons and methods for analysis of muon data could allow us to use muon observations in combination with other tools for space weather forecasting in order to obtain timely warning of extreme space weather conditions and improve the protection of Canadian critical infrastructure from large solar disturbances.

References

[1] The Canadian Space Weather Forecast Centre (CSWFC), website: http://www.spaceweather.gc.ca/tech/se-eng.php .

[2] L. Trichtchenko, D. Boteler, G. Kalugin, J. Armitage, K. Boudjemline, and D. Waller (2012) *Extreme Space Weather Study,* Oral presentation in Public Security S&T Summer Symposium 2012, Ottawa, Ontario, Canada, 11-14 June 2012.

[3] G. Kalugin, L. Trichtchenko, K. Boudjemline, J. Armitage, and D. Waller (2013) *Space weather events with ground-based muon observations (state-of-the-art)*, Geological Survey of Canada, Open File 7285, 158 p., doi: 10.4095/292231.

[4] L. Trichtchenko, D. Boteler, G. Kalugin, K. Boudjemline, J. Armitage, and D. Waller (2011) *Early Warning of the Extreme Space Weather Events. Feasibility Study*, Talk on Energy and Utilities Sector Network Meeting: National Strategy for Critical Infrastructure Protection, Government Conference Centre, Ottawa, Ontario, Canada, November 16, 2011.

[5] L. Bolduc and J. Aubin (1978) *Effects of direct currents in power transformers, Part I: A general theoretical approach*, Electr. Power Syst. Res., 1, pp. 291-298.

[6] NPCC (2000) The Northeast Power Coordinating Council Procedures for Solar Magnetic Disturbance which affect Electric Power Systems, Document C-15, Nov 7, 2000.

[7] T.S. Molinsky (2002) *Why utilities respect geomagnetically induced currents*, JASTP, 64, pp. 1765-1778.

[8] NERC (2012) North American Electric Reliability Corporation special reliability assessment: *Effects of Geomagnetic Disturbances on the Bulk Power System*, Interim Report, February 2012.

[9] B. Rossi, *Cosmic Rays*, New York, McGraw-Hill, 1964, p. 55.

[10] J.E. Humble, M.A. Shea, and D.F. Smart (1985) *Sensitivity of cosmic ray trajectory calculations to geomagnetic field model representations*, Phys. Earth Planet. Inter., 37, pp. 12-19.

[11] C. Plainaki, H. Mavromichalaki, A. Belov, E. Eroshenko, and V. Yanke (2009) *Neutron monitor asymptotic directions of viewing during the event of 13 December 2006*, Advances in Space Research 43, pp. 518-522.

[12] M.L. Duldig (2001) *Australian Cosmic Ray Modulation Research*, Publications of The Astronomical Society of Australia, 18, pp.12-40 (DOI: 10.1071/AS01003, arXiv:astro-ph/0010147v1).

[13] S.E. Forbush (1938) *On world-wide changes in cosmic-ray intensity,* Phys. Rev.*,* 54(12)*,* pp. 975-988.

[14] S. E. Forbush (1946) *Three unusual cosmic-ray increases possibly due to charged particles from the Sun*, Phys. Rev., 70, pp.771-772.

[15] S.E. Forbush, T.D. Stinchcomb, and M. Schein (1950) *The extraordinary increase of cosmic-ray intensity on November 19, 1949*, Phys. Rev., 79, pp.501-504.

[16] S.E. Forbush (1958) *Cosmic-ray intensity variations during two solar cycles,* JGR, 63(4), pp.651-669.

[17] K. Leerungnavarat, D. Ruffolo, and J.W. Bieber (2003), *Loss cone precursors to Forbush decreases and advance warning of space weather effects*, Astrophys. J., 593, pp. 587–596.

[18] K. Munakata, J.W. Bieber and S. Yasue, *et al.* (2000) *Precursors of geomagnetic storms observed by the muon detector network*, J. Geophys. Res., 105**,** pp. 27,457–27,468.

[19] A. Asipenka, A. Belov, E. Eroshenko, H. Mavromichalaki, M. Papailiou, A. Papaioannou, V. Oleneva, and V. Yanke (2009) *Asymptotic longitudinal distribution of cosmic ray variations in real time as the method of interplanetary space diagnostic*, Proceedings of the 31st ICRC, Lodz, 4 pp.

[20] D. Ruffolo, J.W. Bieber, P. Evenson, and R. Pyle (1999) *Precursors to Forbush Decreases and Space Weather Prediction*, Proc. 26th Int. Cosmic Ray Conf., Vol. 6, Salt Lake City, Utah, USA, August 17-25, 1999, pp.440-443.

[21] A.V. Belov, J.W. Bieber, E.A. Eroshenko, P. Evenson, R. Pyle, and V. Yanke (2001) *Pitch-angle features in cosmic rays in advance of severe magnetic storms: Neutron monitor observations*, Proc. 27th Int. Cosmic-Ray Conf., Hamburg, Germany, Vol. 9, pp. 3507–3510.

[22] J.R. Jokipii (1966) *Cosmic-Ray Propagation. I. Charged Particles in a Random Magnetic Field*, Astrophysical Journal, Vol. 146, pp. 480-487.

[23] M. Rockenbach et al. (2009) *Global Muon Detector Network Observing Geomagnetic Storm's Precursor Since March 2001*, Proc. 31st Int. Cosmic Ray Conf., Łódź, Poland, July 7-15, 2009, 4 pp.

[24] M. Rockenbach, et al. (2011) *Geomagnetic storm's precursors observed from 2001 to 2007 with the Global Muon Detector Network (GMDN)*, Geophysical Research Letters, 38, L16108, 4 pp., doi:10.1029/2011GL048556.

[25] L. Trichtchenko and G. Kalugin (2011) *Efficacy of Muon Detection for Solar Flare Early Warning*, Talk on Canadian Muon Workshop, St-Émile-de-Suffolk, Québec, Canada, October 17-19, 2011.

[26] A. Fushishita, et al. (2010) *Precursors of the Forbush decrease on 2006 December 14 observed with the global muon detector network (GMDN)*, The Astrophysical Journal, 715, pp. 1239–1247, doi:10.1088/0004-637X/715/2/1239.

[27] Y. Okazaki, et al. (2008) *Drift Effects and the Cosmic Ray Density Gradient in a Solar Rotation Period: First Observation with the Global Muon Detector Network (GMDN),* The Astrophysical Journal, 681, pp. 693–707.

[28] T. Kuwabara, et al. (2004) *Geometry of an interplanetary CME on October 29, 2003 deduced from cosmic rays*, Geophysical Research Letters 31 (19) L19803, 5 pp.

[29] K. Munakata et al. (2005) *A "lose cone" precursor of an approaching shock observed by a cosmic ray muon hodoscope on October 28, 2003*, Geophys. Res. Lett.,32, L03S04, 4 pp.

[30] T. Nonaka et al. (2003) *Study of Cosmic Ray Short Term Variations Using GRAPES-3 Muon Telescopes*, Proc. 28th Int. Cosmic Ray Conf., July 31- August 7, 2003, Tsukuba, Japan, v6, pp. 3569-3572.

[31] N.J. Schuch, A. Dal Lago, M. Rockenbach et al. (2009) *Proposal for a solar heliosphere 3-D visualization with accurate space weather forecasting combining the observations NASA's Stereo Mission and the Global Muon Detector Network-GMDN*, XXVII IAU General Assembly – JD16 – IHY Global Campaign – Whole Heliosphere Interval, August 3-14, 2009, Rio de Janeiro, Brazil.

[32] F. Jansen, K.Munakata , M.L. Duldig, and R. Hippler (2001) *Muon Detectors – the real-time, ground based forecast of geomagnetic storms in Europe,* ESA Space Weather Workshop: Looking towards a European Space Weather Programme, 2001, ESA WPP-144, 6 pp.

[33] T. Nonaka et al. (2005b) *Short Term Variations of Galactic Cosmic Rays Observed with GRAPES-3 Muon Telescopes*, 29th Int. Cosmic Ray Conf., August 3 - 10, 2005, Pune, India, SH 2.6, pp. 359-362.

[34] J.W. Bieber and P. Evenson (1998) *CME Geometry in Relation to Cosmic Ray Anisotropy*, Geophys. Res. Lett., Vol. 25, No. 15, pp. 2955-2958.

[35] T. Kuwabara, et al. (2009) *Determination of interplanetary coronal mass ejection geometry and orientation from ground-based observations of galactic cosmic rays*, J. Geophys. Res., Vol. 114, A05109, doi:10.1029/2008JA013717, 10 pp.

[36] I. Petukhov and S. Petukhov (2009) *The method of particle trajectories for description of a cosmic ray*, Proc. 31st Int. Cosmic Ray Conf., Łódź, Poland, July 7-15, 2009, 4 pp.

[37] H.S. Hudson, J.-L. Bougeret, and J. Burkepile (2006) *Coronal Mass Ejections: Overview of Observations*,

[38] C. Shen, Y. Wang, P. Ye, X.P. Zhao, B. Gui, and S. Wang (2007) *Strength of coronal mass ejection-driven shocks near the Sun and their importance in predicting solar energetic particle events*, The Astrophysical Journal, 670, pp.849-856.

[39] L. Burlaga, E. Sittler, F. Mariani, and R. Schwenn (1981) *Magnetic Loop Behind an Interplanetary Shock: Voyager, Helios, and IMP 8 Observations*, JGR, 86, A8, pp.6673-6684.

[40] E.N. Parker (1965) *The passage of energetic charged particles through interplanetary space*, Planet. Space Sci., 13, pp.9-49.

[41] L.I. Dorman and M.E. Katz (1977) *Cosmic ray kinetics in space*, Space Science Reviews, 20(5), pp.529-575.

[42] J.R. Jokipii, E. H. Levy and W. B. Hubbard (1977), *Effects of particle drift on cosmic-ray transport. I. General properties, application to solar modulation*, Astrophys. J., 213, 861–868.

[43] Z. Fujii (2011) Nagoya Multi-Directional Muon Telescope, Cosmic-Ray Research Section, Solar-Terrestrial Environment Laboratory, Nagoya University, Nagoya, 464-8601 Japan, http://www.stelab.nagoya-u.ac.jp/ste-www1/div3/muon/dbtext22.pdf (Revised on Feb 23, 2011), 14 pp.

[44] G. Kalugin (2012) *Using ground-based muon measurements for forecasting extreme space weather events*, Oral presentation in Space Weather Group Meeting, Canadian Space Weather Forecast Centre (NRCan), Ottawa, Ontario, Canada, 9 March, 2012.

[45] NASA, http://solarscience.msfc.nasa.gov/SunspotCycle. shtml

[46] G. Kalugin, L. Trichtchenko, J. Armitage, K. Boudjemline, and D. Waller (2012) *A study of Forbush decrease events with ground-based muon observations*, Poster presentation in 23rd European Cosmic ray Symposium, Moscow State University, Moscow, Russia, 3-7 July, 2012 and in 9th Canadian Solar Workshop, St-Émile-de-Suffolk, Québec, Canada, October 12-15, 2012.

[47] G. Kalugin and L. Trichtchenko (2012) *Combining Muon Detector Measurements with ACE Level 2 Data for Space Weather Forecasting*, Oral presentations, FOREWARN Collaboration Meetings, Carleton University, Ottawa, Ontario, Canada, 15 February 2012 and 28 May, 2012.

[48] J.R. Jokipii and P.J. Coleman (1968) *Cosmic-Ray Diffusion tensor and Its Variation Observed with Mariner 4*, JGR, Space Phusics, 73(17), pp. 5495-5503.

[49] J.R. Jokipii (1967) *Cosmic-ray propagation, 2. Diffusion in the interplanetary magnetic field*, Astrophysical Journal, 149, 405-415.

[50] J.J. Quenby, T. Mulligan, J.B. Blake, and D.N.A. Shaul (2013) *Diffusion Coefficients, Short Term Cosmic Ray Modulation and Convected Magnetic Structures*, Advances in Astronomy, ID 429303, 10pp.

[51] A.J. Klimas and G. Sandri (1971) *Foundation of the theory of cosmic-ray transport in random magnetic fields*, The Astrophysical Journal, 169, pp. 41-56.

[52] A.J. Klimas and G. Sandri (1973) *The parallel diffusion of cosmic rays in a random magnetic field*, The Astrophysical Journal, 184, pp. 955-965.

[53] L.A. Fisk, M.L. Goldstein, A.J. Klimas, and G. Sandri (1974) *The Fokker-Planck coefficient for pitch-angle scattering of cosmic rays*, The Astrophysical Journal, 190, pp.417-428.

[54] J.R. Jokipii (1971) *Propagation of Cosmic Rays in the Solar Wind*, Review of Geophysics and Space Physics, 9(1), pp.27-87.

[55] H.J. Völk, (1975) *Cosmic Ray Propagation in Interplanetary Space*, Review of Geophysics and Space Physics, 13(4), pp.547-566.

[56] M. Kachelrieß (2007) *Lecture Notes on High Energy Cosmic Rays*, 17th Jyväsklyä Summer School, Norway, August, 2007.

[57] I.H. Urch (1977) *Charged Particle Diffusion in a Turbulent Magnetic Field*, Astrophysics and Space Science, 48(1), pp.231-236.

[58] F. Harris (1999) *Spectral Analysis Windowing*, In: Wiley Encyclopedia of Electrical and Electronics Engineering, Ed. by J. Webster, Wiley, p.88-105.

[59] S. Haykin and K.J.R. Liu (2009) *Handbook on Array Processing and Sensor Network*, Wiley, p.378.

[60] S. Stergiopoulos (2009) *Advanced Signal Processing: Theory and Implementation for Sonar, Radar, and Non-Invasive Medical Diagnostic Systems*, Ed. by S. Stergiopoulos, 2nd ed., CRC Press, p.469.

[61] B. Boashash (2003) *Time-Frequency Signal Analysis and Processing. A Comprehensive Reference*, Ed. by B. Boashash, Elsevier, p.18.

[62] D. Hale (2006) *An efficient method for computing local cross-correlations of multi-dimensional signals, Center for Wave Phenomena, Consortium Project on Seismic Inverse methods for Complex Structures*, Golden, Colorado, CWP-544, May 15-18, 2006, p.253-260.

[63] R.L. Allen and D.W. Mills (2004) *Signal Analysis: Time, Frequency, Scale, and Structure*, IEEE, Wiley, p.714.

[64] L.T. Ikelle and L. Amundsen (2005) *Introduction to Petroleum Seismology*, In: Investigations in Geophysics, No. 12, Society of Exploration Geophysicists, pp.166-169.

[65] Kalugin, G. and Trichtchenko, L. (2013) *Frequency parameters of the interplanetary magnetic field during large Forbush decrease events*, Oral presentation in DASP 2013, Kingston, Ontario, Canada, February 18-19, 2013.

[66] U.W. Langner and M.S. Potgieter (2005) *Modulation of galactic protons in an asymmetrical heliosphere*, The Astrophysical Journal, 630, pp. 1114-1124.

[67] K.G. McCracken, U.R. Rao, and M.A. Shea (1962) *The Trajectories of Cosmic Rays in a High Degree Simulation of the Geomagnetic Field*, Technical Report 77, Massachusetts Institute of Technology, Laboratory for Nuclear Science, MIT Press, Cambridge.

[68] K.G. McCracken, U.R. Rao, B.C. Fowler, M.A. Shea, and D.F. Smart (1968) *Cosmic Ray Tables (Asymptotic Directions, etc.)*, Annals of the IQSY, 1, Ch. 14, pp. 198-214, MIT Press, Cambridge.

[69] M.A. Shea, D.F. Smart, and K.G. McCracken (1965) A Study of Vertical Cutoff Rigidities Using Sixth Degree Simulations of the Geomagnetic Field, J. Geophys. Res., 70, pp. 4117-4130.

[70] D.F. Smart, M.A. Shea, and E.O. Flückiger (2000) *Magnetospheric Models and Trajectories Calculations*, Space Science Rev., 93, pp. 281-308.

[71] D.J. Cooke, J.E. Humble, M.A. Shea, D.F. Smart, N. Lund, I.L. Rasmussen, B.P. Byrnak, P. Goret, and N. Petrou (1991) *On Cosmic-Ray Cutoff Terminology*, Il Nuovo Cimento, 14**C,** pp. 213-234.

[72] O. Danilova, M. Tyasto, H. Kananen, and P. Tanskanen (1999) The Cosmic Ray Asymptotic Directions for Station Oulu in the Magnetic Field of the Tsyganenko 1989 Model, Geophysica, 35(1-2), pp. 101-109.

[73] M.A. Shea and D.F. Smart (1982) Possible evidence for a ridigity-dependent release of relativistic protons from the solar corona, Space Sci. Rev., 32, pp. 251-271.

[74] J.W. Bieber, P. Evenson, and Z. M. Lin (1992) *Cosmic ray trajectories in the Tsyganenko magnetosphere*, Antarctic Journal, 27, No. 5 (1992 Review), pp. 318-319.

[75] D.F. Smart, M.A. Shea, and R. Gall (1969) *The Daily Variation of Trajectory-Derived High-Latitude Cutoff Rigidities in a Model Magnetosphere*, J. Geophys. Res., 74(19), pp.4731–4738.

[76] J.L. Cramp, M.L. Duldig, and J.E. Humble (1995) *Neutron Monitor Response to Highly Anisotropic Ground Level Enhancements*, Proc. 24th Int. Cosmic Ray Conf.**,** 4, pp. 248-251.

[77] D.F. Smart and M.A. Shea (2000) *Geomagnetic Cutoff Rigidity. Computer Program. Theory, Software Description and Example*. Final Report, Grant NAG5-8009, Center for Space Plasmas and Aeronomic Research, The University of Alabama in Huntsville, Huntsville, Alabama 35889, 198 pp.

[78] K. Nagashima, K. Fujimoto, and I. Morishita (1994) Interplanetary Magnetic Field Colliminated Cosmic Ray Flow Across Magnetic Shock from Inside of Forbush Decrease, Observed as Local-Time-Dependant Precursory Decrease on the Ground, J. Geophys. Res., 99, No. A11, pp. 21,419-21,427.

[79] N.J. Schuch (2006) *Space and atmospheric sciences at South of Brazil*, SCOSTEP -11th Quadrennial Solar Terrestrial Physics Symposium, Sun, Space Physics and Climate, March 6-10, 2006, Rio de Janeiro, Brazil.

[80] F. Jansen and J. Behrens (2008) *Cosmic rays and space situational awareness in Europe*, IEEE Transactions on Magnetics, 21st European Cosmic Ray Symposium, Košice, Slovakia, 9-12 September 2008, http://ecrs2008.saske.sk/dvd/s9.07.pdf, 6 pp.

[81] C.R. Braga, A.D. Lago, W.D. Gonzalez, N.J. Schuch, M.R. Silva, T. Kuwabara, J.W. Bieber, P.A. Evenson, K. Munakata, C. Kato, M. Tokumaru, M.L. Duldig, J. Humble, I.S. Sabbah, H.K.Al Jassar, and M.M. Sharma (2010) *Cosmic ray modulation associated to small and moderate geomagnetic storms during minimum solar activity*, Proceedings of Science, 4th School on Cosmic Rays and Astrophysics, Aug 25 - Sep 4, 2010, São Paulo, Brazil, 14 p.

[82] K. Fujimoto et. al. (2003) *Observation of precursory decrease by the narrow angle muon telescope at MT. Norikura*, Proc.28th Int. Cosmic Ray Conf., July 31- August 7, 2003, Tsukuba, Japan, v6, pp. 3565-3568.

[83] T. Kuwabara, et al. (2006) *Real-time cosmic ray monitoring system for space weather*, Space weather, Vol. 4, S08001, doi:10.1029/2005SW000204, 10 pp.

[84] K. Murakami, K. Nagashima, S. Sagisaka et al. (1979) *Response Functions for Cosmic-Ray Muons at Various Depths Underground*, IL Nuovo Cimento, Vol. 2C, N. 5, pp.635-650.

[85] M. Bercovitch and W.F. Davidson (2012) *Cosmic Ray Neutron Monitoring in Canada*, Physics in Canada, 68(1), pp.16-18.

[86] D. Knudsen, A. Kouznetsov, V. Golovko, J. Armitage, K. Boudjemline, D. Thomson, K. Tapping, D. Boteler, L. Trichtchenko, D. Danskin, and G. Kalugin (2012) *Calgary neutron monitor meeting*, The Canadian Space Weather Forecast Centre, NRCan, 12 October 2012, 2617 Anderson Road, Ottawa, Ontario, Canada.

[87] K. Boudjemline (2012) *Forewarn Detector. Data Analysis*. Oral presentation, FOREWARN Collaboration Meetings, Carleton University, Ottawa, Ontario, Canada, February 15, 2012**.**

[88] K. Boudjemline et al. (2011) *Performance of a drift chamber candidate for a cosmic muon tomography system*, International Conference on Applications of Nuclear Techniques, AIP Conf. Proc. 1412, 129.

[89] K. Boudjemline et al. (2010) *Cosmic ray muon tomography system using drift chambers for the detection of Special Nuclear Materials*, Nuclear Science Symposium Conference Record, IEEE, 547-551.

[90] CRY software: http://nuclear.llnl.gov/simulation/main.html.

[91] D. E. Groom et al. (2001) *Muon stopping power and range tables 10MeV-100TeV*, Atomic Data and Nuclear Data Tables, 78**,** 183–356.

[92] ESTAR program: http://physics.nist.gov/PhysRefData/Star/Text/ESTAR.html.

[93] PSTAR program: http://physics.nist.gov/PhysRefData/Star/Text/PSTAR.html.

[94] GEANT4 software: http://geant4.cern.ch, version 9.3.

[95] L.I. Dorman (1972) *The meteorological effects of cosmic rays*, 'Nauka' Press, Moscow (English translation in Series NASA TTF-755, Washington, DC, 1973).

[96] B. Famoso, P. Rocca, and F. Riggi (2005) *An educational study of the barometric effect of cosmic rays with a Geiger counter*, Physics Education 40(5), pp.461-467.

[97] P.M.S. Blackett (1938) *On the Instability of the Barytron and the Temperature Effect of Cosmic Rays*, Phys. Rev. (Letters to the editor), 54, pp. 973-974.

[98] J. Armitage (2011) *Proposal for Future Canadian Muon Detector*, Oral presentation, Canadian Muon Workshop, St-Émile-de-Suffolk, Québec, Canada, October 17-19, 2011.

Accomplishments

There were several major accomplishments done during the project execution.
Among them there are:

- International muon workshop with 16 participants from 6 countries;
- Several meetings with power grid engineers and several project meetings;
- Extensive review of the literature on all aspects from impacts on power grids to propagations of solar disturbances through the space and effects on cosmic rays. It include the detailed analysis of publications on measurements, theoretical modelling and applications of the cosmic rays, neutrons and muons [3: Kalugin et al., 2013].
- Overview of extreme events during the last solar cycle using the several developed codes, theoretical evaluations of the transport equation for modelling of cosmic ray interactions with solar disturbance.
- Two different designs of the muon detector systems were evaluated with detailed drawings and numerical simulations;
- Test **muon tracking system** detector has been built, and initial data have been recorded and two approaches to remove atmospheric effects on the recorded data were assessed.
- **This resulted in the detailed design recommendations for future detector**

➢ **Workshop Presentations:**

- Kalugin, G., Trichtchenko, L., Armitage, J., Boudjemline, K., and Waller, D. *A study of Forbush decrease events with ground-based muon observations*, Poster presentation, 9th Canadian Solar Workshop, St-Émile-de-Suffolk, Québec, Canada, October 12-15, 2012.
- Trichtchenko, L. and Kalugin, G. *Efficacy of Muon Detection for Solar Flare Early Warning*, Talk on Canadian Muon Workshop, St-Émile-de-Suffolk, Québec, Canada, October 17-19, 2011.
- Armitage, J. *Muon Detectors at Carleton*, Oral presentation, Canadian Muon Workshop, St-Émile-de-Suffolk, Québec, Canada, October 17-19, 2011.
- Armitage, J. *Proposal for Future Canadian Muon Detector*, Oral presentation, Canadian Muon Workshop, St-Émile-de-Suffolk, Québec, Canada, October 17-19, 2011.

➢ **Presentations at the meetings**

- Knudsen D., Kouznetsov, A., Golovko, V., Armitage, J., Boudjemline, K., Thomson, D., Tapping, K., Boteler, D., Trichtchenko, L., Danskin, D., and Kalugin, G. (2012) *Calgary neutron monitor meeting*, The Canadian Space Weather Forecast Centre, NRCan, 12 October 2012, Ottawa, Canada.
- Kalugin, G. *Using ground-based muon measurements for forecasting extreme space weather events*, Oral presentation at Space Weather Group Meeting, Canadian Space Weather Forecast Centre (NRCan), Ottawa, 9 March, 2012.
- Kalugin, G. and Trichtchenko, L. *Combining Muon Detector Measurements with ACE Level 2 Data for Space Weather Forecasting*, Oral presentations, FOREWARN Collaboration Meeting, Carleton University, Ottawa, 15 February and 28 May, 2012.

- Boudjemline, K. *Forewarn Detector. Data Analysis*. Oral presentation, FOREWARN Collaboration Meeting, Carleton University, Ottawa, February 15, 2012**.**
- Trichtchenko, L., Boteler, D., Kalugin, G., Boudjemline, K., Armitage, J., and Waller, D. *Early Warning of the Extreme Space Weather Events. Feasibility Study*, Talk on Energy and Utilities Sector Network Meeting: National Strategy for Critical Infrastructure Protection, Ottawa, November 16, 2011.

➢ **Special Publications**

- Kalugin, G., Trichtchenko, L., Boudjemline, K., Armitage, J., and Waller, D. (2013) *Space weather events with ground-based muon observations (state-of-the-art)*, Geological Survey of Canada, Open File 7285, 158 p., doi: 10.4095/292231.

➢ **Conference presentations**

- Kalugin, G. and Trichtchenko, L. *Frequency parameters of the interplanetary magnetic field during large Forbush decrease events*, Oral presentation at DASP 2013, Kingston, February 18-19, 2013.
- Kalugin, G., Trichtchenko, L., Armitage, J., Boudjemline, K., and Waller, D. *A study of Forbush decrease events with ground-based muon observations*, Poster presentation in 23rd European Cosmic ray Symposium, Moscow State University, Moscow, Russia, 3-7 July, 2012.
- Trichtchenko, L., Boteler, D.H., Kalugin, G., Armitage, J., Boudjemline, K., Waller, D. *Extreme Space Weather Study,* Oral presentation in Public Security S&T Summer Symposium 2012, Ottawa, 11-14 June 2012.
- Boudjemline, K. et al. *Performance of a drift chamber candidate for a cosmic muon tomography system*, International Conference on Applications of Nuclear Techniques, AIP Conf. Proc. 1412, p.129.
- Boudjemline, K. et al. *Cosmic ray muon tomography system using drift chambers for the detection of Special Nuclear Materials*, Nuclear Science Symposium Conference Record, IEEE, pp.547-551.

List of symbols/abbreviations/acronyms/initialisms

NRCan	Natural Resource Canada
DRDC	Defence Research & Development Canada
CME	Coronal Mass Ejection
CI	Critical Infrastructure
CRs	Cosmic Rays
MT	Muon Telescope
ACE	Advanced Composition Explorer
NASA	National Aeronautics and Space Administration
ESW	Extreme Space Weather
GICs	Geomagnetically Induced Currents
GMDN	Global Muon Detector Network
FD	Forbush Decrease
PCTs	Proportional Counter Tubes
IP	InterPlanetary
SSC	Storm Sudden Commencement
ICME	Interplanetary Coronal Mass Ejection
LC	Loss-Cone
IMF	Interplanetary Magnetic Field
EV	Enhanced Variance
DA	Diurnal Anisotropy
TMAs	Trailing Moving Averages
IGRF	International Geomagnetic Reference Field
SOHO	SOlar & Heliospheric Observatory

Glossary

Coronal Mass Ejection

A particularly large release of charged particles from the Sun.

Cosmic Rays

Highly energized charged particles in space with the main constituent being protons (about 90%), mainly originating outside the solar system.

Muon Telescope

A detector of muons, particles produced as a result of interaction of cosmic rays with the oxygen and nitrogen molecules in the Earth's atmosphere.

Advanced Composition Explorer

A NASA solar and space exploration mission to study matter comprising energetic particles from the solar wind, the interplanetary medium, and other sources. The ACE spacecraft is currently operating in a Lissajous orbit close to the L1 Lagrange point (which lies between the Sun and the Earth at a distance of some 1.5 million km from the latter).

Extreme Space Weather

Space weather conditions following large solar flares.

Geomagnetically Induced Currents

Currents induced in conductors, especially pipelines, by the geomagnetic field.

Global Muon Detector Network

International muon detector network composed of four muon telescopes at Nagoya (Japan), Hobart (Australia), Kuwait (Kuwait), and São Martinho (Brazil).

Forbush Decrease

A rapid decrease in cosmic ray intensity associated with solar disturbances.

Proportional Counter Tubes

A counter tube whose output pulse is proportional to number of ions produced.

Storm Sudden Commencement

The moment when a geomagnetic storm starts.

Loss-Cone anisotropy

Effect of intensity deficits confined to a small pitch-angle region around the sunward direction along the interplanetary magnetic field.

Interplanetary Magnetic Field

The solar magnetic field carried by the solar wind among the planets of the solar system.

Pitch angle

The angle between the sunward interplanetary magnetic field direction and the viewing direction of the station or directional channel.

Diurnal Anisotropy

Anisotropy of cosmic rays, which is attributed to the bulk streaming of the cosmic ray gas caused by the corotating interplanetary magnetic field.

International Geomagnetic Reference Field

A standard mathematical description of the Earth's main magnetic field.

Solar & Heliospheric Observatory

A space-based observatory, viewing and investigating the Sun from its deep core, through its outer atmosphere - the corona - and the domain of the solar wind, out to a distance ten times beyond the Earth's orbit.